DOE/ER/53241--T1

DOE/ER/53241--T1

DE91 012396

Particle Confinement and Fueling Effects on the Maryland Spheromak

by

Alexander Bruce Filuk

Dissertation submitted to the Faculty of the Graduate School
of the University of Maryland in partial fulfillment
of the requirements for the degree of
Doctor of Philosophy
1991

FG05-86ER53241

Advisory Committee:

Professor George Goldenbaum, Chairman/Advisor
Professor Alan DeSilva
Professor Hans Griem
Professor Moon-Jhong Rhee
Associate Professor Richard Ellis

Abstract

Title of Dissertation: Particle Confinement and Fueling Effects
on the Maryland Spheromak

Alexander Bruce Filuk, Doctor of Philosophy, 1991

Dissertation directed by: Dr. George Goldenbaum, Professor of Physics,
Department of Physics and Astronomy

The spheromak plasma confinement concept provides the opportunity to study the evolution of a nearly force-free magnetic field configuration. The plasma currents and magnetic fields are produced self-consistently, making this type of device attractive as a possible fusion reactor. At present, spheromaks are observed to have poorer particle and magnetic confinement than expected from simple theory. The purpose of this study is to examine the role of plasma density in the decay of spheromaks produced in the Maryland Spheromak experiment. Density measurements are made with an interferometer and Langmuir probe, and results are correlated with those of other plasma diagnostics to understand the sources of plasma, the spheromak formation effects on the density, and the magnitude of particle loss during the spheromak decay. A power and particle balance computer model is constructed and applied to the spheromaks studied in order to assess the impact of high density and particle loss rate on the spheromak decay. The observations and model indicate that the decay of the spheromaks is at present dominated by impurity radiation loss. The model also predicts that high density and short particle confinement time play a critical role in the spheromak power balance when the impurity levels are reduced.

Dedication

To my parents,
in gratitude for their years of love.

Acknowledgements

There are many people who have helped make this work possible: it is a pleasure to acknowledge them here.

I owe a debt of gratitude to the staff and faculty of the Laboratory for Plasma Research who have helped me in so many ways over the years. In particular, I would like to thank my advisor, Professor George Goldenbaum, for his example of a keen physics curiosity and high scientific standards. Professors DeSilva, Ellis, and Griem provided valuable guidance and advice. My thanks to Mr. Don Martin and Mr. Dave Miller for helpful technical assistance. It was a pleasure to deal with Mr. Ken Diller; his knowledge, professionalism, and friendliness are outstanding.

The MS group has provided encouragement, shared ideas and equipment, and generally made group research thoroughly enjoyable. Thanks to Dr. Cecil Chin-Fatt for his optimism and day-to-day operations advice, and to Dr. Roger Hess for maintaining excellent computer systems. I am grateful to fellow graduate students Bruce Barrow, Claude Côté, Jean-Luc Gauvreau, and Fu-Kwun Hwang for friendship, helpful discussions, and shared data.

There are some who have touched my life forever. To my father, mother, and brothers, I will always be grateful. To my wonderful wife Jean, who supported me throughout the final stages of this research and typed the bulk of this work, I offer my deepest love and gratitude. Finally, thanks be to my God for His wisdom and the wonder of creation (Rom. 1:20).

Contents

List of Tables

List of Figures

Chapter 1

Introduction

1.1 Motivation

The spheromak plasma magnetic confinement scheme is the subject of research at several laboratories around the world [1]. The spheromak concept is interesting from a fundamental plasma physics perspective because it represents a nearly 'force-free' magnetic configuration where the plasma current **j** and plasma magnetic field **B** sustain one another (with an externally imposed equilibrium field for basic constraint of the plasma expansion [2]) such that **j** is parallel to **B**. The 'classical spheromak' is the axisymmetric solution to the force-free equation

$$\nabla \times \mathbf{B} = \lambda \mathbf{B}$$

where λ is a constant, with a spherical or cylindrical flux surface boundary condition. The field shows the linked toroidal and poloidal structure familar to tokamaks, except that the poloidal field is comparable to the toroidal field in strength. Both toroidal and poloidal fields are supplied by internal plasma currents. The existence of such fields in astrophysical phenomena was first suggested by Woltjer [3] and Chandrasekhar [4]. The spheromak concept is also interesting to study for possible application as a fusion plasma confinement device [1]. In this case, much work is needed to extend spheromak lifetimes and plasma temperatures to the parameter regime of fusion devices.

Experimentally, the past decade has seen significant advances in spheromak understanding. The early experiments demonstrated and verified the spheromak magnetic field structure [5,6,7] and the idea, applied most successfully by Taylor [8], that a force-free state is a minimum energy state that the plasma will relax into regardless of the details of its formation scheme. Subsequent work concentrated on stabilizing the spheromak against its most common MHD tilt and shift modes [9]. More recently, emphasis has been placed on understanding the fast decay rate of spheromak magnetic energy [10]. Present spheromaks are formed and then usually allowed to freely decay (although some sustainment has been done [11]), with the decaying magnetic energy being used in heating the plasma and supplying power indirectly to sustain the plasma against particle and radiative energy losses. Low Z impurities, most commonly carbon and oxygen, have limited most spheromaks to low electron temperatures (10–30 eV) determined by dominating radiative power loss. These low temperature spheromaks have high resistivity so that their plasma currents decay rapidly. For spheromaks that are reported to have 'burned through' the low Z radiation barriers [12,13], the magnetic field and current still decay 2–3 times faster than expected from simple Ohmic heating of the electrons (see Chapter 4). The power losses are not yet understood, but density has been shown to play a significant role when the radiation barrier is surpassed [14]. In particular, a high density spheromak with a short particle confinement time requires a significant influx of particles to maintain the density. These particles come from the gas surrounding the plasma as well as from gas desorbed from surfaces near the plasma. Thus it is important to understand where the plasma constituents come from and for how long the plasma particles are confined.

The Maryland Spheromak Experiment (MS) was originally designed for high field, hot, relatively long-lived spheromaks ($B \approx 10$ kG, $t \approx 100$ eV, $\tau \approx 2$ ms). To date the plasmas produced have been much colder and thus short-lived ($B \approx 4 - 7$ kG, $T \approx 10 - 15$ eV, $\tau \approx 0.2$ ms). These plasmas have also had considerably higher density ($n \approx 7 \times 10^{14}$ cm^{-3}) than the hottest reported spheromaks ($n \approx 5 \times 10^{13}$ cm^{-3}). The purpose of this study is to understand the sources of the density in MS spheromaks, the

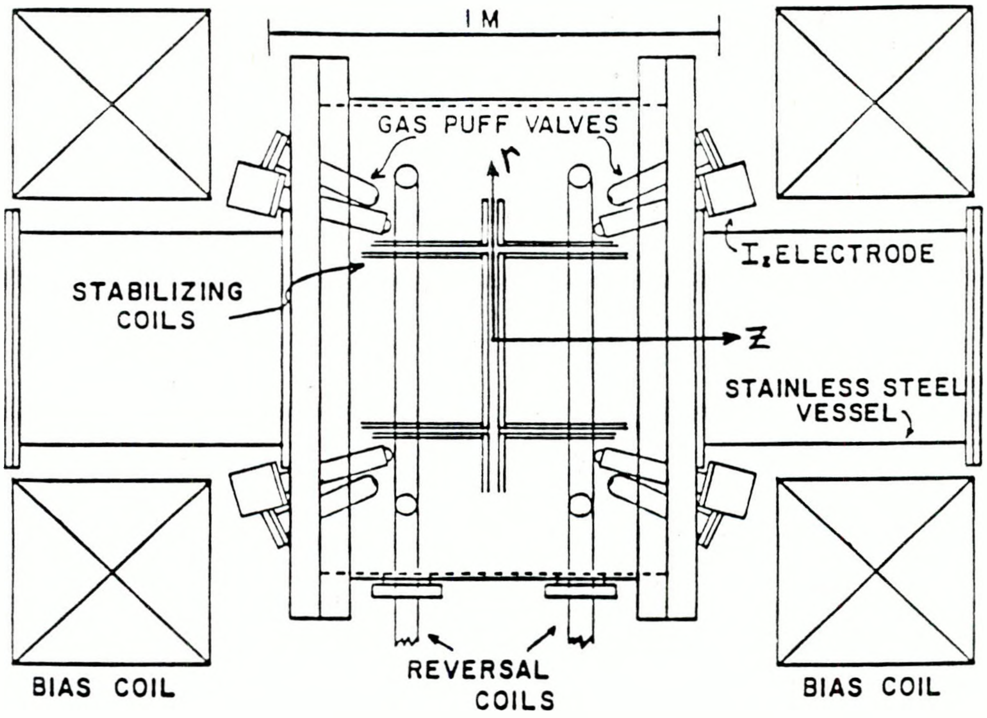

Figure 1.1: Section view of the MS vessel with parts of the figure-8 stabilizing coils indicated. The microwave preionizer is not shown.

mechanisms underlying the density evolution, and the impact of plasma density, particle influx, and impurities on spheromak temperature in general. Interferometer and Langmuir probe diagnostics were used to measure the density, and a computer model was fit to MS data to determine properties of existing spheromaks and to project the conditions necessary for higher temperatures.

1.2 The Maryland Spheromak Experiment

1.2.1 Formation Scheme

The MS spheromaks are formed using the combined $z - \theta$ discharge scheme [15]. Figure 1.1 shows a cross-section of the device. The cylindrical coordinate system used in the spheromak description has a z axis corresponding to the axis of the MS vessel, with $z = 0$ located at the midplane of the device. The three main formation components indicated in Figure 1.1 are the bias coils, the reversal coils, and the I_z electrodes. Other elements include the puff valves, passive stabilizing conductors, and microwave preionizer.

The first component, the bias coils, are a pair of 600 turn aluminum coils connected in series and liquid nitrogen cooled for low resistance. These coils produce a flat-top pulse of about 2 sec duration with typically 300-600 A to provide a mirror-shaped magnetic field that penetrates the stainless steel vacuum vessel walls. For the timescale of the experiment the bias field flux in the wall is constant. About 2 ms before the plasma is initiated, the puff valves are fired to inject gas clouds toward the center of the vessel. The working gas is typically deuterium, although helium is also used. Static gas fills have been substituted for the puff with little difference observed in the resulting plasmas. The amount of gas puffed in corresponds to equilibrium pressures of 3-12 mT in the 900 L chamber volume (when the vacuum pumps are isolated from the system).

The second component, the pair of single turn reversal coils, is energized about 90 μs before the I_z, and reaches a maximum current of typically 350 kA at about the I_z firing time. Both the reversal and I_z current waveforms are essentially 160 μs half-period sine waveforms, with small late time decaying tails. These two circuits are driven by ignitron-switched capacitor banks and are crowbarred to prevent the currents from ringing over. The vacuum poloidal flux at I_z firing time is shown in Figure 2.8 (p. 30) for a typical case. This flux is produced by the reversal and bias currents. The reversal coil is observed to create localized breakdown under conditions of high reversal current or large gas load, and this pre-I_z breakdown assists in keeping the main I_z breakdown on time. The microwave preionizer is most often triggered at reversal trigger time rather than I_z time, because the electron-cyclotron resonance appeared to work much better at inducing local reversal breakdown (which then assisted proper I_z breakdown) than directly inducing the I_z breakdown.

The final formation component is the set of I_z electrodes. A peak current of about 0.75 MA is discharged axially between two annular rings of 16 electrodes. The I_z current ionizes the fill gas to produce the plasma, creates the toroidal magnetic field B_θ necessary for a spheromak, and provides the initial heating currents. A typical volume average current density at peak I_z current is 2-3 MA/m^2. The net poloidal current flowing across a disk of radius r lying in the $z = 0$ midplane and centered on the axis $r = 0$ is defined as I_p. Figure 1.5 shows $I_p = 2\pi r B_\theta$ at peak I_z and at selected subsequent times.

The inductive part of the formation begins as the I_z rises. At this time the reversal current begins falling. Since highly conducting plasma has been created near the reversal coils, the decreasing reversal current induces a toroidal plasma current just inside the reversal coils. As shown in the formation simulations of Guzdar et al. [15], as the (crowbarred) reversal current drops to zero the induced toroidal plasma current's poloidal magnetic field closes inside the reversal coils, and the configuration relaxes into the closed flux surface configuration shown in Figure 1.4 at time t=8.25 ms. Various configurations of interior passive stabilizing conductors help to stabilize the spheromak tilt mode during the decay phase.

1.2.2 Diagnostics

The MS experiment has diagnostics to measure magnetic field, density, and visible/UV spectral light emission. Rogowski coils are used to monitor the I_z current and reversal coil currents. A Thomson scattering electron temperature/density apparatus and a bolometer were not operational when the density measurements reported here were performed, so no definitive electron temperature or radiated power measurements were available.

As described in the next section, data were collected with a wide variety of interior stabilizing conductors. The most well-diagnosed spheromaks showing the best overall properties were obtained for the conditions of MS shots #4503-4670. This case will subsequently be referred to as condition 4503, and results from various diagnostics for this condition are presented here as typifying the stable decaying MS spheromak. The formation currents for this condition were: peak reversal =315 kA/coil, peak I_z = 720 kA, bias = 500 A.

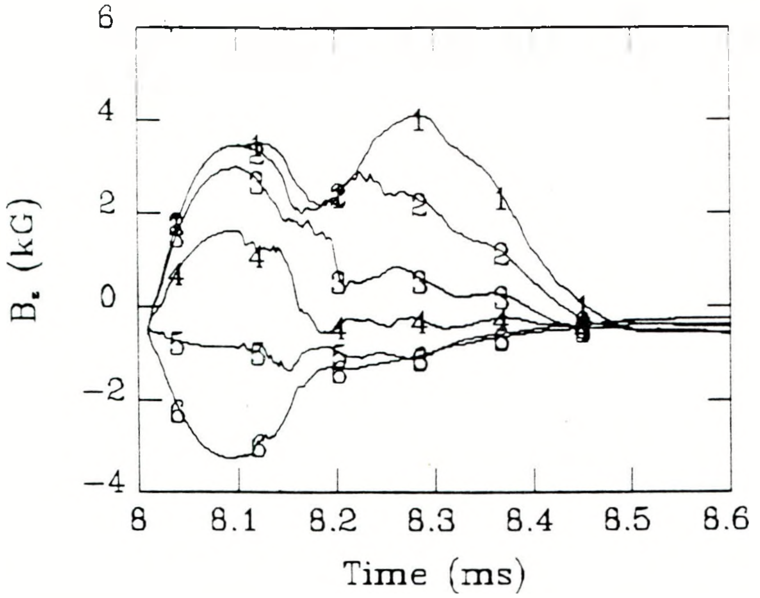

Figure 1.2: B_z histories from the midplane probe for condition 4503. Locations # 1-6 are at r=(5.0,12.7,20.3,27.9,35.6,43.1)cm.

1.2.2.1 Magnetics

Magnetic data are collected by three probes [16]. The midplane probe is located at z=0 and measured the three **B** components at 6 radial locations separated by 7.6 cm spacing. Figures 1.2, 1.3 show time histories of B_z and B_θ for condition 4503. Note that t=0 was picked as an arbitrary time well before the puff valves were triggered. For condition 4503, the reversal was triggered at t=8.01 ms, while the I_z was triggered at t=8.1 ms. The spheromak magnetic field was fully established by t=8.25 ms and decayed with small relaxation ripples as discussed in Chaper 3.

The L-shaped magnetic probe is located at the midplane in a similar fashion as the midplane probe, but this probe has a 90 bend and seven sets of orthogonal B coils. Adjusting the probe location to perform multiple shot averaged scans gave the magnetic field in one plane between the I_z electrodes. These data were used to produce the flux and net poloidal current plots of condition 4503 that are shown in Figures 1.4 and 1.5. For this condition, the I_z circuit was triggered at t = 8.1 ms. The dotted lines indicate regions of negative flux and net poloidal current in Figures 1.4 and 1.5, respectively. The jagged

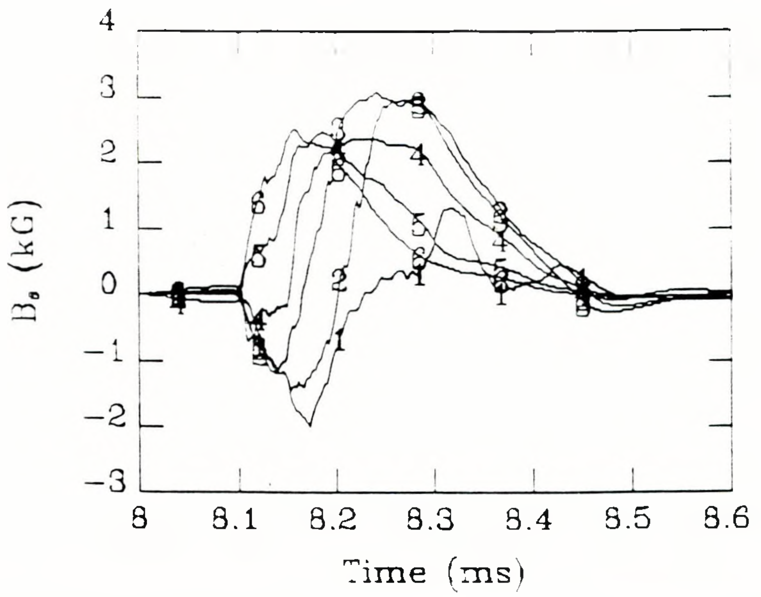

Figure 1.3: B_θ histories from the midplane probe for condition 4503. Locations are as in Figure 1.2.

contours seen at large radii are the result of uncertainties in the measurement technique. These results will be discussed in the context of the density measurements in Chapter 3.

The final magnetic probe is a radial probe indicated in Figure 2.8. This probe is used to measure B_θ near the I_z electrodes and thus, with the assumption of axisymmetry, to indicate the net poloidal current at various radii. This probe was not used extensively.

1.2.2.2 Spectroscopy

The spectroscopy diagnostic on MS at the time of this work was a 3/4 m spectrometer coupled to an optical multichannel analyzer (OMA). The OMA/spectrometer gave a gated 'snapshot' of a portion of the plasma emission spectrum with one dimension of spatial resolution. Optionally, a high speed chopper was used to trade the space dimension information for rough ($\approx 50 \mu s$) time resolution of a single viewing chord [17]. The observed impurity spectral linewidths were translated into impurity ion temperatures T_D [10,18] based upon the well-known Doppler line broadening mechanism [19]. Figure 1.6 shows ion temperature and intensity histories for the C III (2297 Å), C IV (5801 Å), and O IV (3063 Å) impurity lines for condition 4503. The line of sight for this data was parallel to

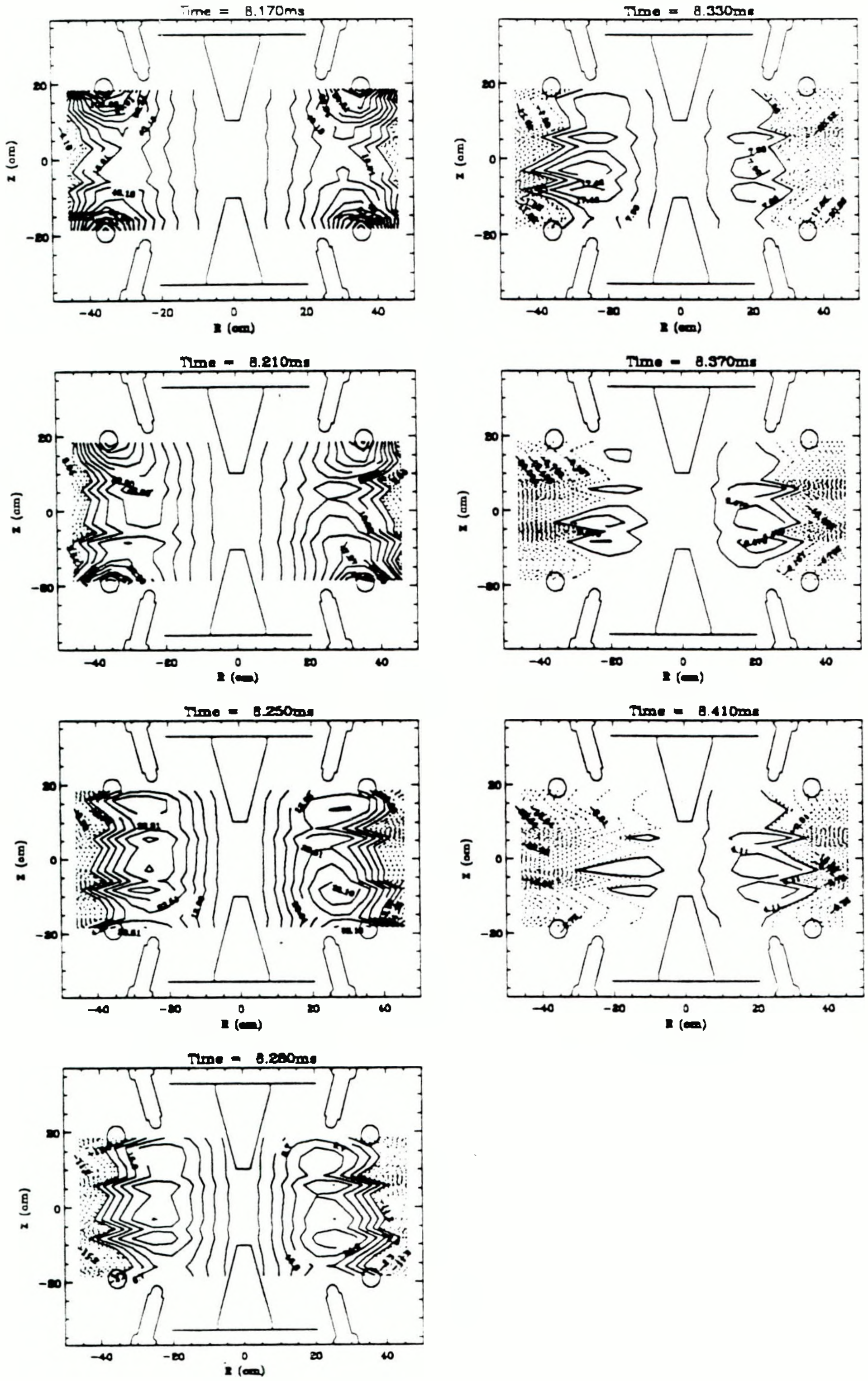

Time = 8.170ms

Time = 8.330ms

Time = 8.210ms

Time = 8.370ms

Time = 8.250ms

Time = 8.410ms

Time = 8.280ms

Figure 1.4: Poloidal flux contours from the L-probe for condition 4503 at selected times (refer to text). Values in mWb.

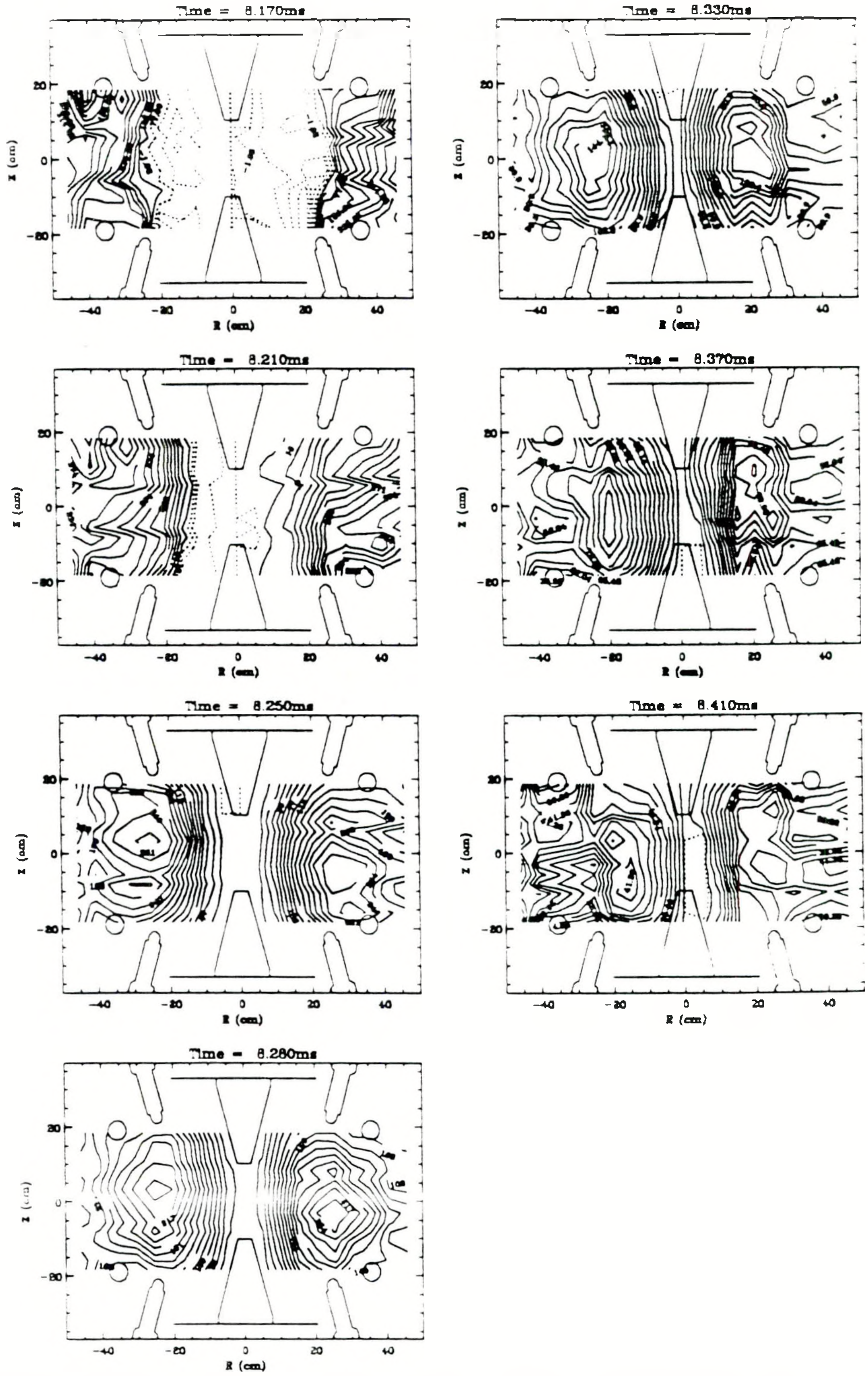

Figure 1.5: Poloidal current contours from the L-probe for condition 4503 at selected times (refer to text). Values in kA.

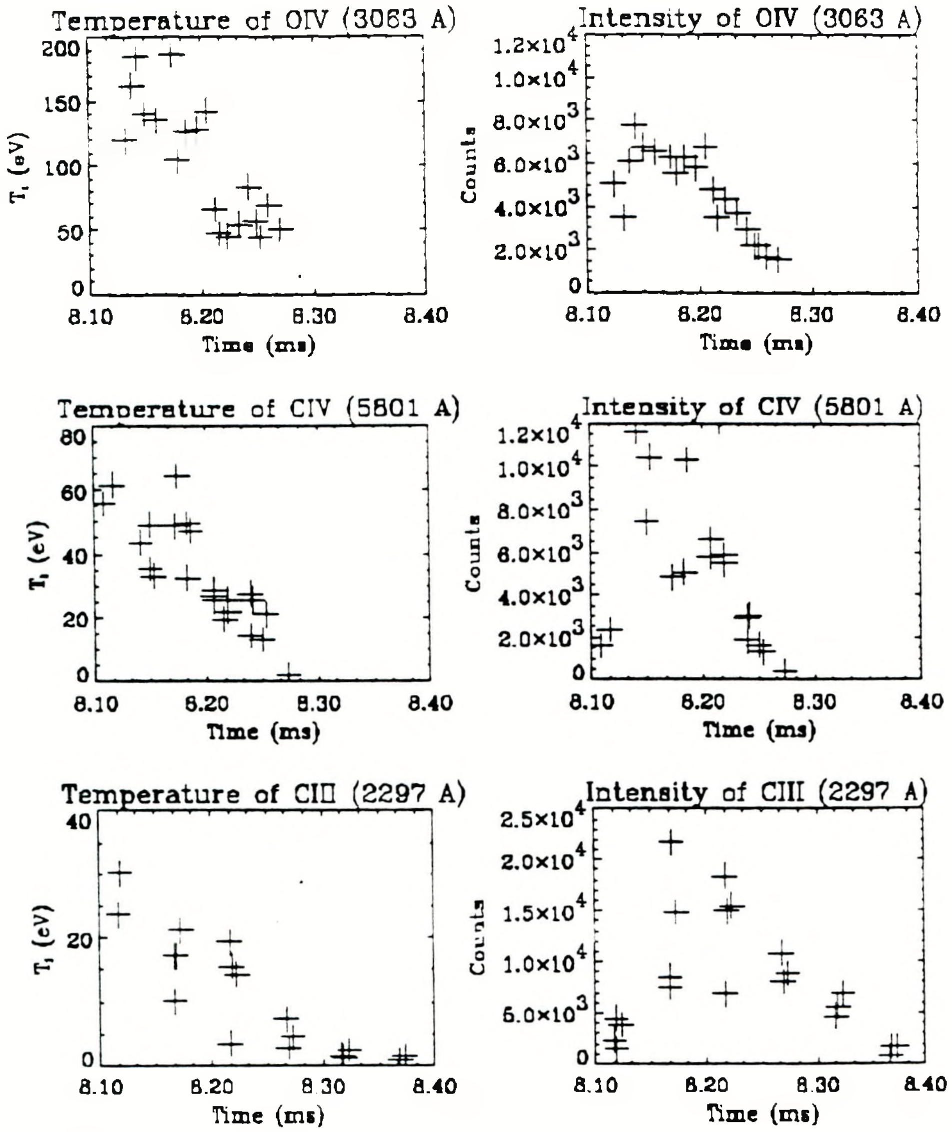

Figure 1.6: Impurity ion temperatures derived from Doppler-broadening, and corresponding line intensities for O IV, C IV and C III lines.

the vessel z axis, at radius r=16.5 cm.

In addition to providing information about the ion temperatures, the presence or absence of various impurity emission lines gives an indication of the electron temperature, when an equilibrium distribution model can be adopted [19]. As discussed in Chapter 4, the non-equilibrium coronal model is valid in the MS parameter regime. In this treatment, the impurity charge state distributions are determined by relative rates of electron impact ionization and radiative recombination. The next lower order approximation would be to ignore particle transport (refueling influx and finite loss time) and assume a coronal equilibrium (CE) distribution. In this case equilibrium of the above rates is attained, and the CE distribution of ion charge state as a function of temperature becomes applicable. On MS, oxygen was the most plentiful low Z impurity available from the materials inside the MS vessel, and large amounts of oxygen emission were always observed spectroscopically.

The oxygen CE distribution of charge states has been calculated by Carolan and Piotrowicz [20], and shows clearly the concentration of highly radiative O III – O V charge states in the temperature range $10 \leq T_e \leq 25$ eV. These charge states form a radiation barrier that must be surpassed to attain the much less radiative helium-like O VII state. The oxygen CE distribution also indicates that the presence of O III and O IV with the absence of O II and O V implies an electron temperature $T_e \approx 11 - 13$ eV. On clean MS shots, O III and O IV were almost always observed: O V was clearly seen only under the optimum case of condition 4503. This implied a central temperature $T_e^{core} \approx 13 - 16$ eV for a CE electron distribution, since the line of sight in this case was through the anticipated hottest parts of the plasma (the magnetic axis region and the vicinity of the I_z electrodes). The particle transport effects would make this a lower bound on T_e^{core}, since influxing ions in the process of being stripped of their electrons would slightly shift the distribution to lower charge states for a give temperature, or equivalently raise the temperature for a given distribution. Because the inferred MS temperatures were well below that of the oxygen radiation barrier at 25 eV [20], particle transport effects would not alter the average impurity charge state by more than 10% [20], making the CE lower bound for T_e^{core} a reasonable estimate. The volume average electron temperature was taken as $T_e = T_o + 0.5T_e^{core}$ [14], where $T_o \approx 4$ eV is the edge temperature, giving an estimate for maximum volume average electron temperature of $T_e \approx 11$ eV. It should be noted that this temperature estimate technique cannot be used with the carbon ion distribution, because the C V species that should be present at $T_e > 9$ eV cannot be readily observed due to the large (299 eV) excitation energy required to populate the C V excited states. The inferred electron temperature is consistent with that obtained from the decay rate of the volume averaged spheromak magnetic field, with an anomaly factor of 2–3 times Spitzer resistivity [14] (see Chapter 4).

The impurity ion Doppler temperatures indicated in Figure 1.6 are much higher than the inferred electron temperature. The significance of this, the implications for the majority species ion temperature, and the effect on the spheromak power balance are all discussed in Chapter 5.

1.2.2.3 Density

The density diagnostics on MS are a 4-beam quadrature laser interferometer, providing line-integrated electron density, and a floating double tip edge Langmuir probe to provide local ion density. Details of these diagnostics will be presented in the next chapter.

1.2.3 Overview of MS Development

Most of the inital phase of MS operation was devoted to diagnosing and eliminating a gross asymmetry in the plasma. Magnetic measurements showed a spheromak-like field structure that was displaced radially from the vessel axis in a direction away from the reversal coil feed-throughs. Numerous configurations of conductors were used in the vessel to try to keep the plasma from shifting off-center. These included various types of figure-8 stabilizing coils [21], a cylindrical core down the vessel axis, a cylindrical liner, and cone or funnel shaped conductors on the axis [22] (indicated in Figure 1.4). All of these conductors slightly reduced the magnitude of the asymmetry, but further measurements indicated that the problem was current from the plasma to the bare metal reversal coils. This coupling was originally expected to be very weak because of the difficulty of plasma current crossing strong magnetic fields—the 'magnetic insulation' phenomenon.

The second phase of MS operation was finding a suitable insulating covering for the reversal coils. A 'proof of principle' insulating tape reversal coil wrapping greatly reduced the plasma asymmetry but yielded dense plasmas. Following this, a series of wrapping materials were tried. The general idea was to use a relatively inexpensive, replaceable, two-component covering; one component was to provide good electrical insulation and the other was to shield the insulating material in order to prevent sputtering, evaporation, or gas desorption in the presence of plasma. Combinations of wrappings used were rubberized electric ("Bishop") tape under fiberglass, teflon tape under titanium foil, and teflon tape under nichrome foil. The Bishop tape/fiberglass combination yielded relatively dense plasmas, while the titanium foil became shredded and torn due to magnetic forces and hydrogen embrittlement [23].

Condition 4503 was obtained using the teflon/titanium combination. Some fluorine (from the teflon) has been observed in the plasma spectra, but the measured high densities depended more strongly on the machine parameters and other materials inside the chamber than on the reversal coil wrapping, once the outer metallic foil covering was installed (see Chapter 3).

The most recent phase of MS work has been concentrated on burning through the impurity radiation barrier. The results presented here indicate that the combination of high density, short particle confinement time, and large impurity content has imposed a strict temperature limit on MS spheromaks, producing the relatively short configuration lifetimes.

Chapter 2

Density Diagnostics

The following sections discuss both the theory and operation of the interferometer and the Langmuir probe. The techniques used to obtain radial density profiles are presented. CGS units are used except where noted otherwise. Temperature is always in eV.

2.1 Theory

2.1.1 Interferometer

The interferometer diagnostic is used to measure line-integrated electron densities along chords at the midplane of MS. The principles of operation are well known and have been discussed by numerous authors [24,25]; they are summarized here. Interferometry involves measuring the phase shift of light passing through the plasma. Let f be the light frequency, f_{p_e} the electron plasma frequency, f_{c_e} the electron cyclotron frequency ($f_{c_e} = \frac{1}{2\pi}\frac{eB}{m_e c}$), and f^c the momentum exchange collision frequency of electron with ions or atoms. Then in the collision dominated plasma approximation, where

$$\frac{f_{p_e}}{f}, \frac{f_{c_e}}{f}, \frac{f^c}{f} \ll 1, \tag{2.1}$$

one has a simple expression for the plasma index of refraction μ.

$$\mu = [1 - (\frac{f_{p_e}}{f})^2]^{1/2} \doteq 1 - \frac{f_{p_e}^2}{2f^2} \tag{2.2}$$

An interferometer divides a monochromatic plane wave of light into two beams: the scene beam passes through the plasma and is phase-shifted with respect to the reference beam.

which travels only through air. The difference in phase $\Delta\phi$ between the recombined beams is the vacuum wavenumber $k = \frac{2\pi}{\lambda}$ times the optical path length difference.

$$\Delta\phi = \frac{2\pi}{\lambda}\int |\mu_{scene} - \mu_{ref}|\, d\ell = \frac{2\pi}{\lambda}\int |\mu - 1|\, d\ell \quad .$$

where the line integral is along the path through the plasma. Using (2.2) for μ gives

$$\Delta\phi = \frac{\pi}{fc}\int f_{pe}^2\, d\ell = \frac{e^2\lambda}{m_e c^2}\int n_e\, d\ell \quad . \tag{2.3}$$

For the parameter regime of MS, one may check that the approximations of (2.1) hold. For the visible laser light ($\lambda = 6328\mathring{A}$) used, $f = \frac{c}{\lambda} = 4.74 \times 10^{14}$ s^{-1}, while one has

$$\begin{aligned} \frac{f_{pe}}{f} &= \frac{4\pi n_e e^2}{m_e f} = 2.35 \times 10^{-19} n_e^{1/2} \quad . \\ \frac{f_{ce}}{f} &= \frac{eB}{m_e c f} = 3.71 \times 10^{-8} B \quad . \\ \frac{f^c}{f} &\doteq \frac{f_{ei}}{f} = 6.12 \times 10^{-21}\frac{n_e \ln\Lambda}{T_e^{1/2}} \quad . \end{aligned}$$

For a plasma density $n_e \le 1 \times 10^{15}$ cm^{-3}, magnetic field strength $B \le 7$ kG, and temperature $T_e \le 100$ eV, these three quantities are all much less than 1.

Relation (2.3) may be expressed (with λ given above) as

$$\frac{\Delta\phi}{2\pi} = 2.84 \times 10^{-18}\overline{n}_e L \tag{2.4}$$

where $\overline{n}_e \equiv \frac{1}{L}\int n_e\, d\ell$ is the line-average density in cm^{-3}, and L is the total plasma path length in cm. Note that the numerical coefficient is proportional to the wavelength used, so that low density or small plasmas require a longer wavelength laser to achieve a measurable phase shift. The phase shift $\Delta\phi$ is observed as an interference between the scene and reference beams. What is observed is typically the intensity of the interference fringes, which are proportional to $\sin\Delta\phi$ or $\cos\Delta\phi$. One may extract $\Delta\phi$ from the measured intensity using the appropriate inverse trigonometric function, but ambiguities exist in the choice of branch of $\sin^{-1}$ or $\cos^{-1}$; as well, there are sensitivity nulls where sin or cosine reach extrema. As Buchenauer and Jacobson have demonstrated [26], a quadrature polarizing interferometer solves these problems.

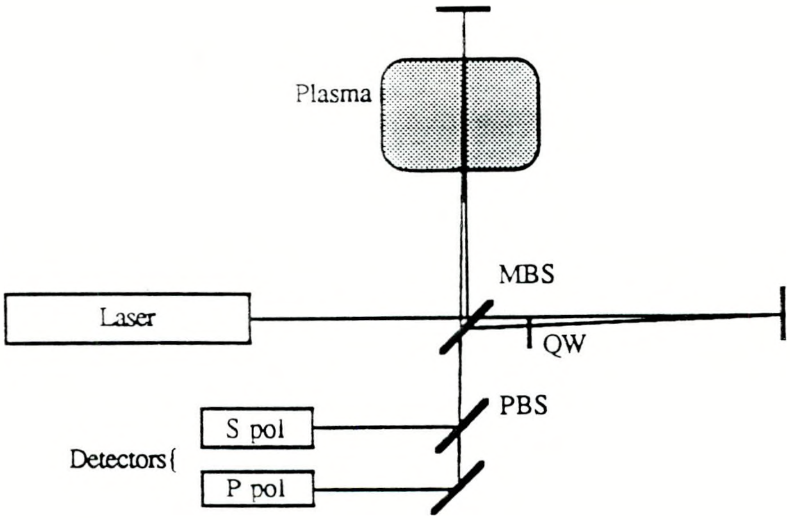

Figure 2.1: Quadrature interferometer arrangement showing main beamsplitter (MBS), $\lambda/4$-waveplate (QW), and polarizing beamsplitter (PBS).

The quadrature arrangement uses polarized light in the interferometer to yield simultaneously both $\sin\Delta\phi$ and $\cos\Delta\phi$, allowing unambiguous branch selection of the inverse trigonometric function. Figure 2.1 shows the optics used. A linearly polarized laser light source is split into scene and reference beams. The scene beam passes through the plasma and is phase shifted, while the reference beam is circularly polarized by one pass through a $\frac{\lambda}{4}$-waveplate. The recombined beam is divided into its orthogonal polarization components, which are separately monitored by detectors. One may write the initial light electric field vector in terms of its horizontally polarized (within the plane of the optics of Figure 2.1, or P polarized) and vertically polarized (perpendicular to the optics plane, or S polarized) components,

$$\mathbf{E}_o = E_o \begin{pmatrix} -\sin\theta_o \\ \cos\theta_o \end{pmatrix} e^{i(\mathbf{k}\cdot\mathbf{r}-\omega t)}$$

for a linear polarization at angle θ_o with respect to the vertical. The upper element is the horizontal component and the lower element is the vertical component.

Now consider the effects of the various non-ideal polarizing optical components, written as matrix operators. The free-space (air) propagation and normal incidence mirror reflections are assumed to have no effect on the polarization other than overall negligible phase inversions. Denote the reflecting and transmitting operations of the main beamsplitter as $\mathcal{R}, \mathcal{T}$ respectively. A non-ideal beamsplitter will slightly change the polarization of incident light due to polarization-dependent reflectivities (R_h, R_v) and transmissivities (T_h, T_v). Thus one has

$$\mathcal{R} = R\begin{pmatrix} R_h & 0 \\ 0 & R_v \end{pmatrix} \quad , \quad \mathcal{T} = T\begin{pmatrix} T_h & 0 \\ 0 & T_v \end{pmatrix} \quad .$$

The plasma effect on the light is approximately a simple phase shift $\Delta\phi$. The total transmission of the non-polarizing vessel windows may be denoted by T_w. Thus the plasma operation is $\mathcal{P} = T_w e^{i\Delta\phi}$. The $\frac{\lambda}{4}$-waveplate operation may be written, for a waveplate whose optical axis is at an angle θ with respect to the vertical, as

$$\mathcal{Q} = \begin{pmatrix} s^2 \pm ic^2 & sc(-1 \pm i) \\ sc(-1 \pm i) & c^2 \pm is^2 \end{pmatrix} \quad .$$

where $c \equiv \cos\theta$, $s \equiv \sin\theta$, and the upper (lower) sign is used if the optical axis is the fast (slow) axis of the waveplate.

The scene beam is reflected at the main beamsplitter, passes through the plasma, and returns through the main beamsplitter. The reference beam passes through the main beamsplitter and returns through the $\frac{\lambda}{4}$-waveplate to be reflected at the main beamsplitter. Combining all the polarization effects gives a scene beam operator $\mathcal{M}^{Scene} = \mathcal{T}\mathcal{P}\mathcal{R}$ and reference beam operator $\mathcal{M}^{Ref} = \mathcal{R}\mathcal{Q}\mathcal{T}$. Explicitly,

$$\begin{aligned} \mathcal{M}^{Scene} &= T_w e^{i\Delta\phi}\begin{pmatrix} T_h R_h & 0 \\ 0 & T_v R_v \end{pmatrix} \\ \mathcal{M}^{Ref} &= \begin{pmatrix} R_h T_h (s^2 \pm ic^2) & R_h T_v sc(-1 \pm i) \\ R_v T_h sc(-1 \pm i) & R_v T_v (c^2 \pm is^2) \end{pmatrix} \quad . \end{aligned}$$

The beams are recombined and projected into polarization components. The horizontal component is given by

$$\mathbf{E}_h = \begin{pmatrix} 1 & 0 \\ 0 & 0 \end{pmatrix} (\mathcal{M}^{Scene} + \mathcal{M}^{Ref}) \mathbf{E}_o$$

while the vertical component is given by

$$\mathbf{E}_v = \begin{pmatrix} 0 & 0 \\ 0 & 1 \end{pmatrix} (\mathcal{M}^{Scene} + \mathcal{M}^{Ref})\mathbf{E}_o$$

For an ideal quadrature arrangement one lets $\theta = 0$ and $\theta_o = \frac{\pi}{4}$. Here, let $\theta = 0 + \delta$ and $\theta_o = \frac{\pi}{4} + \delta_o$ to see the effect of small polarization and $\frac{\lambda}{4}$-waveplate misalignments $(\delta, \delta_o \ll 1)$. Keeping only terms linear in α, δ, and δ_o, the two polarized components' intensities are proportional to the average magnitude of the electric fields.

$$I_h \propto |\mathbf{E}_h|^2 = R_h^2 T_h^2 \left\{ (1 + 2\delta_o)(\frac{1 + T_w^2}{2} \pm T_w \sin\Delta\phi) + \delta \frac{T_v}{T_h} \left[T_w(\cos\Delta\phi \mp \sin\Delta\phi) - 1\right] \right\} E_o^2$$

$$I_v \propto |\mathbf{E}_v|^2 = R_v^2 T_v^2 \left\{ (1 - 2\delta_o)(\frac{1 + T_w^2}{2} + T_w \cos\Delta\phi) + \delta \frac{T_h}{T_v} (T_w(\cos\Delta\phi \mp \sin\Delta\phi) + 1) \right\} E_o^2$$

One now requires that the $\frac{\lambda}{4}$ waveplate misalignment δ be negligible in order to drop the second term on both of the above expression. Then both intensities consist of a fixed part and a sinusoidal part that varies with the relative phase shift $\Delta\phi$. By calibrating the interferometer one has

$$I_h = I_{h_o} + \tilde{I}_h \sin\Delta\phi$$

$$I_v = I_{v_o} + \tilde{I}_v \cos\Delta\phi$$

where I_{h_o}, $\tilde{I}_h$, I_{v_o}, and $\tilde{I}_v$ are known. Thus the line average density can be found using

$$\overline{n}_e = \frac{c_1}{L} \tan^{-1} \left[\frac{I_h - I_{h_o}}{I_v - I_{v_o}} \left(\frac{\tilde{I}_v}{\tilde{I}_h} \right) \right] \tag{2.5}$$

where c_1 is a constant determined by Equation (2.4), and the appropriate branch of $\tan^{-1}$ is determined uniquely by the behavior of the sin and cos signals. Note that variations in the laser output, attenuation of polarizing optics and vacuum vessel windows, and small misalignments of the incident polarization are all accounted for or normalized out of the calculated line density. Only the alignment of the $\frac{\lambda}{4}$-waveplate appears as a first-order effect, so that care must be taken in aligning this optical component. In practice this is no significant restriction because the waveplates have their optical axes factory marked, permitting alignment to within ±2°.

2.1.2 Langmuir probe

The Langmuir probe density diagnostic has advantages over the inteferometer in that it gives a local density, and may also provide a local temperature. The disadvantages are that the probe perturbs the plasma, and many simplifying assumptions (some of which are only marginally satisfied under these conditions) are made to interpret the probe signal. A summary of the probe principle of operation and assumptions required are presented here, based on Chen's [29] thorough discussion of electric probes.

A floating double tip probe is used because the large I_z discharge current in MS creates large fluctuations of the plasma floating potential during spheromak formation. The circuit is essentially two metal tips, in contact with the plasma, with a bias voltage V_B between them (see Figure 2.7). If the two tips have the same area A, the current I through the circuit is given by [29]

$$I = I_o \tanh\left(\frac{V_B}{2T_e}\right) \tag{2.6}$$

where T_e is in eV. The ion saturation current I_o is given approximately by [30]

$$I_o = j_o A = \frac{n_i A}{2}\sqrt{\frac{T_e}{m_i}} \tag{2.7}$$

where n_i is the ion density and m_i the ion mass.

Use of Equations (2.6) and (2.7) requires that simple thin-sheath Langmuir probe theory [31] be valid. This requires: i) essentially Maxwellian velocity distributions (i.e. negligible flow energy compared to thermal energy), ii) probe sheath thickness δ much less than probe dimension a, iii) ion gyroradius ρ_i much larger than a, iv) ion temperature T_i larger than electron temperature T_e, and v) one ion species collected at the negative probe tip. Condition i) can be satisfied if the electron drift velocity $v_d = \frac{j}{ne}$ is small compared to the thermal velocity, $\frac{v_d}{v_{th_e}} \ll 1$. For MS during peak I_z, $j \leq 400$ A/cm^2, $T_e \approx 10$ eV, and $n_e \leq 10^{15}$ cm^{-3} so that $\frac{v_d}{v_{th_e}} \leq \frac{1}{50}$. Condition ii) requires a small Debye length $\frac{\lambda_D}{a} \ll 1$. MS parameters give $\lambda_D \approx 10^{-3}$ mm while the probe diameter $a \approx 1/2$ mm. The ion gyroradius is $\rho_i \approx 1$ mm, which marginally satisfies iii), while the observed Doppler ion

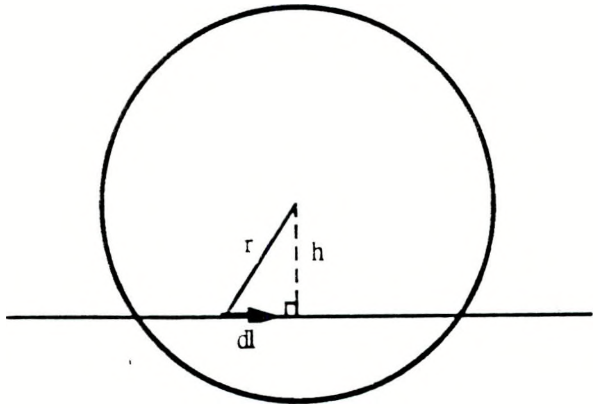

Figure 2.2: Geometry for calculating line integrals in an axisymmetric system.

temperatures (for impurity ions) indicate $T_i \geq T_e$ throughout the spheromak formation and decay.

The electron temperature and ion density are obtained from Equations (2.6) and (2.7) by varying the probe tip bias voltage to map out the $\tanh x$ curve [29]. The slope near V=0 and the saturation current I_o drawn combine to provide n and T_e. Note that the ion saturation current is only weakly dependent on T_e.

2.1.3 Inversion Technique

The line integrated densities $\int n_e\, dl$ obtained by the interferometer were used along with the assumption of cylindrical symmetry to obtain an inverted density profile $n(r,t)$. The technique is based on the Abel inversion of the integral

$$f(h) = \int_h g(r)\, dl = 2\int_h^1 \frac{g(r)r}{\sqrt{r^2 - h^2}} dr \qquad (2.8)$$

where the integral is along a chord described by the chord parameter h as shown in Figure 2.2, and $g(r)$ the desired radial function. A unit circle region is used since all lengths may be normalized to the circle radius. The plane of the page that Figure 2.2 lies in corresponds to the $z = 0$ midplane of MS. The Abel inversion for the desired radial function $g(r)$ in terms of the measured chord function $f(h)$ is

$$g(r) = \int_r^1 \frac{df(h)}{dh} \frac{dh}{\sqrt{h^2 - r^2}} \qquad (2.9)$$

In principle one may measure discrete f_j for several h_j, fit some smooth function $f^{fit}(h)$ to the set $\{h_j, f_j\}$, and calculate Equation (2.9) numerically to an accuracy determined by the number of chords used and their coverage of $0 \leq h \leq 1$. In reality however, the data f_j are often contaminated by uncertainties of noise and shot-to-shot variation, which significantly alter the inverted function g(r) [32,33,34]. In addition, while the plasma magnetic field structure is generally toroidally symmetric to a good approximation, the axis of symmetry may move about, introducing uncertainty in the h_j. The basic problem is that even though (2.9) is a unique and well defined mapping of a point P_h in chord space to a point P_r in radial space, a small ϵ volume of points in chord space around P_h is mapped to a much larger volume around point P_r in radial space.

To minimize the effect of noisy data, one may assume a functional form of $g(r)$ with adjustable parameters a_k, and fit the integral in Equation (2.8) to the measured f_j. The advantage of this technique is that one may use some intuition in selecting the form of $g(r)$ to limit the spurious oscillations of the inversion. The problem with this approach is that one imposes a priori knowledge about the radial function that is possibly incorrect. A compromise solution, first used successfully by Cormack [32] and later refined by Nagayama [34], is to use some intuition to choose a set of smooth fitting functions $g^k(r)$, (k=1,2,...M) that are linearly independent and preferably orthogonal in a loose sense (i.e. the $g^k(r)$ do not overlap one another excessively; $g^k(r) = r^k$ on $0 \leq r \leq 1$ would not be satisfactory, for example). Assuming $g(r) = \sum_{k=1}^{M} a_k g^k(r)$, one has $f(h) = \sum_{k=1}^{M} a_k f^k(h)$. The set of functions

$$f^k(h) = 2\int_h^1 g^k(r) \frac{rdr}{\sqrt{r^2 - h^2}}$$

can be constructed and evaluated at each measured chord h_j (j=1,2,...,N) to give $f^k(h_j)$, and the coefficients a_k are determined by least squares fitting the N data points f_j to the

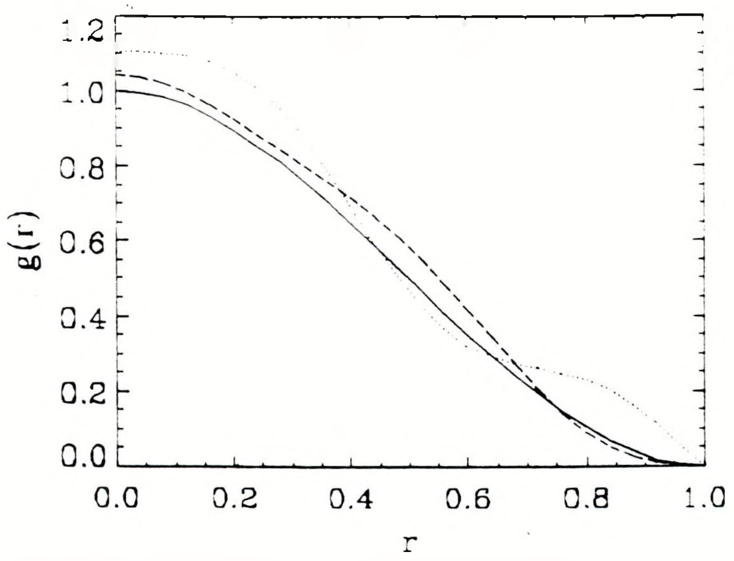

Figure 2.3: Inversion method test, showing original profile (solid) and reconstructed profiles with 20% noise (dashed) and with 30% noise (dotted).

M fitting functions $f^k(h)$.

The $g^k(r)$ used here are zero order Bessel functions [34],

$$g^k(r) = J_o(r\rho^k)$$

where ρ^k is the k^{th} zero of $J_o(x)$. The number of chords N used was between 8 and 11, while the number of coefficients M was varied. As with all fitting algorithms, increasing the number of terms M permitted greater resolution of the radial profile features but also introduced spurious oscillations in the inverted profile. Smooth, physically reasonable (non-negative) inversions were obtained for $M < 5$. The region near r=0 is poorly determined with any inversion scheme, because even the chords passing near the axis have only a fraction of their information weighted from the vicinity of r=0. This is a fundamental effect of line averaging, and produces here inverted density profiles that may show negative density or a positive density peak at the axis.

The inversion scheme was tested by assuming a radial function $g(r)$, calculating line integrals, adding some random noise, and then inverting to compare the result with the original. Figure 2.3 shows a typical test profile and inverted results using the Bessel function method with M=4. Significant distortion is seen for 30% added noise. The Bessel function method was found superior to that of Cormack, although the two methods gave generally similar inverted profiles.

Edge Langmuir probe density data was used to construct additional edge chords to be used in the inversions. Since the probe was not absolutely calibrated, edge data were fit with a polynomial in r (assumed to go to zero at the r=1 boundary) and edge line integrals were calculated using Equation (2.8). Note that the radial Bessel functions used in the inversions all go to zero at r=1, so a large density near the edge would require many terms $f^k(h)$ to invert accurately.

2.2 Apparatus

2.2.1 Interferometer

The multiple beam interferometer is the primary density diagnostic on MS, and is described below. A single beam version of this interferometer was also used temporarily to obtain axial line averaged density. Refer to Figure 2.4 for the locations of the beam paths.

2.2.1.1 Description

The multiple beam quadrature interferometer was located such that the 4 parallel scene beams passed through the lower half of the z=0 midplane of the MS vessel, as shown in Figures 2.4 and 2.5. A 15 mW linearly polarized HeNe (λ = 6328Å) laser light source was used. The initial beam was divided into 4 beams using beamsplitting cubes; to maintain a high degree of linear polarization, polarizing beamsplitter cubes (PBS) were used in conjunction with $\frac{\lambda}{2}$ waveplates. The incident beam's linear polarization angle was rotated to 45° with respect to vertical by passing it through an appropriately oriented $\frac{\lambda}{2}$ waveplate; the beam then passed into the PBS and divided into approximately equal intensity S polarization (deflected 90°) and P polarization (undeflected) beams. The two

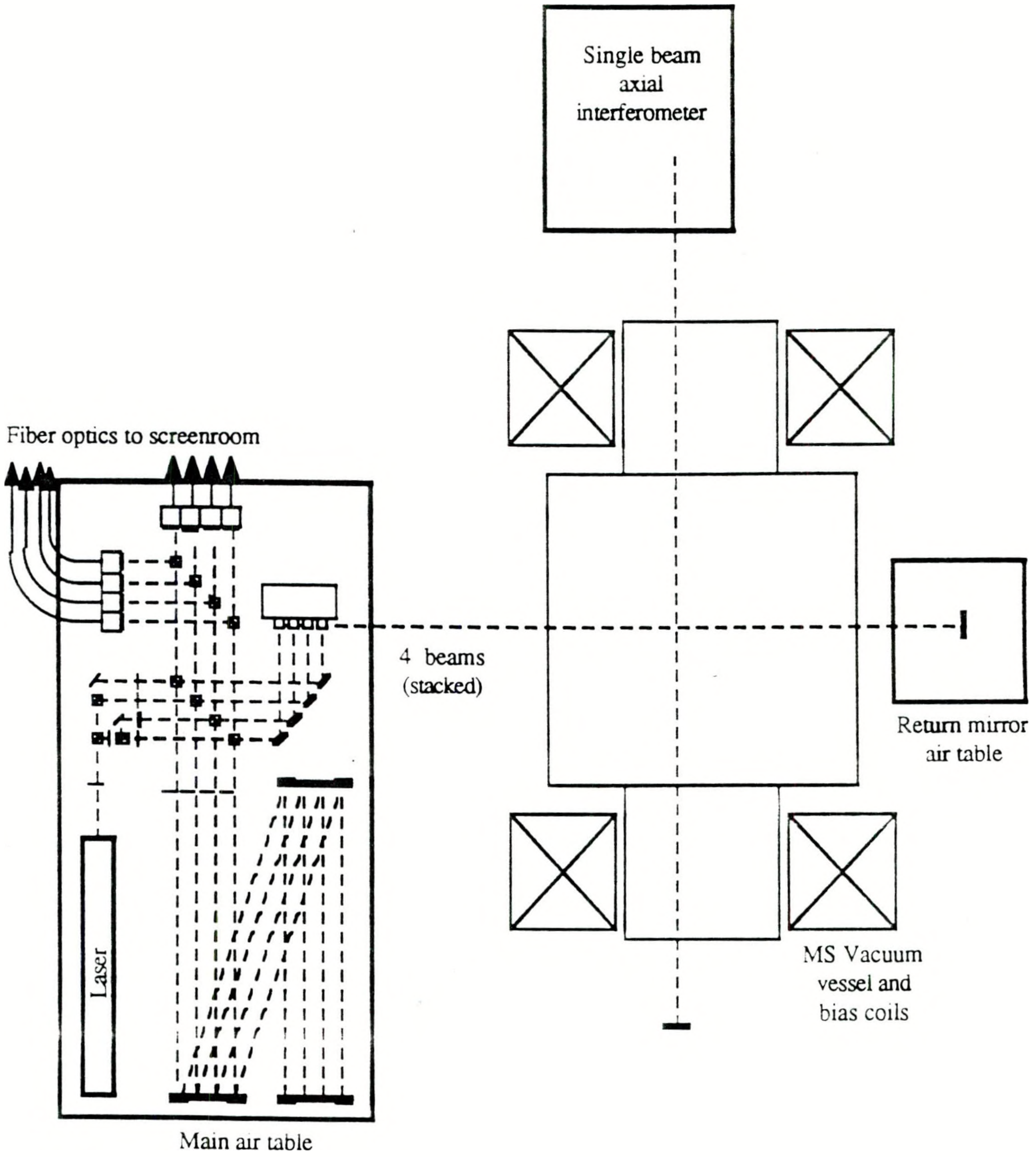

Figure 2.4: Top view of optics arrangement for multi-beam interferometer. Dotted lines indicate laser light paths. Axial beam interferometer is also shown.

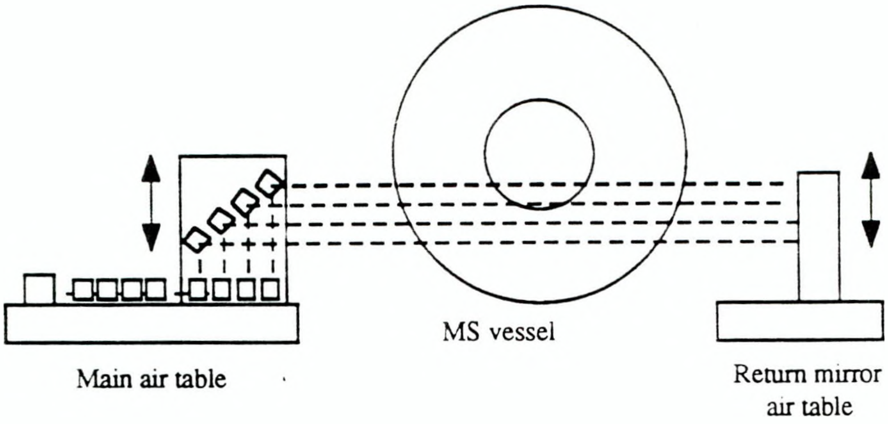

Figure 2.5: Side view of optics arrangement for multi-beam interferometer. Beams can be scanned across lower half of MS midplane.

beams then passed again through $\frac{\lambda}{2}$ waveplates to rotate their polarizations back to 45° with respect to vertical. Repeating the process yielded 4 beams of approximately equal intensity.

Each of these beams was then used in a quadrature interferometer arrangement [26] as described in Section 2.1.1. The main beamsplitting cubes (MBS) were relatively polarization insensitive, with S and P polarization transmittances within 5% of each other. However, the hybrid metal-dielectric optical coatings of the MBS were also approximately 30% absorptive. The $\frac{\lambda}{2}$ waveplates were multiple-order mica type, and the MS vessel windows were 6.4 mm thick fused silica with a 30 arc-minute wedge to direct surface reflections out of the beam paths. The reference beams were folded several times to accomodate the 4.5 m optical path length on the optics table. It was found that the coherence length of the laser was short enough to require the scene and reference path lengths be matched to within 1 cm for maximum fringe contrast. All mirrors were protective-coated aluminum type[1], and the return mirrors on the ends of the scene and reference paths were slightly concave (with a 10 m radius) to refocus the 1 mrad diverging beam from the laser.

---

[1] ER.2 coating, Newport Research Corp.

These mirrors were also slightly misaligned to permit the returning reference beams to pass through the $\frac{\lambda}{2}$ waveplates, and to prevent all the returning beams from feeding back into the laser.

The 4 recombined beams were divided into S and P polarizations by the final PBS cubes, and the 8 polarized beams were each intercepted by a 1 mm diameter plastic fiber optic behind a 6328 $\AA$ notchpass filter. The fiber optics carried the light signals to a screen room. Because the typical fringe's bright or dark band was 1-3 mm wide and only a single band was desired across the end of the fiber optic, the beams were not focussed into the fibers. To maintain the brightest and broadest fringes possible, all transmissive optics were anti-reflection coated for 6328 $\AA$, and all optics' transmitted wavefront distortion was $\frac{\lambda}{4}$ or better at 6328 $\AA$. To minimize vibration-induced fringes, all optics except the scene beams' return mirrors were located on a single air-supported granite optical table, and covered by an acoustic damping enclosure. The scene beams' return mirrors were located on a similar, but much smaller, table about 105 cm from the MS vessel axis. It was found necessary to use non-metallic mirror mounts near the vessel to avoid mirror motion due to the interaction of induced eddy currents with stray I_z magnetic field.

The 8-channel light detection electronics was located in the MS screen room for protection from electromagnetic, electrostatic, and magnetic fields. The 15 m long plastic fiber optics (run through opaque tubing for physical protection and light shielding) from the interferometer optics table were routed to a 1P28 photomultiplier tube array. The current signals were then preamplified and bandwidth limited using transimpedance amplifiers cascaded with active filters. The preamplifier outputs were matched into buffer amplifiers, an 8-channel main amplifier, and an 8-channel digitizer as shown in Figure 2.6. The 18 dB/octave Butterworth-type frequency roll-off of the preamplifier was used to obtain maximum bandwidth without violating the Nyquist sampling criterion at the 0.5 MHz/channel maximum sampling rate of the 8-channel digitizer. The data was read from the digitizer into the MS computer using Camac hardware and MDS/IDL soft-

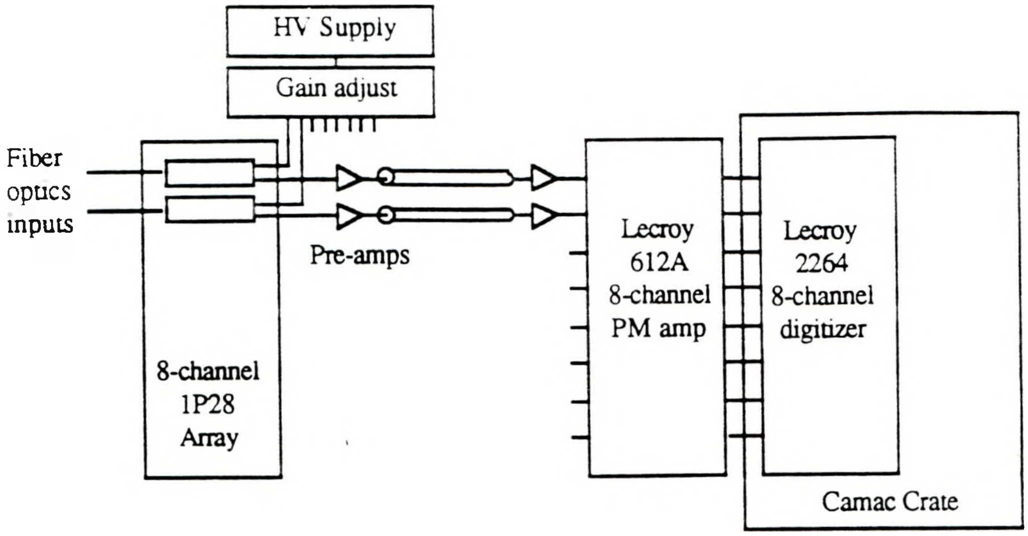

Figure 2.6: Detection electronics shown for one beam (S and P polarization signals) of the multi-beam interferometer.

ware.

In order to obtain an accurate interferometer calibration, the beams were aligned prior to each shot. The table was lightly tapped with a remote plunger about 2 minutes before the shot, and the digitizers triggered to record the relatively slow sinusoidal signals due to the moving optics table. This information was used to establish each signal's fringe amplitude and zero. The resolution of the interferometer was limited by noise in the detection apparatus and laser to $\frac{1}{30}$ fringe, corresponding to a density of about 3×10^{13} cm^{-3}. A full fringe (2π phase shift) corresponded to 1.8×10^{15} cm^{-3} density for 2 passes across the 100 cm vessel diameter. The line density quantity $\overline{n}_e L$ was saved into a database, permitting use with the Abel inversion routines or allowing one to directly view line-average density histories by dividing by the total path length L.

It is important to check that any excited neutral deuterium surrounding the plasma does not contribute significantly to the phase shift of the interferometer beam. The neutral contribution to the index of refraction μ may be written [19]

$$\mu - 1 = \frac{1}{2}\left(\frac{f_{pe}}{f}\right)^2 \left[\sum_{i \neq j} \frac{f_{ij}}{\left(\left(\frac{f_{ij}}{f}\right)^2 - 1\right)} \frac{n_i}{n_e}\right]$$

where the summation is over all transitions from state i to state j, f_{ij} is the frequency of the ij transition, f^{ij} is the absorption oscillator strength, n_0^i is the number density of the neutral excited state i, and f, f_{p_e} were defined previously. For the neutrals to have a negligible effect, the quantity in square brackets must be small compared to 1. The closest deuterium line to $f = 6328\mathring{A}$ is the $2 - 3$ transition at $f_{23} = 6563\mathring{A}$. Since f^{23} is of order 1 and $\left((\frac{f_{ij}}{f})^2 - 1\right) \approx 0.1$, one requires $\frac{n_0^2}{n_e} \ll 0.1$ for a negligible neutral effect. As noted in the next chapter, the formation plasma extended almost to the chamber walls. This edge plasma temperature was estimated to be about 5 eV, from Langmuir probe measurements (see Chapter 3). Since even a temperature as low as 2 eV more than 99% ionizes the deuterium [27], the neutrals' contribution to the phase shift should be negligible.

2.2.1.2 Average Density Decay

To model the time history of the line average density, an equation with a variable source rate S and characteristic particle confinement time τ is used [28],

$$\frac{d\overline{n}}{dt} = S - \frac{\overline{n}}{\tau} \tag{2.10}$$

In general both τ and S are functions of time, but once the spheromak has formed and is simply decaying, a constant confinement time and refueling rate are reasonable approximations [14]. Then the solution of Equation (2.10) is an exponential decay with time constant τ to an asymptotic density $\overline{n}_\infty = \tau S$. Under conditions where a plateau density $\overline{n}_\infty$ was clearly seen, the density decay was fit to an exponential to determine the particle confinement time.

Results of the interferometer measurements are presented in the next chapter.

2.2.2 Langmuir Probe

The edge Langmuir probe had four tips of equal size available for use, although typically only two were connected together as a low impedance double probe, while a third was sometimes used as a high impedance single probe. The probe tips were formed by

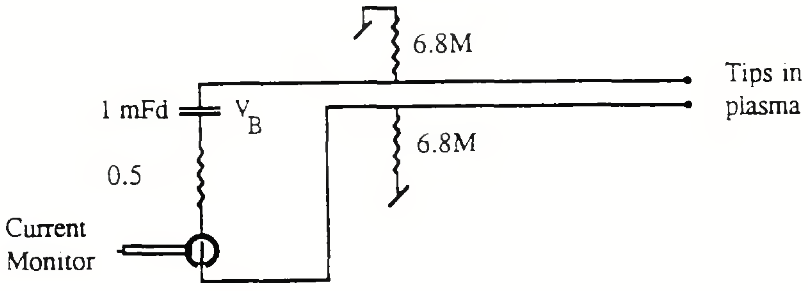

Figure 2.7: Circuit used for Langmuir probe. Current monitor is a Pearson Model #411.

protruding thoriated tungsten wire from thin hollow ceramic tubing; the exposed wire tip was a cylinder of $1.35 \pm .08$ mm length and $0.52 \pm .01$ mm diameter. The wire and ceramic tubing ran along the inside of an evacuated stainless steel shaft to an electrical vacuum-feedthrough. The probe shaft assembly could be moved radially in and out of the edge plasma, and could be rotated to look for electric field effects. About 4 m of RG174 coaxial cable carried the tip signals to a copper box containing the probe circuitry shown in Figure 2.7. Additional wire braid, connected to the copper box and screen room ground but insulated completely from the RG174 and the probe body, was necessary to shield electrical noise pickup. The outer conductor of the RG174 was connected to the probe body, which was connected to the grounded MS vessel. To avoid ground loop problems, it was important to not connect the MS vessel ground to the screen room ground via any MS diagnostics.

The signal from the Pearson current monitor was routed to the digitizers in a manner very similar to those of the interferometer. Approximately 15 m of RG-58 terminated coaxial cable housed in copper shielding carried the signal to the screen room, where it was RC filtered ($f_{3\text{dB}} = 0.2$ MHz), passed through fast buffer amplifiers, and digitized at 0.5 MHz sampling rate. The entire setup was calibrated in place.

The Langmuir probe locations are shown in Figure 2.8 along with typical vacuum poloidal flux surfaces for condition 4503 at the I_z firing time. No midplane ports were

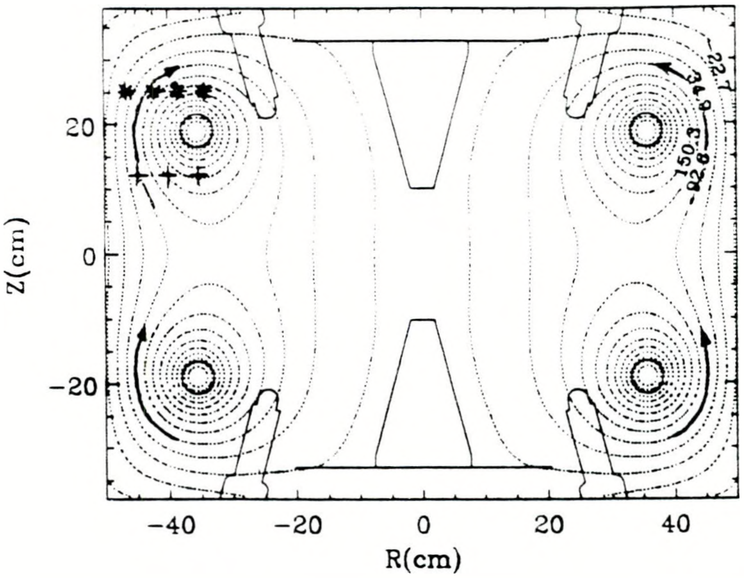

Figure 2.8: Section view of MS interior with vacuum poloidal flux lines (values in mWb) at I_z trigger time. Edge Langmuir probe (+), magnetic probe (*), and outer I_z (arrows) locations are indicated.

available, so the probe was located 12 cm off midplane. The I-V characteristic was checked at the r=40 cm and r=45 cm positions. Figure 2.9 shows typical I-V curves for r=40 cm at two times; reversing the tip bias polarity $V_B \rightarrow -V_B$ gave a reversed current $I \rightarrow -I$ within the shot-to-shot variation. Typically three shots were done at a given tip bias to average out shot variations. The majority of data were taken at r=35, 40, and 45 cm with the probes biased to near ion saturation, V_B=30 V. The bias was zeroed to look for electric field across the tips; this electric field was typically less than 20% of the signal seen at ion saturation, and once the spheromak formed this fraction fell to less than 5%.

The probe tips were heated white-hot under vacuum prior to a data run in order to burn off any resistive oxide layer or impurities [29]. The MS vessel was filled with about 50 mT D_2 and a glow discharge was sustained between a tip and the grounded chamber for about 10 sec, until the tip glowed white hot and stopped sputtering. This procedure greatly improved shot-to-shot reproducibility.

Results from the Langmuir probe measurements are discussed in the next chapter.

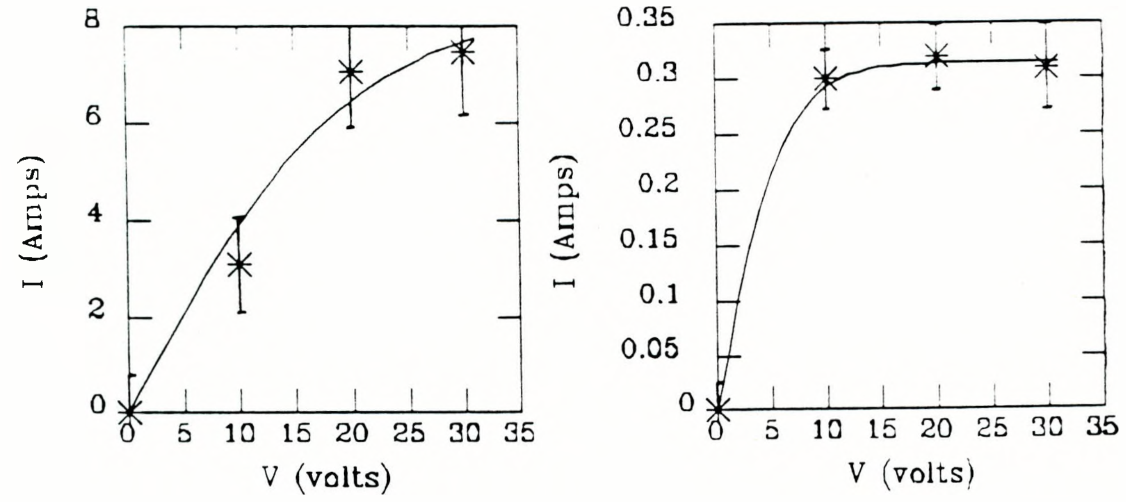

Figure 2.9: Sample fitted I-V characteristics for the Langmuir probe during formation ($t = 8.18$ ms, left) and decay ($t = 8.34$ ms, right).

Chapter 3

Density Observations and Results

3.1 Introduction

The line-averaged density results can be examined in two ways. First, one may look at the time histories of various chord line densities and examine features of the spheromak formation and equilibrium/decay phases. Second, one may use the multiple-chord scans of line density, supplemented with edge density information from the Langmuir probe, to reconstruct the (assumed axisymmetric) radial density profile $n(r,t)$; these reconstructions help to give an understanding of the plasma sources, relation to magnetic equilibria, and density profile evolution.

Figure 3.1 shows a typical time history of 4 interferometer chord line densities. As explained in Section 2.1.1, the line density for any chord is divided by the total chamber pathlength to give a line-average density $\overline{n}$. The overall magnitude, risetime, peaking, and decay of $\overline{n}$ histories are addressed below. Generally, the observed $\overline{n}$ is substantially higher than that expected from fully ionizing the fill gas, and the plasma density decays much faster than classically predicted. Various theoretical models for anomalous particle diffusion are examined at the end of this chapter. The impact of the observed high density on the spheromak's heating and lifetime will be discussed in Chapter 5.

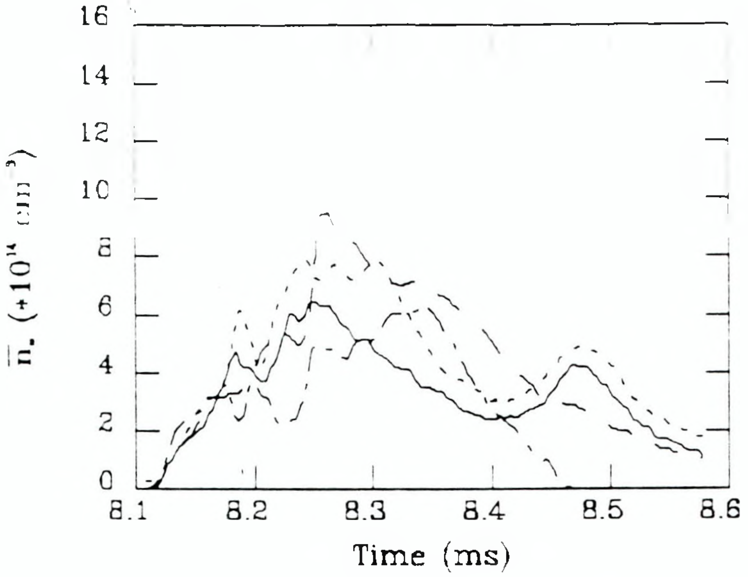

Figure 3.1: Typical 4-chord $\bar{n}$ histories. I_z is triggered at 8.1 ms and the spheromak is fully formed by $t = 8.25$ ms. Chord parameters: h=4 cm (solid), h=11 cm (dotted), h=23 cm (dashed), h=31 cm (dot-dashed).

3.2 Line-Averaged Density

3.2.1 Formation Phase

3.2.1.1 Ionization

The formation period of the spheromak begins with the plasma initiation at I_z trigger time and ends when a fully formed spheromak is evident from the magnetic field structure ($8.1 \leq t \leq 8.25$ ms in Figure 3.1). Figure 1.2 shows typical midplane magnetic field B_z at several radial locations; the spheromak poloidal flux surfaces are fully detached from the reversal coils about 150 μs after I_z is fired.

The I_z current, with the assistance of a microwave preionizer, breaks down the fill gas to create the plasma. The quarter-cycle risetime of the I_z current is typically 75 μs. Figure 3.1 indicates the density initially rises in about this time but then continues to increase for the next $\approx$ 75 μs, attaining its maximum at about spheromak formation time. The fill gas ionization process involves many atomic subprocesses because of the diatomic hydrogen (or deuterium) molecule. Dissociation of the molecule by electron impact dissociation ($H_2 + e^- \rightarrow 2H + e^-$) followed by electron impact ionization of the atomic hydrogen ($H + e^- \rightarrow H^+ + 2e^-$) is the most likely of several ionization paths, based on the rate coefficients at a low initial average temperature of 2 – 3 eV [27]. The overall rate limiting (slowest) process is the atomic hydrogen ionization. Assuming recombination is negligible (a good assumption until a $T = 2 - 3$ eV equilibrium is approached, where the amount of neutral hydrogen becomes much less than the amount of ionized hydrogen), one has an approximate equation for the hydrogen ion density n_i,

$$\frac{dn}{dt} = n_H n_e \langle \sigma v \rangle_{eii} \quad ,$$

where n_h is the atomic hydrogen density, $n_e \approx n_i$ is the electron density, and $\langle \sigma v \rangle_{eii}$ is the rate coefficient for electron impact ionization averaged over a Maxwellian distribution. This gives a very rough estimate of the timescale for ionization

$$\tau_{ioniz}^{-1} \approx \frac{1}{n_i} \frac{dn_i}{dt} = n_H \langle \sigma v \rangle_{eii} \quad .$$

With $n_H \approx 5 \times 10^{14}$ cm^{-3} and $\langle \sigma v \rangle_{eii} \approx 1 - 8 \times 10^{-11}$ cm^{-3}s^{-1}, this gives $\tau_{ioniz} \approx 25 -$ 200 μs, in agreement with that observed. Note that this estimate has a large uncertainty, mainly due to the strong temperature dependence of $\langle \sigma v \rangle_{eii}$ at low temperatures.

3.2.1.2 Other Sources of Plasma

In general, the observed maximum $\bar{n}$ during formation was much higher than that expected from a fully ionized gas fill (a useful "rule of thumb" is that 1 mT of hydrogen (or deuterium) yields an electron density of about $\frac{2}{3} \times 10^{14}$ cm^{-3}). Both static gas fills and dynamic gas puffs are used on MS. In the static case, the gas pressure (and hence density) is known at the time the I_z is fired. The observed maximum density had no systematic dependence on the fully-ionized fill density; however, operating at very low fills did in general produce a lower peak $\bar{n}$. The use of gas puffs gave similar results. The peak $\bar{n}$ were observed to depend most strongly on the machine conditions, both on the

Reversal Coil Covering	Stabilizing Conductors	D_2 Gas Puff p_{final} (mT)	Peak $\overline{n}$ (± 2)	Typical MS Shot #
None	Cones	3	13	2312
Bishop/fiberglass	Cones	12	17	3883
	Funnels	12	22	4049
	None	12	11	4087
Teflon/Ti	Cones	12	10	4284
	"	3	9	4525
(discharge cleaned)	"	3	7	4935
(I_z=1 MA)	"	3	20	4734

Table 3.1: The variation of peak $\overline{n}$ (units of 10^{14} cm^{-3}) with MS vessel interior hardware.

formation currents used and on the material exposed to plasma inside the vacuum vessel. The peak $\overline{n}$ varied to a lesser degree with the use of different fill gases. Comparing peak $\overline{n}$ for different cases is complicated by the fact that the MS experiment had many hardware modifications to vessel interior materials and configurations. The varying sensitivity of peak $\overline{n}$ to the location and type of these materials gives an indication of the source and mechanism contributing to the observed density.

Table 3.1 summarizes the dependence of peak $\overline{n}$ on MS interior hardware. The various stabilizing conductors used are described in Chapter 1. The following sections discuss the correlation of density observations with changes in various MS conditions.

Electrodes

In general, prior to installation of Elkonite electrode tips, the fill gas was readily broken down at fills of 3 mT D_2. This yielded a peak $\overline{n}$ of $5-7 \times 10^{14}$ cm^{-3} with low formation fields (reversal: ± 3.5 kV, I_z: -10 kV, bias: 200 A), and peak $\overline{n}$ of $9-10 \times 10^{14}$ cm^{-3} with higher fields (reversal: ±5 kV, I_z: -13 kV, bias: 350 A). When Elkonite tips were installed, the fill gas density had to be substantially increased to achieve consistent breakdown compared to the stainless steel or tantalum-coated aluminum electrode conditions. In the latter two cases the electrodes showed extensive pitting and surface roughness, while the Elkonite electrode tips have shown much less disintegration in the course of 3–5 times as many shots. While extensive electrode surface deterioration assists the breakdown process and could contribute substantial impurities to the plasma, the observed high densities at low fill prior to use of Elkonite would require a plasma overwhelmingly made up of metal ions and low Z impurities – this plasma would have radiatively decayed away much more rapidly than the observed MS lifetimes (see Chapter 5). In addition, spectroscopic measurements of visible and near-UV impurity line intensities indicate that emission from low Z impurities (O,C) is much more prevalent than that from heavy metallic ions. Instead, the majority of the high density is likely due to surface desorption of trapped gases from material in contact with plasma or formation currents.

Compression

Plasma compressions could also contribute to an increased density, but the magnetic data (refer to Figure 1.2) typically do not show any systematic indication of compressing flux (the increased B_z field seen only near r=0 is not significant because the total flux $2\pi \int rB_z\, dr$ is small there). Plasma-surface interaction is consistent with the generally high level of shot-to-shot variation of even the line-integrated quantity $\overline{n}$ and agrees with the overall tendency for $\overline{n}$ to gradually decrease with repeated shots under the same firing conditions. Table 3.1 shows that the peak $\overline{n}$ is reduced by a factor of 2 simply by removing the copper funnel stabilizing conductors, while changes in the gas puff did not correlate at all with the peak $\overline{n}$ (changes in the gas puff/fill did affect the equilibrium/decay $\overline{n}$ observed – refer to Section 3.2.2).

Surface Effects

Not shown in Table 3.1 are cases where proof-of-principle tests were performed

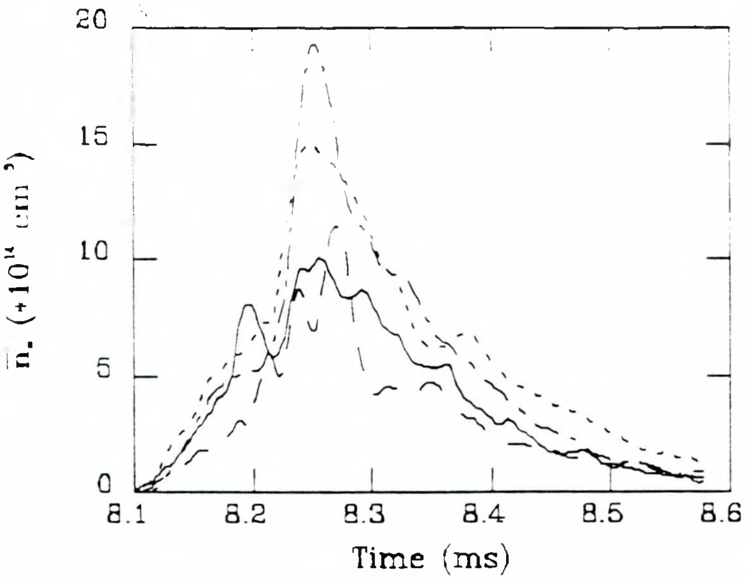

Figure 3.2: 4-chord $\overline{n}$ histories when reversal coil coverings were arcing through. Chords and shot conditions are as per Figure 3.1.

utilizing easily-machineable materials despite the fact that they were known to emit impurities copiously when exposed to plasma. An arc through the titanium-coated, teflon insulated reversal coil wrap gave a 30–40 μs burst of density on the off-diameter chords (see Figure 3.2). The time of appearance of the large density burst due to ionized insulating material begins approximately 120 μs after I_z firing, indicating that surface desorbed impurities reach the path of the interferometer beams at z=0 in about this time.

Similar observations were made when the vessel walls were coated with carbon during discharge cleaning in a methane gas mixture, as well as when the reversal coils were wrapped with a rubberized electrical insulating tape and fiberglass. Note that in this case, as was usually observed, the outer interferometer chords showed the largest $\overline{n}$. In one test, cylindrical polyethylene current barrier sheets were placed inside the MS vessel at r = 35 cm, $|z| \geq 21$ cm to prevent formation I_z current from running outside of the reversal coils. Despite the use of metallic strips on the surface of the polyethylene, substantial amounts of impurities were introduced into the plasma as shown by the large densities of Figure 3.3. The difference between this and previous high density conditions, however, is that $\overline{n}$ appears to rise on the inner chords (near the machine axis) about 40 μs

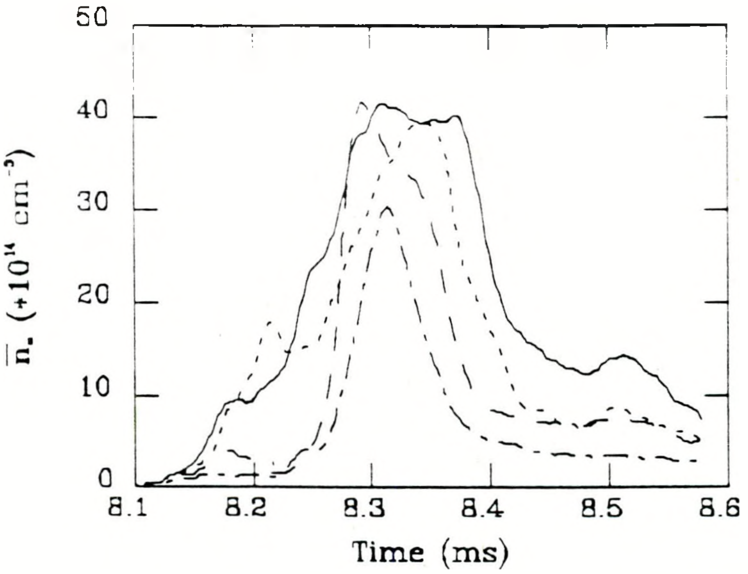

Figure 3.3: 4-chord $\overline{n}$ histories when metal-sheeted polyethylene current divertors were installed. Chords and conditions are as per Figure 3.1.

before it rises on the outer chords. Magnetic probe data confirmed that the I_z current was confined to radii inside the reversal coil (r<35 cm). This was the only condition where the maximum $\overline{n}$ occurred on the inner chords, probably due to impurities traveling along inner radius field lines (see Figure 2.8) across the midplane z=0. The normally observed maximum $\overline{n}$ on outer chords indicates that the density peak is associated with I_z formation current flowing outside (r>35 cm) the reversal coils. This was confirmed with the use of an edge radial Langmuir probe (see Section 3.3), which indicated large density outside the reversal coils for the interval $40 \leq t \leq 130\mu$s (see Figure 3.4).

The chamber walls are another possible desorption surface. Magnetic field measurements near the walls generally show that the outer formation I_z current seems to flow along magnetic field lines, which would keep the current away from the walls. On the other hand, the walls have a large surface area, so a desorption mechanism other than ion or electron bombardment (e.g. photodesorption [27]) could still give rise to the large density observed near the walls during formation. As noted above, when the vessel walls were coated with carbon due to discharge cleaning in methane the observed $\overline{n}$ increased by almost an order of magnitude.

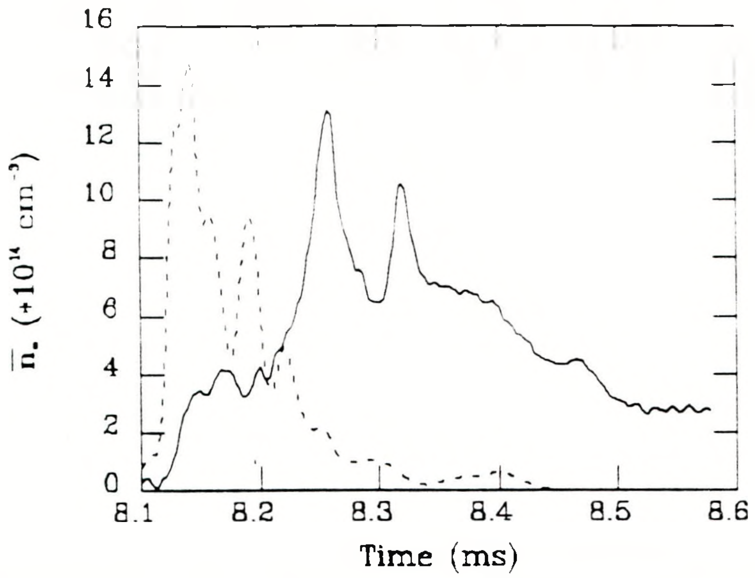

Figure 3.4: Comparison of line-averaged density (solid) at h=23 cm and local edge density (dotted) at r=45 cm. Spheromak is fully formed by t = 8.25 ms.

Reversal Coils

The reversal coils are a likely candidate for the source of desorbed hydrogen and impurities that give the large peak $\bar{n}$. Numerical computations [15] of MS formation have shown $\mathbf{j} \times \mathbf{B}$ velocities directed onto the reversal coil surfaces under some conditions, and the insulating rubberized tape wrapping test mentioned above showed a very large (factor 8) increase in spheromak density. However, early MS conditions with bare stainless steel reversal coils showed a similar peak $\bar{n}$ as when the coils were wrapped in a teflon/titanium combination. Also, Table 3.1 shows that changing the reversal coil wrapping from rubberized tape under fiberglass (very poor materials for proximity to plasma) to teflon tape under titanium foil only reduced the peak $\bar{n}$ by about 50% under the same 12 mT puff conditions. If the reversal coil surface was the critical source of density, one would expect a change of this kind to have reduced the peak $\bar{n}$ by an order of magnitude or more. Thus it appears that the reversal coils, while contributing to the peak $\bar{n}$ are not the primary source of density during formation.

Insulators

The I_z electrode insulators also showed evidence of contributing to the plasma density. These insulators are 3 mm thick cylindrical ceramic sleeves fitted around each electrode. The I_z formation current that flows around the outer radii (r>35 cm, see Figure 2.8) leaves the electrode tip and flows over and around the ends of the ceramic sleeves. The sleeves showed evidence of high surface currents at their ends; and also showed extensive metallic deposits along their lengths to the grounded vacuum vessel bases. The grounded bases around the electrodes also showed evidence of arcs. The arcing indicates that portions of the I_z current not only flow across the end of the ceramic sleeve and along field lines on the outer (r>35 cm) radii, but also flow back along the ceramic sleeve surfaces to the vacuum vessel. Because the I_z circuit cable outer braids are connected to the vessel, a low inductance current path would cause the arcing surface current to flow down one electrode ceramic sleeve to the vessel wall, along the inner wall surface, and down the opposite end ceramic sleeve to the opposite polarity electrode tip.

The ceramic surface (aluminum oxide) is very porous, and traps water both on the surface and in bulk [35]. This desorbed water, along with vaporized aluminum oxide and impurities, would then be dissociated and ionized by the I_z current and energetic plasma electrons, resulting in a high density burst streaming along the field lines. This density burst streaming velocity would have to be about 1.5 cm/μs, corresponding to an ion thermal energy of 4 eV for deuterium. Spectroscopy shows substantial oxygen and aluminum line emission, and the ceramic insulating sleeves are the most significant source of aluminum inside the MS vessel. However, if the insulating sleeves are the primary source of density responsible for the peak $\overline{n}$ one would expect the density to propagate by parallel diffusion along <u>both</u> the outer (r>35 cm) and inner (r<35 cm) I_z current paths. As discussed below (Section 3.3), the outer edge density peaks early in the formation, while the inner density peak $\overline{n}$ is typically observed $\approx 70\mu$s later, at the final stage of spheromak formation.

3.2.1.3 Summary

The formation density rises on the same timescale as the I_z current to a value substantially higher than expected from simply fully ionizing the fill/puff gas. The even larger subsequent peak density was observed to depend strongly on the placement and composition of hardware in the MS vessel, implying that surface desorption and blow-off contribute significantly to the plasma density during formation. There is strong evidence that the I_z electrode insulators are the dominant additional density source, but the low central $\overline{n}$ seen during formation does not support this.

3.2.2 Equilibrium/Decay Phase

Following the peaking of $\overline{n}$ at spheromak formation, the density typically decays on all the chords. The inner chords fall off approximately exponentially to a plateau value as shown in Figure 3.1 for $8.25 \leq t \leq 8.45$ ms. The outer chords fall off toward $\overline{n} = 0$. The different density asymptotes for different chords can be explained in conjunction with magnetic probe observations of the decaying spheromak. Figure 3.5 shows the poloidal flux radial profile at the midplane at various times. At $t \approx 8.35$ ms, the separatrix $\psi = 0$ begins to move radially inward due to a tilt instability (seen in the flux surfaces of Figure 3.5) and the external bias field magnetic pressure beginning to overwhelm the decaying plasma pressure. Figure 3.1 shows that this is also the time that the outer chords $\overline{n}$ begins to fall more rapidly: the shrinking region of well-confined plasma permits more and more outer plasma to escape along open field lines. The collapsing separatrix seen in Figure 3.5 by $t \approx 8.45$ ms also manifests itself as an $\overline{n}$ burst, seen peaking on the inner chords of Figure 3.1 by $t \approx 8.48$ ms. The inverted n(r) profiles show this more clearly in Section 3.3. The burst is the result of the radially inward moving separatrix and flux surfaces dragging plasma in toward the machine axis (in ideal MHD, the "frozen-in" theorem implies that

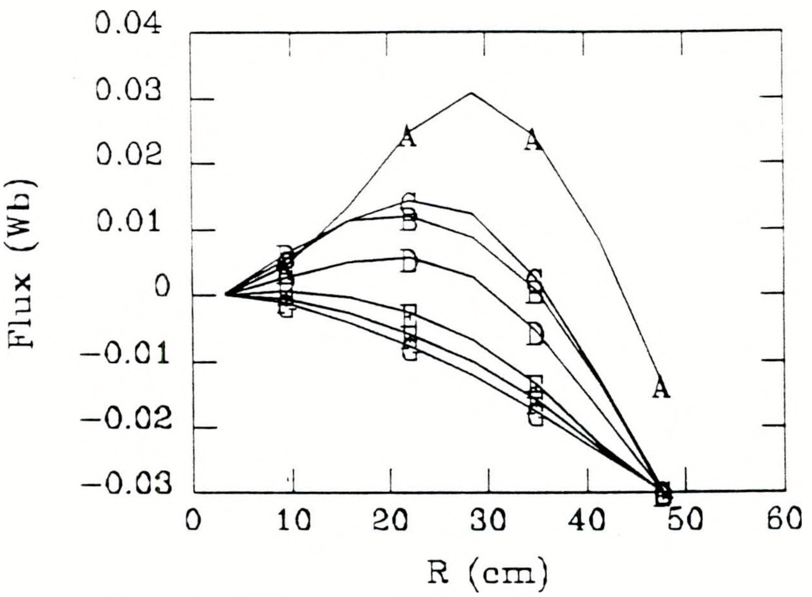

Figure 3.5: Poloidal flux profiles $\psi(r)$ for the shot of Figure 3.4 at times: 8.20 ms (A), 8.25 ms (B), 8.30 ms (C), 8.35 ms (D), 8.40 ms (E), 8.45 ms (F), 8.50 ms (G). The vessel wall is at r=50 cm.

all the plasma would move in with the collapsing flux surfaces; in resistive MHD, a better approximation, the plasma is only partially frozen-in, and some portion is lost onto open field lines as the spheromak separatrix collapses).

3.2.2.1 Density Decay Mechanisms

The overall decay of density can be attributed to several mechanisms. One idea is that the high peak $\bar{n}$ is due to an extremely large impurity presence, and the decay is the result of impurity recombination immediately after formation. However, spectroscopic observations of impurity line emission and computer models of the decay (Chapter 4) show no evidence of an overwhelming low-Z impurity or a significantly ionized high-Z impurity in amounts sufficient to double or triple the ionized fill gas electron density. Another possible reason for the rapid decay is that the interferometer beams were recording a density burst localized near the midplane, and parallel diffusion transported the plasma away from the vicinity of the beams. This too is highly unlikely in that: i) the off-midplane Langmuir probe (Section 2.2) shows its density burst before the interferometer does, ii) the major

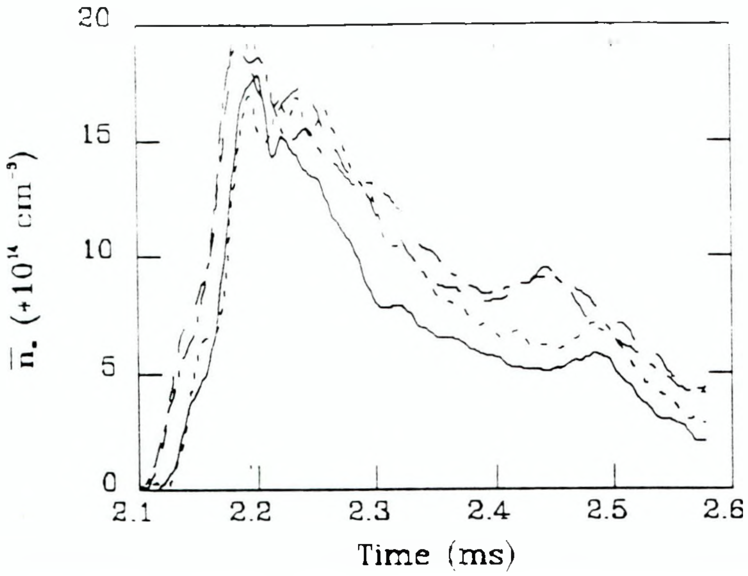

Figure 3.6: Comparison of the $\overline{n}$ decays of the h=0 chord for various static fills of D_2: 6 mT (solid), 8 mT (dotted), 9 mT (dashed), 12 mT (dot-dashed).

candidates for density sources (the walls, the reversal coils, the I_z electrode/insulators) are all off the midplane, and iii) an axial interferometer beam running parallel to the machine axis at $r = 15$ cm showed a very similar $\overline{n}$ decay during the decay phase, not to be expected from a midplane-localized burst diffusing out along flux surfaces. The most likely explanation for the $\overline{n}$ fall-off is that it is due to an average particle confinement time shorter than the spheromak lifetime.

3.2.2.2 Estimating Particle Confinement Time

As discussed in the previous chapter, one may use the $\overline{n}$ decay to estimate the average particle confinement time τ_p. Figure 3.6 shows the $\overline{n}$ decay for the chord near the axis (h=4 cm) for 4 different D_2 gas fills. Note that the $t = 0$ time for the shot of Figure 3.6 was displaced by 6 ms compared to those shots shown in earlier figures. Table 3.2 shows the estimated values of n_o, n_∞, and best fit τ_p values using the decay phase of 150–325 μs after I_z is fired. A value of $\tau_p = 63 \pm 14$ μs was obtained, with no significant variation with chord or fill density. This value also did not change by more than 20% over the range of MS conditions used. The $\overline{n}$ instead varied in peak value and asymptotic, or plateau.

p_{fill} (±.2 mT)	n_o (± 1)	n_∞	τ_p (μs)
6	13	5 ± .5	63 ± 12
8	17	6 ± 1	59 ± 13
9	17	7 ± 2	64 ± 16
12	15.5	7.5 ± 2	67 ± 15

Table 3.2: Initial and final $\overline{n}$ (units of 10^{14} cm^{-3}), and fitted density decay time τ_p from the $\overline{n}$ decays of Figure 3.6.

Wrapping Condition	n_∞ ($\times 10^{14}$ cm^{-3})	S ($\times 10^{18}$ cm^{-3}s^{-1})
Bishop	35 ± 5	54 ± 7
Bishop/fiberglass	5.1 ± .3	7.8 ± .4
Teflon/titanium	5.5 ± .4	8.5 ± .5
Bare coils	5.0 ± .2	7.7 ± .3

Table 3.3: Variation of plateau density n_∞ with reversal coil covering.

value. Shots in which the vessel interior was 'dirty' (the first 5–10 shots after pumpdown, or when the vessel walls were coated with carbon from discharge cleaning in methane, or when plastic materials were used in the vessel) showed higher particle refueling rates, evidenced by the higher plateau densities as discussed in Chapter 2. Table 3.3 summarizes the estimated refueling rates for various reversal coil insulating coverings, derived by assuming a particle loss time τ_p=65 μs. Note that even when the reversal coils were uninsulated the refueling rate was still almost as high as when the coils were wrapped. However, the magnetic configuration in the uninsulated case was asymmetric and unstable.

3.2.2.3 Scaling with Fill

The decay phase $\overline{n}$ at h=0 was observed to vary systematically with the average midplane fill density present at breakdown. Figure 3.7 shows the h=0 chord $\overline{n}$ value, averaged over the decay interval from 50 μs to 150 μs after spheromak formation time, versus the average midplane neutral atomic deuterium density (twice the molecular density) at I_z

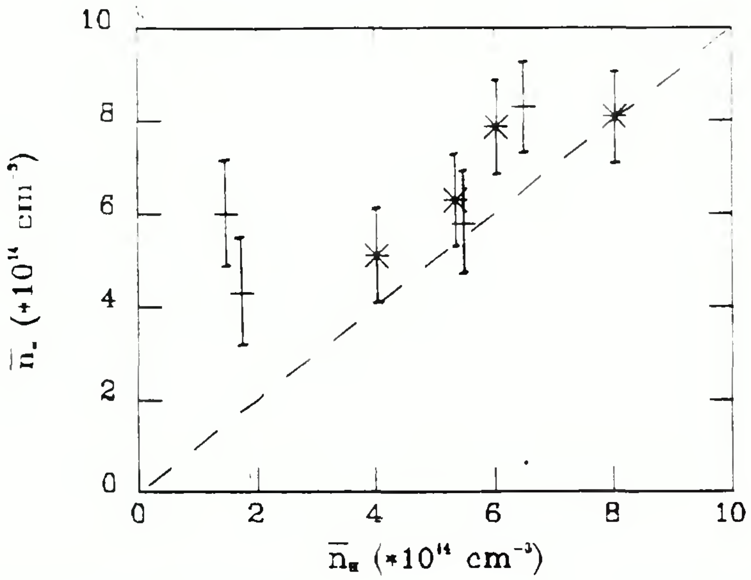

Figure 3.7: Scaling of the observed plateau density n_∞ with the line-average density of the fully-ionized gas puff. Dashed line indicates the $\overline{n}$ expected from a fully ionized fill.

firing time, as obtained using a fast ionization gauge. At higher fills the points are at or just above the level of density expected from fully-ionized fills, but they approach a non-zero constant at low fills. This constant represents an additional fueling source of density.

3.2.2.4 Observations in Helium

Some distinct differences were observed during the decay phase when helium was used as the plasma gas instead of deuterium. Figure 3.8 shows the transverse (h=0) and axial $\overline{n}$ histories in deuterium, while Figure 3.9 shows the same histories in helium. The overall $\overline{n}$ is lower in helium. This may be due to incomplete double ionization of helium at the cooler edge yielding fewer than the two electrons per He atom necessary to match the two electrons per D_2 molecule. Alternatively, the difference may be due to the fact that deuterium is more readily absorbed into metallic surfaces than helium, and thus more deuterium is desorbed during deuterium shots than is helium (and deuterium) during helium shots. The latter would be consistent with the observation that after initially changing over to He, the $\overline{n}$ observed were almost identical to those in D_2; as more He

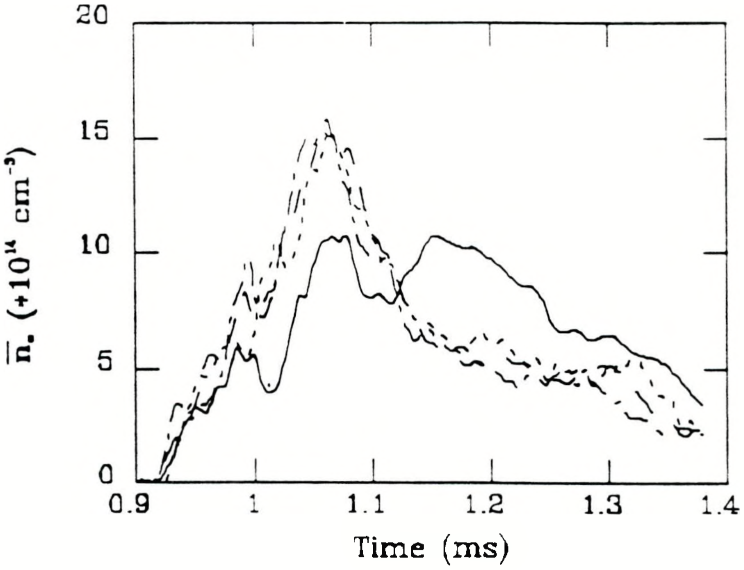

Figure 3.8: Comparison of axial $\overline{n}$ (solid) with midplane $\overline{n}$ chords (dotted) for a shot in D_2. I_z is triggered at 0.9 ms, spheromak is fully formed by 1.05 ms.

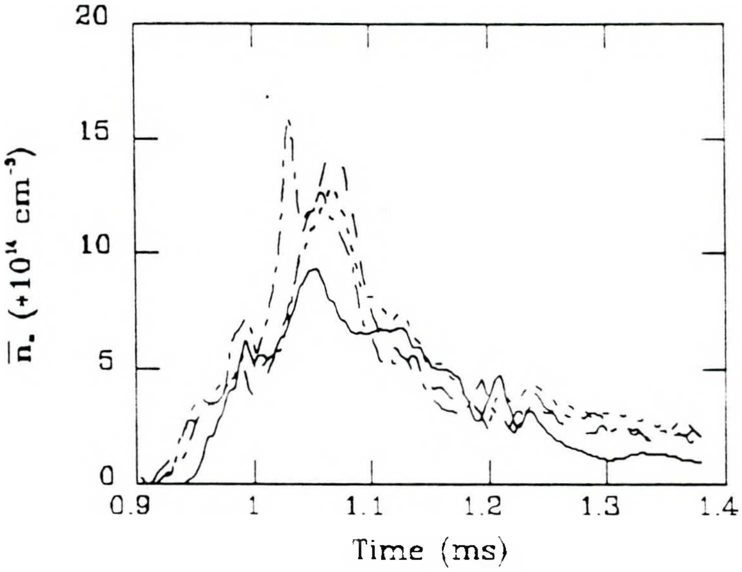

Figure 3.9: Comparison of axial $\overline{n}$ (solid) with various midplane $\overline{n}$ chords (dotted) for a shot in He. Other conditions are the same as for those of Figure 3.8.

shots were taken, the density decreased with each shot until the late-time $\bar{n}$ values were 40-60% of those in D_2.

The greatest difference in Figures 3.8 and 3.9 is in the axial $\bar{n}$ histories. During the decay phase, the axial $\bar{n}$ in He is about half that in D_2. Quantitatively, treating the spheromak plasma as a region of axial length L_p and average density $\bar{n}_p$, and the non-spheromak plasma volume between the walls and end separatrixes as a region of length $L_v = L - L_p$ and average density $\bar{n}_v$, the average axial density may be written $\bar{n} = (L_p\bar{n}_p + L_v\bar{n}_v)/L$. The poloidal flux surface mappings give $L_p \approx 50$ cm, $L_v \approx 30$ cm. The density data of Figures 3.8 and 3.9 give, at $t = 1.18$ ms for example, $(\bar{n}_p)_{D_2} = 7.5 \times 10^{14}$ cm^{-3}, $(\bar{n})_{D_2} = 1.1 \times 10^{15}$ cm^{-3} and $(\bar{n}_p)_{He} = 5 \times 10^{14}$ cm$^{-3} = (\bar{n})_{He}$. One then readily finds that during the decay the average axial density $\bar{n}_v$ outside the ends of the spheromak was about the same as that inside the spheromak in the He case, but it was about 1.5 times that inside the spheromak in the D_2 case. The D_2 shots' larger edge density was likely to have been due to a higher wall desorption rate of D_2. Consistent with this were the observations of the D_β (and H_β, as the spectrometer was not used in a high enough order to resolve the wavelength difference) spectral emission for shots in D_2 and He (Figure 3.10) . During the decay phase, the D_β intensity for He shots was 1/2 to 2/3 the intensity in D_2 shots. Since deuterium is almost fully ionized at $T_e \approx 2$ eV [27], most of the D_β light would have been coming from the cooler edge region near the walls. The fact that so much D_β emission was observed in an He shot implies that substantial deuterium or hydrogen is released from the walls or other surfaces inside the MS vessel during a shot.

3.2.2.5 Summary

The spheromak decay phase can be characterized by an exponential decay of the density to a plateau determined by the particle refueling rate and loss time. The loss time was only weakly changed over the wide variety of MS conditions, while the fueling rate scaled with

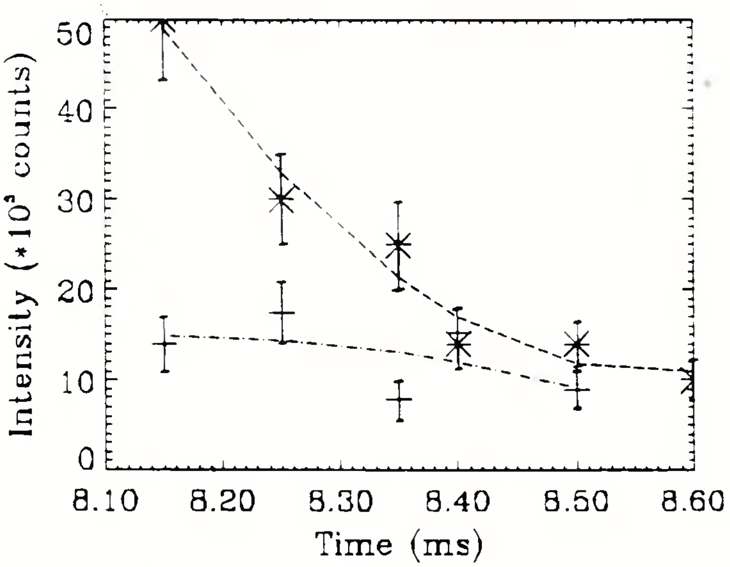

Figure 3.10: Intensity of (H_β, D_β) emission for shots under similar conditions in D_2 (*) and in He (+). Curves are fits to points.

the fully ionized fill only at large densities. Spectroscopy and axial interferometry indicate that during the decay phase the additional density is likely due to desorbed hydrogen or deuterium.

3.3 Radially Resolved Density

With the assumption of axisymmetry, the interferometer line-densities were used to construct Abel-inverted radial density profiles $n(r,t)$. As noted in Chapter 2, the limited chord coverage of the vessel's midplane required supplementing the line-density information with edge densities as measured with a Langmuir probe. It was generally found that the edge density was significant only during spheromak formation.

3.3.1 Edge Density Probe

The probe data gave the local temperature and density histories shown in Figures 3.11 and 3.12. For a probe biased into ion saturation the current signal is only weakly ($T^{1/2}$) dependent on temperature, and since I-V probe scans at r=40 and 45 cm indicated very similar temperatures within the margin of error, the temperature history shown in Fig-

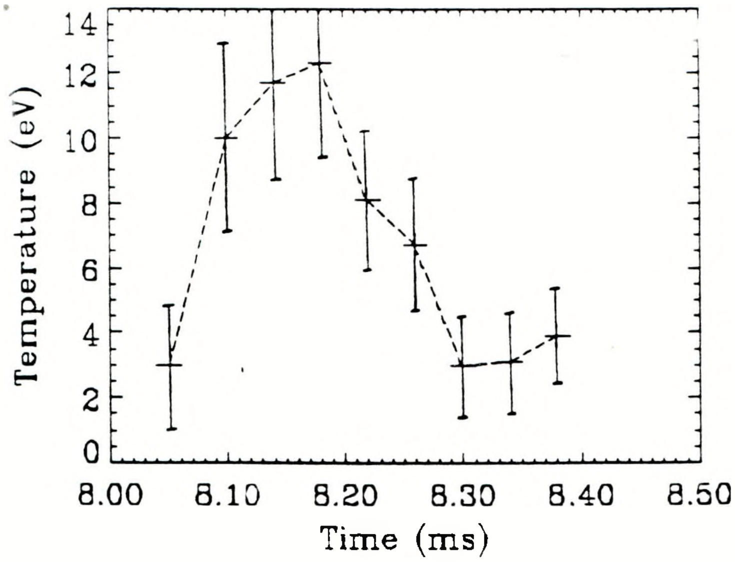

Figure 3.11: Edge electron temperature from Langmuir probe. Note the non-zero temperature before I_z firing time (t = 8.1 ms) due to reversal breakdown of the gas puff.

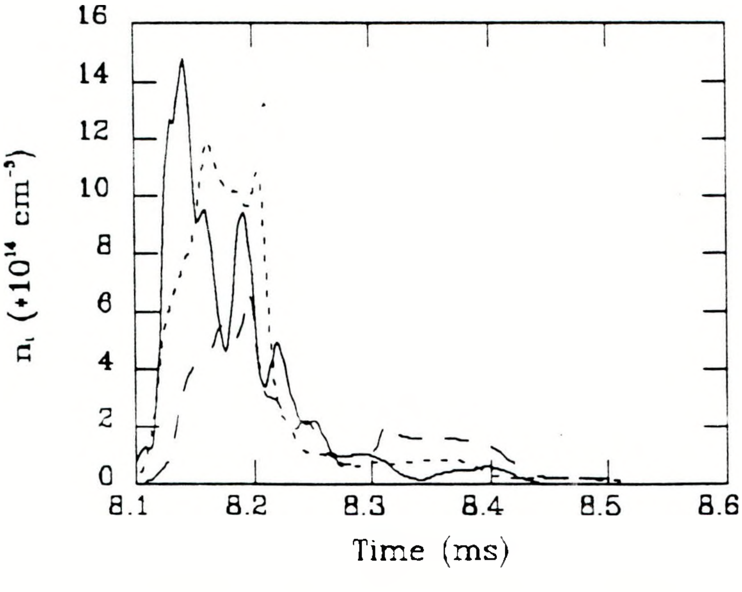

Figure 3.12: Edge ion density from Langmuir probe at r=45 cm (solid), r=40 cm (dotted), and r=35 cm (dashed). Spheromak is fully formed at t=8.25 ms.

ure 3.11 was used at all three radial locations r=35, 40, and 45 cm to derive the density histories shown in Figure 3.12.

The Langmuir probe densities, particularly those at r=40 and 45 cm, show large, irregular behavior for the interval 30–120 μs after I_z fires. Magnetic probes inserted radially at z=25 cm show that the outer I_z poloidal current flows along field lines that pass in the vicinity of $40 \leq r \leq 45$ cm at the Langmuir probe location (indicated on Figure 2.8). The large densities indicated may be due to material released from the I_z electrode insulators traveling along field lines past the Langmuir probe. Figure 3.4 shows how the outer chord interferometer line-densities generally peaked after the Langmuir probe edge density peaked; the data imply that the localized high edge density associated with the outer I_z current is moved into the central spheromak region during formation, leading to a high density spheromak by the time the formation process is complete.

3.3.2 Inversion Results

The edge densities and line-densities were used to construct density profiles $n(r,t)$ by inversion, as discussed in Chapter 2. Edge density data were only taken for a limited number of shots, while interferometer density scans were done under several conditions. However, the edge data only had a significant effect on the inversions for the first 100–120 μs of formation (see Figure 3.13), and the inversion process gave good (i.e. physically meaningful) results only after the first 75 μs of formation. Since the overall density levels were similar in all the interferometer density scans, and the midplane magnetic data showed a similar amount of outer I_z current in all of these cases, the edge density data of condition 5125 were used as typical edge data for all the density scans taken under similar conditions.

3.3.2.1 Profile Features

Figure 3.14 shows selected $n(r,t)$ profiles for the non-peaking shots of MS condition 4503. In the discussion that follows, it is helpful to refer to the density profiles $n(r,t)$ (Fig-

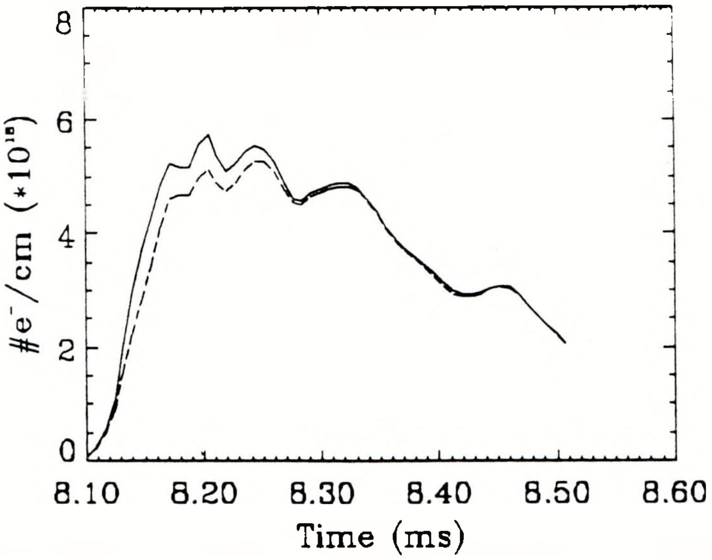

Figure 3.13: Total number of electrons at midplane as derived from interferometer scan of condition 4503. Dotted line indicates effect of using one-half of edge density from Langmuir probe.

ure 3.14), the midplane integrated total number of electrons N(t) (Figure 3.13), the midplane magnetic field probe data $B_z(t)$ (Figure 1.2), and the poloidal current contours I_p (Figure 1.5). The times referred to are the MS event times, $8.1 \leq t \leq 8.5$ ms.

The features of the density profile evolution are as follows. For $t < 8.17$ ms the I_z current and N(t) are rising, the density is very high on the outer (r>35 cm) edge, and the density inversions are not physically meaningful due to large shot-to-shot variation, lack of axisymmetry during early formation, and the limitations of a smooth, fourth-order Bessel function fit to model a largely outer edge localized profile.

At $t \approx 8.17 - 8.18$ ms the I_z has peaked and N(t) stops increasing. The I_p current contours begin moving toward r=0 as the induced reversed current on axis decays away, and the inversions become physically realistic as the outer edge density falls.

By $t \approx 8.21$ ms the I_z is penetrating in toward r=0. The edge density no longer dominates, and the density profile begins to look like a flux function except on the outer (r>35 cm) edge.

During the interval $t \approx 8.22 - 8.245$ ms the closed current and flux surfaces of a

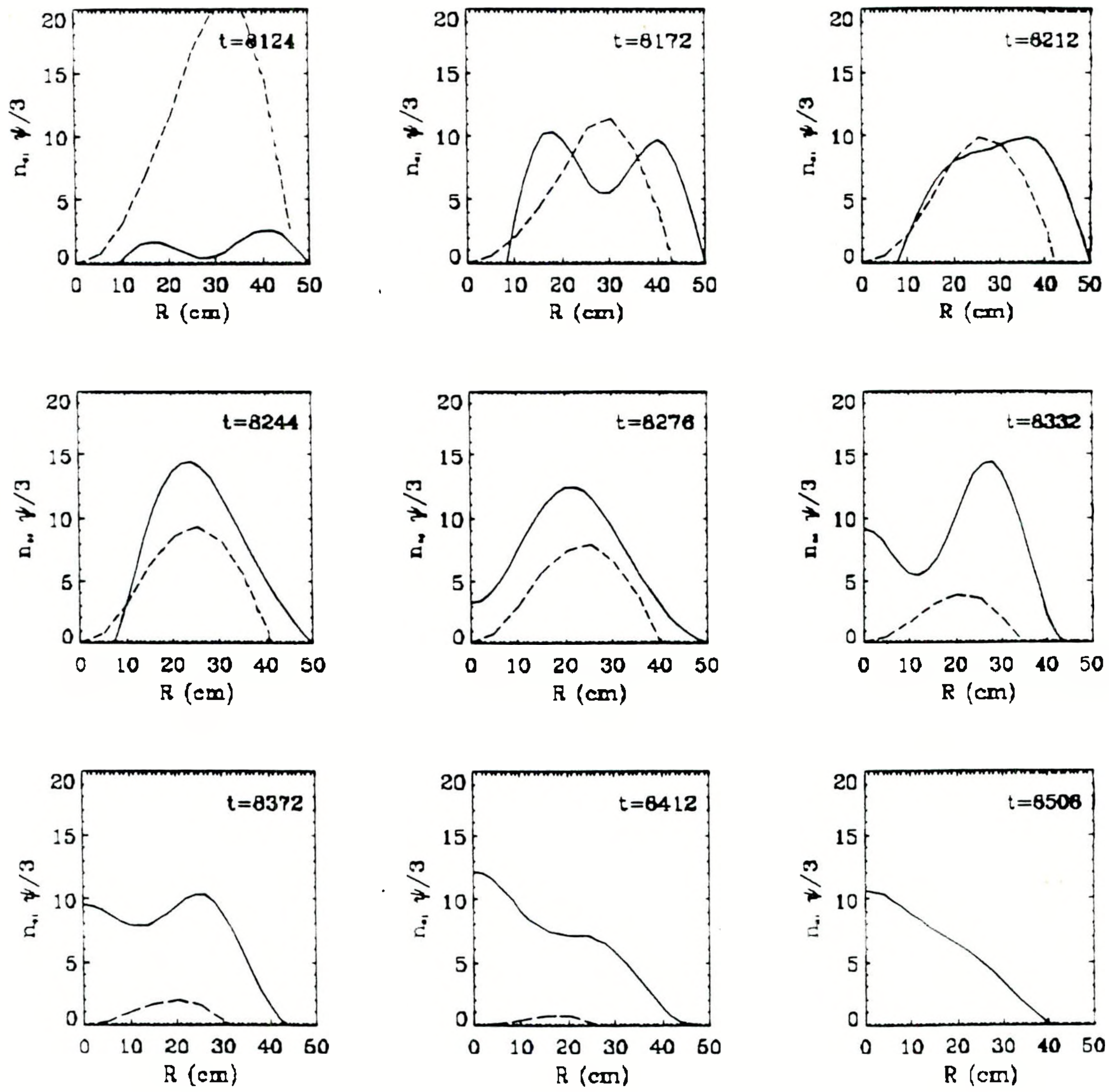

Figure 3.14: Radial density profiles (solid) in units of 10^{14} cm^{-3}, from inversion of chord data for condition 4503. Also shown are the poloidal flux profiles (dotted) in mWb. Note that flux has been divided by 3 for visualization purposes.

spheromak form. The density increasingly peaks at the magnetic axis (maximum poloidal flux location) while decreasing on the outer edge. The fact that N(t) is roughly constant over this period indicates that the density rise at the magnetic axis is due to plasma on the outer edge moving radially inward as the flux surfaces close in to $r \leq 40$ cm.

At $t \approx 8.27$ ms the ripple in $B_z(t)$ indicates a small relaxation event, when N(t) drops slightly and n(r) rises in the vicinity of r=0. Another relaxation event is seen on $B_z(t)$ at $t \approx 8.315$ ms, as n(r) begins to rise even further at r=0. Some tilting of I_p contours is seen.

By $t \approx 8.335$ ms the tilt is clearly present, and N(t) and the poloidal flux begin to drop as plasma is lost. The density at the origin has become significant, due to the tilting field lines channeling more plasma from the nearby aluminum cones. The tilt stops growing by $t \approx 8.35$ ms, under the stabilizing effect of the aluminum cones.

At $t \approx 8.37$ ms another relaxation occurs, increasing the rate of B_z decay and starting the rapid shrinking of the plasma separatrix. The density profile begins to invert so that $n(r = 0)$ exceeds $n(r =$magnetic axis). N(t) continues to fall at about the same rate.

For $t > 8.41$ ms the spheromak magnetic structure collapses, but N(t) levels out and rises slightly. The profiles show that the density continues to decrease except near the origin, where a peaking occurs. The on-axis peaking and slight increase of N(t) may be due to radially collapsing plasma, partially dragged with the rapidly shrinking magnetic field structure, converging on the stabilizing cones to release more gas.

3.3.2.2 Peaking Profiles

The non-peaking type of shot N(t), Figure 3.13, shows that the overall density magnitude originates during the I_z increase, and is mostly localized at the outer radii initially. This is in contrast to the peaking type of shot N(t), Figure 3.15. The peaking shots of condition 5125 were done with helium puffs (equilibrium pressure of 6.5 mT), while the non-peaking shots of condition 4503 shown above were done with deuterium puffs (equi-

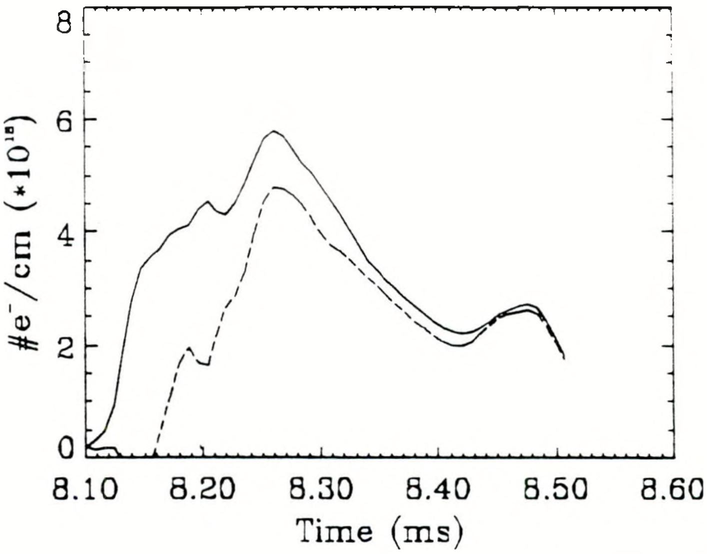

Figure 3.15: Total number of electrons at midplane as derived from interferometer scan of condition 5125. Dotted line indicates total number of electrons for $r \leq 36$ cm, the approximate separatrix size.

librium pressure of 3 mT).[1] The overall lower plasma density of condition 5125 compared to condition 4503, in spite of the higher fill, is consistent with the observation that shots in helium generally gave gradually lower densities as more shots were taken.

Figure 3.15 shows that a burst of about 30% additional plasma is added to N(t) beginning at $t \approx 8.23$ ms, and has decayed away by $t \approx 8.3$ ms. The inverted density profiles, Figure 3.16, at selected times may be compared with those of condition 4503. The main differences are that condition 5125 shows larger density near the origin for $8.18 \leq t \leq 8.24$ ms, and also shows a build-up of density at the magnetic axis for $8.23 \leq t \leq 8.25$ ms. This build-up time coincides with the period of strong magnetic relaxation seen in the $B_z(t)$ data of Figure 3.17 and was commonly observed.

The peaking of N(t) indicates that a plasma source was present, not simply movement of plasma toward the magnetic axis from the edge as in condition 4503. The most likely candidate for this additional source is the reversal coil surface; Figure 1.4 shows that the

---

[1] In general, however, there was no observed correlation of peak density amplitude with the type or amount of puffed gas; different peaking behaviors were observed on successive shots under identical conditions.

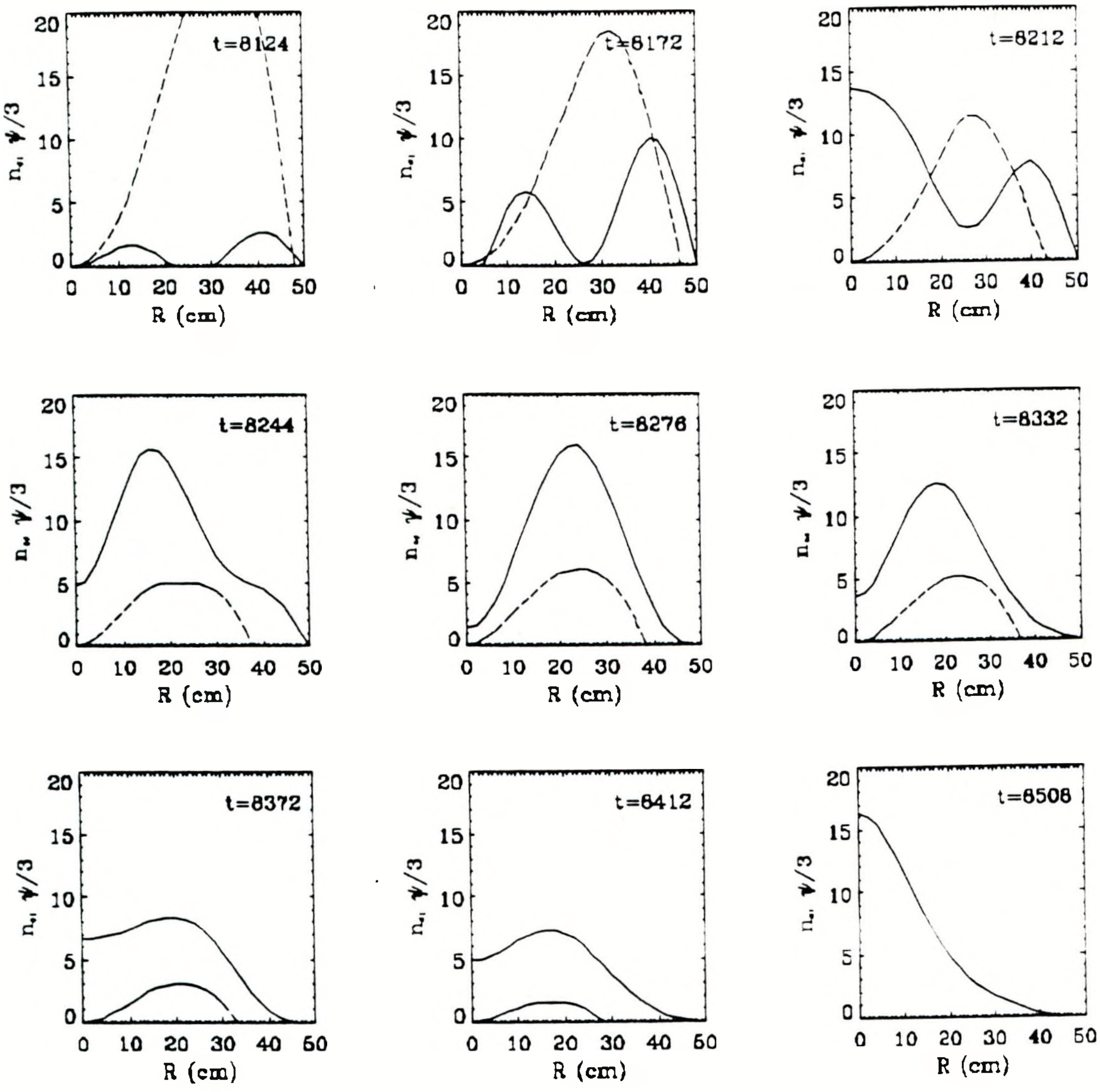

Figure 3.16: Radial density profiles (solid) in units of 10^{14} cm^{-3}, from inversion of chord data for condition 5125. Also shown are the poloidal flux profiles (dotted) in mWb. Note that flux has been divided by 3 for visualization purposes.

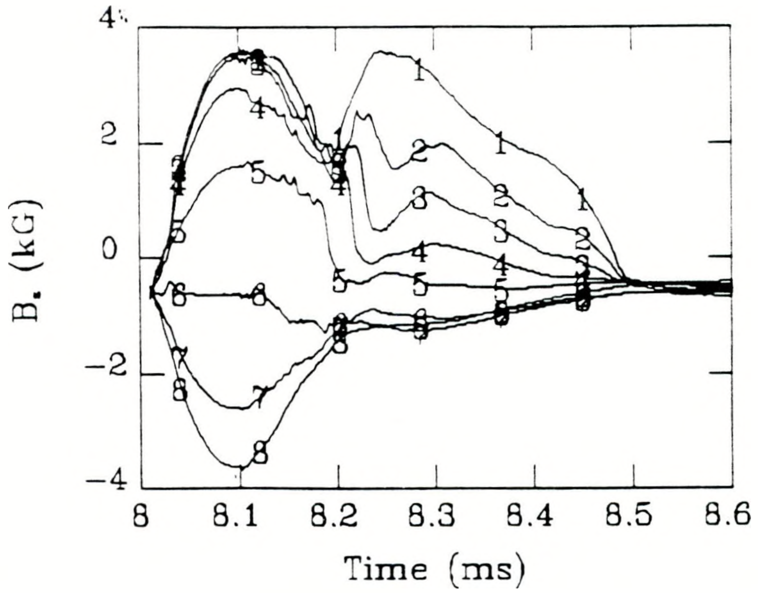

Figure 3.17: Midplane magnetic field B_z for condition 5125. Probe locations are as in Figure 1.2.

density peaking time $8.23 \leq t \leq 8.26$ is exactly the time that the closed flux surfaces form off of the reversal coils. Note that this additional density at spheromak formation, a fraction of the overall density, is to be considered distinct from the density rise which appears earlier in the formation ($t < 8.23$ ms). As discussed in Section 3.2.1, the initial density increase above the fully ionized gas fill is correlated with the I_z timing, vessel interior conditions, and high outer edge density associated with the outer I_z current.

3.3.3 Summary

The inverted profiles obtained with supplementary edge density data show large formation density linked to the outer I_z current. In the non-peaking case, the total number of particles remains approximately constant while the plasma moves radially inward with the flux surfaces at the time of spheromak formation. In the more commonly observed peaking case, the total number of particles and the density near the magnetic axis show a burst of about 50 μs duration at the time that the closed flux surfaces move off of the reversal coil. Plasma interaction with the reversal coil covering is a likely cause of the additional density peak. It is not understood why some shots show the peaking while others do not; the phenomenon is not reproducible, and non-peaking shots are seen much less frequently than peaking shots. Most of the high density observed on MS is associated with the initial density rise, <u>not</u> with the peaking at spheromak formation. It is desirable to limit both the initial density increase as well as the formation peaking in order to obtain hotter spheromaks, as will be shown in the next chapter.

3.4 Theoretical Predictions for Particle Transport

3.4.1 Spheromak Observations

The observed particle confinement time reported in Section 3.2.2.2 can be used in conjunction with the Abel-inverted radial density profiles to estimate an MS particle diffusion coefficient $D_{\perp}^{MS}$. With a density gradient scale length $a_n = n(\frac{dn}{dr})^{-1}$ and a density $1/e$ decay time τ_n, one has an estimated diffusion coefficient $D_{\perp} \approx a_n^2/\tau_p$. For MS, $\tau_n = 63 \pm 14$ μs was obtained from the decay rate of line-average density during the spheromak equilibrium. From the density profiles of Figure 3.14 for $t > 8250$ μs, one may obtain a density gradient scale length estimate of about 10 cm. However, this is an upper bound because of the necessity to limit the number of radial modes when Abel inverting noisy line-integrated data. The higher radial mode information, corresponding to shorter density gradient scale lengths, cannot be resolved. One may use a rough estimate of $a_n = 7 \pm 3$ cm to obtain

$$D_{\perp}^{MS} = 7.8 \pm 6.9 \times 10^5 \qquad \mathrm{cm}^2/\mathrm{s}.$$

The large error is due to the uncertainty of the gradient length scale.

This diffusion coefficient is higher than the classical estimate[2]. As shown by Chen [36], one has

$$D_{\perp}^{cl} = \eta_{\perp} \frac{nc^2(T_e + T_i)}{B^2} \approx 1.0 \times 10^5 \qquad \mathrm{cm}^2/\mathrm{s},$$

for typical MS conditions and classical (Spitzer) resistivity enhanced by an anomalous

---

[2] Note that for typical MS conditions, $\omega_{c_i} \approx \nu_{ii}$, indicating that ions are not magnetically confined. However, the electrons are magnetized and their slower diffusion rate would limit the overall diffusion to the classical ambipolar rate in the absence of neoclassical or anomalous effects.

factor of 3 (see Section 4.2.2.1). This value is lower than the MS estimate for $D_\perp$, but does fall within the uncertainty limits.

A simple Bohm diffusion [30] estimate gives a value in the same range,

$$D_\perp^{Bohm} = \frac{1}{16}\frac{cT_e}{eB} \approx 4.2 \times 10^4 \qquad \mathrm{cm}^2/\mathrm{s}.$$

Bohm-like scaling of particle diffusion is generally considered to be an indication of plasma turbulence [37], with small scale fluctuating electric and/or magnetic fields contributing to the enhanced (over classical) diffusion. A wide variety of turbulent transport models give the T/B Bohm scaling, but they can vary by an order of magnitude in their numerical coefficient. While MS spheromaks formed to date do not cover a wide enough range of parameters to look at scaling, Mayo's local measurements of $D_\perp$ on the S-1 spheromak [38] gave a Bohm-like diffusion coefficient $D_\perp = 5.25 D_\perp^{Bohm}$.

There are several experimental indications of turbulence in MS plasmas. Normalized rms averages of fluctuating quantities of magnetic field $\langle \frac{\tilde{B}}{B} \rangle$ and density $\langle \frac{\tilde{n}}{n} \rangle$ can be estimated from magnetic and Langmuir probe data. Averaging over the frequency range 20 kHz$\leq f \leq$200 kHz, typical values for the decaying spheromak equilibrium of MS condition 4503 are $\langle \frac{\tilde{B}}{B} \rangle \approx 1 - 2\%$, $\langle \frac{\tilde{n}}{n} \rangle \approx 8\%$. These values were measured at the edge of the spheromak, in the vicinity of the separatrix. The edge magnetic field fluctuation amplitude is relatively low compared to the 10-20% often seen on tokamaks, but the density fluctuation amplitude is comparable to tokamak turbulence levels [39]. Another possible indication of plasma turbulence is the large Doppler-broadening of impurity ion spectral lines, indicated by the high ion temperatures in Figure 1.6.

A typical spectrum of $\tilde{n}$ fluctuations, shown in Figure 3.18, does not indicate the narrow peaks characteristic of a few weakly interacting coherent modes of weak turbulence, nor does it show the broad spectrum characteristic of fully developed turbulence [40]. The peaks at 70 kHz and 115 kHz are intriguing; the frequencies are well below those typical of inverse Alfvén transit times ($\approx$ 500 kHz) but are in the correct frequency range for the

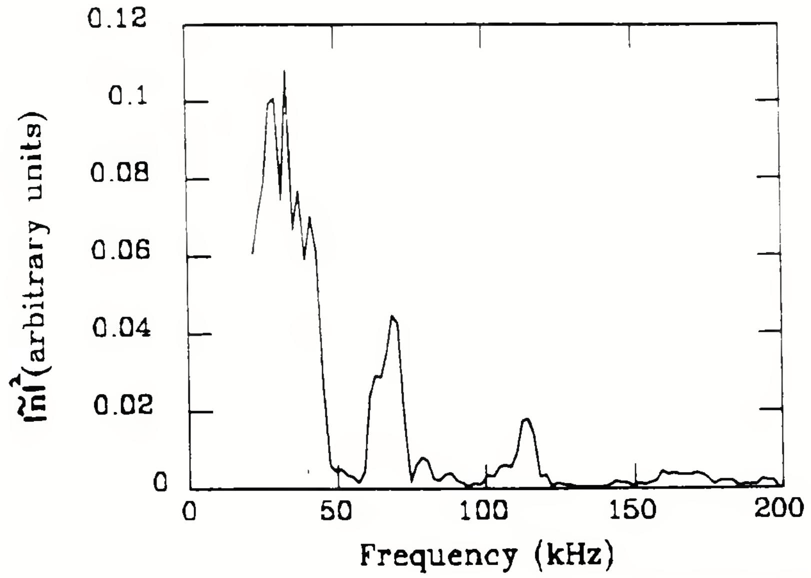

Figure 3.18: Spectrum of density fluctuations, from Langmuir probe located at r=35 cm.

onset of drift waves, as will be shown below.

Ichimaru [37] has shown how strong turbulence enhances fluctuations by a characteristic factor $g^{-1} = n\lambda_D^3$, where λ_D is the Debye length. For MS one has $g^{-1} \approx 500$, indicating strong enhancement. Ichimaru also derives, from very general considerations of the effects of low frequency ($\omega \ll \omega_{c_e}$) electron fluctuations, an anomalous diffusion coefficient

$$D_\perp^{anom} = \frac{\ln(\frac{m_i}{m_e})}{32\pi}\frac{c(T_iT_e)^{1/2}}{eB}\left(1+\frac{T_i}{T_e}\right)^{3/2} \quad . \tag{3.1}$$

If $T_i = T_e$ this gives $D_\perp^{anom} = 3.4D_\perp^{Bohm}$. If the ion temperature is larger than the electron temperature then the diffusion is rapidly enhanced. For example, $T_i = 2T_e$ gives $D_\perp^{anom} = 9D_\perp^{Bohm}$, a value well within the uncertainty of the estimated MS value. Thus, the observed short particle confinement time is consistent with turbulent transport, but a model for the fluctuation mechanism is needed.

3.4.2 Theories for Anomalous Diffusion

The detailed mechanisms of turbulent transport are not well understood presently [39], and there are numerous models for each of a variety of possible instabilities. One may utilize the useful review by Liewer [40] to examine candidate models. The large density gradient, low temperatures, low level of magnetic fluctuations, small scale size of fluctuations, and large fraction of parallel current indicate electrostatic drift waves or MHD rippling modes are the most likely candidates [41]. It should be noted that the electromagnetic fluctuations associated with many instabilities can be strong enough that the stochastic field diffusion component will overwhelm the electrostatic component, giving a diffusion coefficient [42]

$$D_\perp \approx \left\langle \frac{\tilde{B}}{B} \right\rangle^2 D_\parallel^{cl} = \left\langle \frac{\tilde{B}}{B} \right\rangle^2 \left(\frac{\omega_{c_e}}{\nu_{ei}} \right) D_\perp^{cl} \quad .$$

For the high collisionality and low fluctuation level $\langle \frac{\tilde{B}}{B} \rangle$ observed on MS, however, this process would not significantly enhance classical perpendicular diffusion.

Electron drift waves have been cited as the source of anomalous diffusion in previous spheromak studies [38,28]. On MS these modes would be categorized as collisional drift waves since the collisionality is very high,

$$\nu_{ei} \frac{a}{v_{th_e}} = 6.85 \times 10^{-14} a \ln \Lambda \frac{n}{T_e^2} \approx 70 \gg 1$$

where $a \approx 15$ cm is a plasma length scale size. In the linear (non-turbulent) limit, the drift wave typically has a frequency on the order of the electron diamagnetic frequency $\omega \approx \omega_{*_e} = k v_{*_e} = \frac{kcT}{a_n e B}$, where $k^{-1} \approx \rho_s \equiv \frac{c_s}{\omega_{c_i}} \approx 3$ mm. On MS this would correspond to a frequency of about 100 kHz, consistent with the spectrum of Figure 3.18.

Quasi-linear theories of weakly turbulent drift waves typically become invalid when the fluctuation level becomes large enough that the microscopic local density gradient $\tilde{n}k \approx \tilde{n}/\rho_s$ becomes comparable to the macroscopic gradient, $\nabla n \approx n a_n^{-1}$ [40]. For MS this would correspond to a maximum fluctuation level

$$\left\langle \frac{\tilde{n}}{n} \right\rangle < \frac{\rho_s}{a_n} \approx 4\% \quad .$$

The observation of an 8% density fluctuation level on MS would classify the turbulence in the moderate to strong regime.

There are several candidate theories for turbulent collisional drift waves [43,44,45]. The model of Wakatani and Hasegawa [43] predicts a Bohm-like diffusion $D_\perp = 16 D_\perp^{Bohm}$ that agrees with the estimate $D_\perp^{MS}$, but also requires a saturated density fluctuation level $\langle \frac{\tilde{n}}{n} \rangle \approx 2(\frac{\rho_s}{a_n})^{1/2} \approx 35\%$. This is typical of several such models, and indicates that the turbulence in MS spheromaks should be categorized as moderate rather than strong.

The resistive MHD rippling mode is another candidate theory for the anomalous transport [46]. At low enough mode number and high collisionality, strong electron temperature gradients and parallel currents transform the collisional drift wave into the rippling mode [40,47]. In tokamaks and higher temperature spheromaks this instability may be significant, but because MS plasmas are on the low temperature side of a strong low-Z impurity radiation barrier (as will be shown in the next chapter) the electron temperature gradient is expected to be very weak [28].

In conclusion, then, MS particle transport during the spheromak decay phase is consistent with moderate strength turbulence, possibly enhanced by an elevated ion temperature (as indicated in Equation (3.1)). The plasma shows only small indications of magnetic field fluctuations, and turbulent collisional drift wave transport is consistent with the observed density fluctuations and diffusion coefficient estimate. An interesting avenue of further research would be to explore in detail the nature of the turbulent fluctuations on MS using Langmuir probe and magnetic probe measurements, but that is beyond the scope of this work.

Chapter 4

Zero-Dimensional Modeling of Density Data

4.1 Introduction

4.1.1 Motivation

To assess the role of density in MS spheromak formation and decay, the density measurements performed with the interferometer must be correlated with data from other MS diagnostics. To understand the mechanisms underlying the measured density increase at formation, and the behavior during spheromak decay, some model of the density history must be contructed. The model parameters can be determined by a combination of physical arguments and adjustment to agree with MS data. The variation of these parameters allows one to estimate the sensitivity of the model results to any uncertainties, while the scaling of model predictions can be compared with data to improve both the magnitude and functional dependence of parameters.

Once a model has been tested over a regime where MS data has been acquired, it can be used to extrapolate to new regimes of operation, guiding the selection of MS operating parameters. More important, for this study, the model can be used to assess the contributions of various physical processes to the observed MS densities and the spheromak evolution.

4.1.2 Previous Models

Numerous analytic and computational models of compact torus plasmas have been constructed. In general, computer techniques must be used to integrate the non-linear coupled differential equations of realistic models. These computer codes may work in zero dimensions (0-D type), treating volume average quantities, or they may work in some combination of one and two dimensions ($1, 1\frac{1}{2}, 2$-D types).

4.1.2.1 Higher Dimension Models

Two powerful $1\frac{1}{2}$-D spheromak codes have been used to model previous spheromak experiments [48,49]. These codes typically alternate between calculating a 2-D equilibrium and flux surface averages to find transport quantities, and then advancing the plasma quasi-equilibrium in 1-D for several timesteps before recalculating the new 2-D equilibrium. Axisymmetry is always assumed. A serious disadvantage in using these codes for short particle confinement time ($\approx$100-400 μs) spheromaks is that they use a coronal equilibrium (CE) impurity treatment that can seriously underestimate the radiated power loss, particularly in the 10-100 eV temperature range [20]. In addition, with almost no experimental data to indicate otherwise, Schumaker et al. [49] used classical transport coefficients; some of these classical coefficients have since been shown to be inaccurate for spheromaks [50,38]. Nevertheless, their simulations of the Beta II experiment confirmed impurity radiation as the dominant energy loss [51]. A 0-D coronal non-equilibrium model [51] indicated the same result with much less effort than the $1\frac{1}{2}$-D code. Experimental spheromak research is near the point of extensive use of one- or two- dimension spatially-resolved diagnostics, but limited understanding of particle and energy confinement makes the use of higher dimension computer models an unnecessary complication at present.

4.1.2.2 Zero Dimension Models

The 0-D models are constructed by volume integrating the full partial differential equations of plasma evolution and introducing volume averages of the quantities of interest. These codes are substantially smaller and easier to construct than the higher dimension versions, and can be run on personal computers or workstations. The models guide in the device design, and also allow one to explore the parameter space of a plasma device to find optimum operating regimes. However, the 0-D models provide no spatial information, and some plasma processes depend strongly on large gradients typically found at the plasma edge. The magnitude of gradient-dependent terms can only be estimated from observed length scales.

Early 0-D models were power balance codes; they simply attempted to model the observed temperature by accounting for all the input and output powers. Barnes et al. [14] and Meyerhofer [28] have given summaries of early spheromak power balance computer models. These codes worked well modeling cold, radiation-dominated spheromak experiments. It had been anticipated that MS would burn through the low-Z radiation barrier, entering a regime where modeling of other physical processes would be required.

A more recent model by Barnes et al. [14] used the proper coronal non-equilibrium impurity treatment, and included energy loss due to short particle confinement. It is important to take into account the enhanced energy loss due to particle loss. This energy loss will be manifest in several ways [52].

First, a low particle confinement time τ_p will extend the burn-through time of an impurity charge state and can greatly increase the radiated power, because the hot ions lost during the burn-through are replaced by cold ions recycling from the outer plasma region. These cold ions must then be ionized up through their highly radiative states. For example, the work of Carolan and Piotrowicz [20] indicates that for a density of 5×10^{14} cm^{-3}, temperature of 30 eV, and particle confinement time of 150 μs, the oxygen impurity radiation is enhanced by about a factor four over the infinite particle confinement time value. Note that their work also indicates that with the above conditions of electron density and temperature, it would require about 1.5 ms for an impurity distribution to attain coronal equilibrium.

Another effect of short particle confinement time is the energy carried out by lost particles. Using volume averaged quantities in the following arguments, one can estimate the input heating (assumed ohmic) power density Q_{input} for typical MS conditions to be about 300 MW/m^3, using

$$Q_{input} = \frac{B^2}{8\pi\tau_{B^2}} \quad .$$

Here, B≈2.5 kG is the volume average magnetic field and $\tau_{B^2} \approx 70$ μs is the observed magnetic energy decay time. MS estimates are $\tau_p \approx 100$ μs, $n \approx 6 \times 10^{14}$ cm^{-3}, and $T \approx 12$ eV. As explained below, and noted by Meyerhofer [28], each lost plasma particle takes away an average $\frac{5}{2}$T (not $\frac{3}{2}$T) of energy. Thus the power density loss due to convective particle loss Q_{loss} is approximately 56 MW/m^3, as found by

$$Q_{loss} = \frac{5}{2}\frac{p}{\tau_p} \quad .$$

Here $p = n_e T_e + n_i T_i \approx 2 n_e T_e$ is the volume average plasma pressure, and the loss process is treated as ambipolar to maintain charge neutrality.

A third energy loss due to short particle confinement is the energy spent ionizing and reheating the influxing neutral hydrogen and impurities, termed the particle replacement loss Q_{pr}. If neutral hydrogen is electron impact ionized at a rate given by a rate coefficient $\langle\sigma v\rangle_{eii}$ and one has a finite particle confinement time $\tau_p \approx 100$ μs, then in steady state the hydrogen loss equaling the production rate gives an equilibrium neutral density n_o

$$\frac{n_H}{\tau_p} = n_o r \quad ,$$

where r≡ $n_e\langle\sigma v\rangle_{eii}$ and n_H is the hydrogen ion density. Taking $n_H = n_e = 6 \times 10^{14}$ cm^{-3} and $\langle\sigma v\rangle_{eii} = 6 \times 10^{-9}$ cm^{-3}s^{-1} at 10 eV, this implies an equilibrium neutral fraction

$n_o/n_H = (\tau_p r)^{-1} = 2.4\times10^{-3}$. The incoming neutral hydrogen must be ionized, and both the newly created ion and electron must be heated up to the bulk plasma temperature. The heating power required from the plasma's hot thermal electrons and hydrogen ions is proportional to the rate at which this neutral hydrogen is being produced: the total power density loss may estimated to be about 60 MW/m^3, using

$$Q_{pr} = (n_o r)(2(\frac{3}{2}T) + E_{ih}).$$

Here E_{ih} takes into account the energy spent to produce ionized hydrogen and the factor 2 adds up the electron and ion power losses assuming T_e=T_i. $E_{ih} \approx 24$ eV is made up of the 13.6 eV ionization potential of an H atom, and $\approx$ 10 eV required in the ionization process by successive electron excitations [53]. Note that the net 1.5 eV required to dissociate an H_2 molecule [27] is not included here since the neutral hydrogen near the plasma edge will already be in the atomic form, having been photo-dissociated and/or charge exchange lost from the plasma interior.

Finally, since a high hydrogen loss rate requires significant refueling to maintain the steady state density, and this cold refueling neutral hydrogen can charge exchange with hot plasma ions, a charge exchange power loss Q_{cx} due to convecting hot neutrals will exist. This loss can be estimated as $\approx$ 85 MW/m^3 using

$$Q_{cx} = \frac{5}{2} n_H n_o \langle\sigma v\rangle_{cx}(T - T_o) \quad ,$$

where $\langle\sigma v\rangle_{cx}$=$2\times10^{-8}$cm^{-3}s^{-1} (at 10 eV) is the rate coefficient for charge exchange, and T_o is the average temperature of cold edge neutrals, taken to be 1 eV. This convection loss is in addition to any other plasma particle loss rate due to drifting orbits, stochastic edge fields, wave-particle interactions, or other anomalous processes.

None of the particle loss effects listed above dominates the power loss, but the sum of the estimated convection, particle replacement, and charge exhange losses account for about half the estimated ohmic heating power. The remainder is typically due to radiation, enhanced by coronal non-equilibrium impurity distributions. The cumulative effect of short particle confinement time on spheromaks was first noted experimentally by the CTX group [52,14] when they achieved a factor of $\approx$100 reduction in plasma impurity radiation but still could not burn through the oxygen impurity radiation barrier, due to high particle loss and refueling rates caused by the rippled magnetic fields around their mesh flux conserver.

In addition to the Barnes et al. model (which incorrectly used $\frac{3}{2}$T as the plasma energy lost per particle), Meyerhofer [54] constructed a 0-D model to study plasma compression effects on low temperature spheromaks. He used the correct $\frac{5}{2}$T loss and coronal non-equilibrium impurity treatment, but kept the resistivity classical. He also included charge exchange radiation from impurities, but found it to be negligible. However, as shown above, the energy loss due to the convection of charge exchanged hot neutrals can be a significant loss. Most of the processes listed above depend on the product of n_H and n_e, which varies approximately as n^2. This implies that a high density spheromak will have high radiation loss and high particle refueling loss. As will be shown, this imposes a severe clamp on the temperatures achieved on MS.

4.2 Model Description

The 0-D model used here was constructed for several reasons. Although numerous models described above have published results, none uses model parameters sufficiently similar to those of MS. In addition, it was desirable to try to correctly account for the effects of both power and particle balance, as noted in Figure 4.1, using a coronal non-equilibrium impurity treatment. This model is based on that used by Barnes et al. [14], with enhancements and corrections.

One begins with the full system of 2-fluid MHD transport equations, assuming a quasi-equilibrium (i.e. dropping viscous and inertial terms [55]),

$$\partial_t n_{e,i} + \nabla \cdot (n_{e,i} \mathbf{v}_{e,i}) = S_{e,i} \tag{4.1}$$

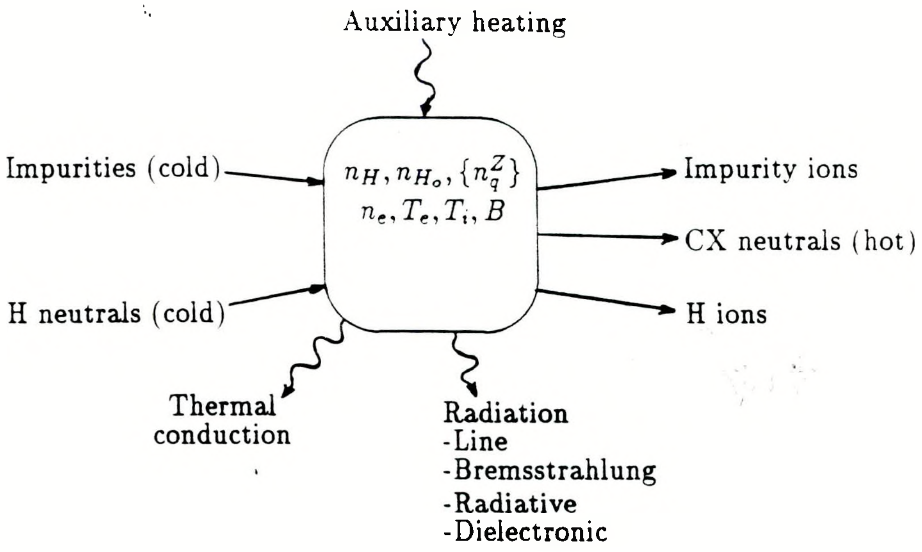

Figure 4.1: Overview of the basic processes modeled by the 0-D code.

$$\frac{3}{2}n_e\frac{dT_e}{dt} + n_eT_e\nabla\cdot\mathbf{v}_e = -\nabla\cdot\mathbf{q}_e - Q_{ei} + \frac{\mathbf{j}\cdot\mathbf{R}_{ei}}{en_e} \tag{4.2}$$

$$\frac{3}{2}n_i\frac{dT_i}{dt} + n_iT_i\nabla\cdot\mathbf{v}_i = -\nabla\cdot\mathbf{q}_i + Q_{ei} \tag{4.3}$$

$$\nabla p_e + en_e(\mathbf{E} + \frac{1}{c}(\mathbf{v}_e\times\mathbf{B})) = -\mathbf{R}_{ei} \tag{4.4}$$

$$\nabla p_i - Zen_i(\mathbf{E} + \frac{1}{c}(\mathbf{v}_i\times\mathbf{B})) = +\mathbf{R}_{ei} \tag{4.5}$$

$$-\frac{1}{c}\partial_t\mathbf{B} = \nabla\times\mathbf{E} \tag{4.6}$$

$$\frac{4\pi}{c}\mathbf{j} = \nabla\times\mathbf{B} \tag{4.7}$$

plus some form of Ohm's law, introducing a resistivity η. The system must in general be solved for the densities $n_{e,i}$, velocities $\mathbf{v}_{e,i}$, temperatures $T_{e,i}$, and fields B and E, assuming some functional forms for the transport quantities: resistivity η, particle source/sinks $S_{e,i}$, heat fluxes $\mathbf{q}_{e,i}$, electron heat transfer Q_{ei}, and momentum transfer $\mathbf{R}_{ei}$. For transport one typically uses classical (Braginskii [56]), neoclassical (i.e. taking into account the toroidal geometry effects), or some anomaly factor times classical, unless an anomalous functional form has been determined experimentally or theoretically. For the impurities, one must add some model of their charge state distribution and radiative processes. A 0-D system is constructed by taking volume averages of Equations (4.1)–(4.3), (4.6), (4.7). The plasma is assumed to be near the force-free state throughout, so that (4.4) and (4.5) give $\nabla p = \mathbf{j} \times \mathbf{B} \approx 0$. The following sections detail how each 0-D equation and its parameters are determined. In what follows, CGS units will be assumed unless noted otherwise, with the exception that temperature is always treated as an energy, in eV.

4.2.1 Hydrogen Particle Balance

The particle balance equations for the majority species (hydrogen is used throughout this chapter) follow from the particle equation of continuity, Equation (4.1). Dropping the e,i subscripts for now, and introducing the volume average

$$\overline{x} \equiv \frac{1}{V} \int_V x \, dV$$

one has

$$\frac{d\overline{n}}{dt} + \frac{1}{V} \int_{\delta V} n\mathbf{v} \cdot d\,\mathbf{s} = \overline{S} \tag{4.8}$$

Note that the volume of interest V is assumed fixed, or varying on a timescale much longer than changes in the plasma parameters n, $\mathbf{v}$, T, etc. The surface integral is the number of particles per unit time leaving the region, denoted by Γ,

$$\Gamma \equiv \int_{\delta V} n\mathbf{v} \cdot d\,\mathbf{s} \quad .$$

One now *defines* a particle confinement time τ_p such that

$$\Gamma \equiv \frac{\overline{n} V}{\tau_p} \quad . \tag{4.9}$$

Intuitively, τ_p is the typical loss time of a plasma particle. Writing explicitly the particle source terms due to ionization and radiative recombination, and dropping the explicit indication of volume averages, one obtains the hydrogen ion continuity equation

$$\frac{dn_H}{dt} = n_o n_e \langle \sigma v \rangle_{eii} - n_e n_H \langle \sigma v \rangle_{rr} - \frac{n_H}{\tau_p} \tag{4.10}$$

where n_e is the electron density, n_H is the hydrogen ion density, n_o is the cold neutral atomic hydrogen edge density (it will be shown later that it is valid to treat the neutrals as both cold and localized to the edge), and $\langle\sigma v\rangle_{rr}$ is the Maxwell-averaged radiative recombination rate. In the parameter regime of MS ($n \approx 5-10\times10^{14}$ cm^{-3}, $T \approx 10-20$ eV) these atomic processes are dominant [57]. Note that charge exchange does not contribute to a change in hydrogen ion density. It should be noted that recent work by Mayo [10] on low density, higher temperature ($n \approx 5 \times 10^{13}$ cm^{-3}, $T \approx 100$ eV) spheromaks has shown that multiple-generation charge exchange transport may lead to a widely varying neutral density concentration in the plasma, with a significant fraction (1-5%) of cold neutrals at the plasma magnetic axis available to charge exchange with hot ions and cause energy loss. These profile-dependent effects are not well modeled in a 0-D code, but charge exchange loss included here is to be interpreted as that which arises from processes near the surface of the volume of interest.

In a similar manner, one has for the neutral atomic hydrogen

$$\frac{dn_o}{dt} = S_H - n_o n_e \langle\sigma v\rangle_{eii} + n_e n_H \langle\sigma v\rangle_{rr} \quad . \tag{4.11}$$

The neutrals are not confined, so a loss time is not applicable. They are assumed to be refueled at a rate S_H by processes at the plasma edge. This refueling rate can play an important role in the energy balance of the spheromak [14].

The rate coefficient $\langle\sigma v\rangle_{eii}$ for hydrogen is taken from Elton [58], while the approximation of Barnes et al. [14] for $\langle\sigma v\rangle_{cx}$ is used. The $\langle\sigma v\rangle_{rr}$ rate coefficient is taken from Post et al. [59], using a convenient analytic approximation form given by Mewe [60].

4.2.2 Power Balance

To obtain the 0-D power balance equation, one begins with the second velocity moment of the kinetic equation [56], neglecting viscosity,

$$\partial_t\left(\frac{mn}{2}v^2 + \frac{3}{2}nT\right) + \nabla \cdot \left\{\left(\frac{mn}{2}v^2 + \frac{3}{2}nT\right)\mathbf{v} + p\mathbf{v} + \mathbf{q}\right\} = en\mathbf{E} \cdot \mathbf{v} + \mathbf{R} \cdot \mathbf{v} + W \tag{4.12}$$

where m is the particle (e,i) mass, q is the flux density of heat (thermal transport), and R is the averaged momentum change of an ion species due to collisions with other species,

$$\mathbf{R} \equiv \int m\mathbf{v}' C d^3 v'$$

(where C represents a generalized collision operator). W is the heat generated in the particle species due to collisions with other species (ohmic heating and electron-ion transfer). Performing the volume average process on Equation (4.12) yields

$$\partial_t(\frac{3}{2}\overline{nT}) + \frac{1}{V}\int_{\partial \mathrm{V}}(\frac{5}{2}nT\mathbf{v})\cdot d\mathbf{s} = Q - Q_{th} \qquad (4.13)$$

where we assume that the internal flow terms are small, $\frac{1}{2}mv^2 \ll \frac{3}{2}\mathrm{T}$. Here $Q_{th} \equiv \frac{1}{V}\int \mathbf{q}\cdot d\mathbf{s}$ is the thermal conduction loss density. The surface integral term can be written (using the Γ defined earlier)

$$\frac{1}{V}\int \frac{5}{2}nT\mathbf{v}\cdot d\mathbf{s} = \frac{5}{2}T_{edge}\frac{\Gamma}{V} = \frac{\frac{5}{2}T_{edge}\overline{n}}{\tau_p} \quad .$$

Here we will use $T_{edge} = \overline{T}$. Note the factor $\frac{5}{2}\overline{T}$ loss per particle arises from the $\frac{3}{2}\overline{T}$ thermal energy lost plus the work $\overline{T} = p/n$ done by the plasma pushing the ion out of the volume [56]. Finally, using (4.8), $\frac{d\overline{n}}{dt} = \overline{S} - \Gamma = \overline{S} - \overline{n}/\tau_p$ in (4.13) and dropping explicit volume average notation, one has the energy density balance equation

$$\frac{3}{2}n\frac{dT}{dt} = Q_{oh} - Q_{th} - Q_{work} - Q_{pr} \quad , \qquad (4.14)$$

where $Q_{work} = nT/\tau_p$ is the plasma work power density of lost particles, and $Q_{pr} = \frac{3}{2}nTS$ is the power density required to heat up the newly created particles from source S (particle replacement power). Note that thus far Q was considered the collision heating term, but one may include any other heat gain or loss terms as well. The forms of the various power densities Q_j are now considered.

4.2.2.1 Ohmic Heating Q_{oh}

The input power to the electrons is from ohmic heating, the thermalizing of relative electron-ion acceleration in the presence of an applied electric field. Assuming an Ohm's law $\mathbf{E} = \eta \mathbf{j} - \mathbf{v}/c \times \mathbf{B}$ in the plasma[1] one has

$$Q_{oh} = \frac{1}{V} \int \mathbf{j} \cdot \mathbf{E} dV = \overline{\eta j^2} \equiv \eta^* \bar{j}^2. \tag{4.15}$$

If j in the plasma is assumed known (either by measurement or by fitting a standard force-free magnetic field solution [9]), one can calculate $\bar{j}$; relation (4.15) then defines an effective resistivity η^* [10]. Numerous researchers have found that if classical Spitzer-Härm resistivity η_{sp} is used, one must assume an anomalous factor κ_{sp} of 2–4 in $\eta^* = \kappa_{sp}\eta_{sp}$ to agree with the observed field energy decay rate [14,61]. Alternatively, one may use no anomaly but instead argue that since most of the helicity decay occurs in the outer plasma regions, some temperature $T_{edge} < T^* < \{T_{central}, \overline{T}\}$ should be used [61]. The first case uses $T_e^* = \overline{T}$, with κ_{sp} adjustable (typically $\kappa_{sp} \approx 2 - 4$). The second uses $\kappa_{sp} = 1$ but $T_e^* = f\overline{T}$, where f is adjustable (typically $.1 < f < 1$). The use of κ_{sp} or T_{edge} is equivalent. One has, with T_e in eV,

$$\eta^* = \kappa_{sp}\eta_{sp} = 5.75 \times 10^{13} \frac{\kappa_{sp} Z_{eff} f(Z_{eff}) \ln \Lambda_{ee}}{T_e^{3/2}} \qquad \text{(sec)}$$

where $Z_{eff} = \langle Z^2 \rangle / \langle Z \rangle$, $f(x) = (.582 + .418x^{-.7})$ is an approximation of the Spitzer-Härm correction for Z dependence [62], and $\ln \Lambda_{ee} = 24 - \ln(\frac{n_e^{1/2}(cm^{-3})}{T_e(ev)})$ is the Coulomb logarithm. Note that η_{sp} here is the parallel resistivity, since in a force-free spheromak $\mathbf{j} \parallel \mathbf{B}$.

Anomalous (non-Spitzer) resistivities have been proposed. It has been noted that when the drift velocity of elecrons becomes a significant fraction of their thermal velocity, current-driven microinstabilities may result in enhanced resistivity [63,42]. A necessary condition for this instability to arise is $v_d/v_{th_i} > \mathcal{O}(1)$. An empirical resistivity first proposed by Chodura [64] was used by Milroy and Brackbill [63] in modeling field-reversed pinches

$$\eta_{ch} = \frac{m_e \nu_{anom}}{ne^2}, \qquad \nu_{anom} = C_1 \omega_{p_i} (1 - e^{-\frac{v_d}{f v_s}})$$

---

[1] A more generalized Ohms's law including a Hall term will not change the dissipation loss.

where $v_d = j/ne$, v_s is the ion sound speed, ω_{p_i} is the ion plasma frequency, and f, C_1 are parameters (typically $f = $, $C_1 = 1$). For a spheromak with $j = \lambda B$ one has

$$\frac{v_d}{v_{th_i}} = 6.5 \times 10^{14} \frac{B(\mathrm{kG})}{n_i (T_i)^{1/2}} \quad .$$

Typical MS parameters given above, with $B \approx 2.5$ kG, give $v_d/v_{th_i} \approx .8$. This value lies in the intermediate regime, making enhanced resistivity possible but not likely to have a significant effect.

4.2.2.2 Thermal Conduction $Q_{th_{e,i}}$

Tokamaks report neoclassical ion thermal conduction agrees reasonably well with observations [40,65], and computational studies of spheromak particle orbits indicate that neoclassical effects may be even less important in spheromaks [66]. Consistent with other models [14,54], classical ion thermal conduction is used here [56]

$$Q_{th_i} = 6.28 \times 10^{-15} \frac{T_i^{1/2}}{a_T R_s B^2(\mathrm{kG})} \sum_{Z,q} \left[(n_q^Z q^Z)^2 (\frac{m_z}{m_p})^{1/2} \ln \Lambda_i \right] \frac{\mathrm{erg}}{\mathrm{cm^3 s}}$$

where a_T is the thermal gradient length scale, R_s is the spheromak separatrix radius, m_z, m_p are the impurity ion mass and hydrogen ion mass respectively, and q^Z, n_q^Z are the impurity ion charge and density of the species characterized by atomic number Z. One also has

$$\ln \Lambda_i = 23 - \ln \frac{Z_{eff} n_e^{1/2} (q^Z)^{1/2}}{T_i^{3/2}} \quad .$$

The use of classical ion thermal conduction is valid even when the ions are not completely magnetized, $\omega_{c_i} \tau \approx 1$, as is the case with MS condition 4503.

Electron thermal conduction is much less certain. Some of the processes that can enhance classical or neoclassical transport of heat in tokamaks are [65] drift waves, trapped electron modes, tearing modes, drift-tearing modes, magnetic 'flutter', and stochastic fields. Generally, anomalous (i.e. non-neoclassical) particle transport will also imply anomalous electron heat transport. One indication of the possibility of anomalous transport, as mentioned above, is the drift speed of electrons becoming significant. MS parameters give $v_d/v_{th_i} \approx \mathcal{O}(1)$, and other hotter spheromaks have a similar value of this parameter due to their lower densities. The intermediate value of this parameter makes it difficult to firmly predict the role of microinstabilities in transport. However, spheromak transport is certainly not classical in general, as discussed in Section 3.4.

A possible reason for enhanced thermal conduction is a stochastic magnetic field B. A cross-field thermal conduction coefficient $\kappa_r = \langle \frac{\tilde{B}}{B} \rangle^2 \kappa_{\|}$ due to stochasticity has been found previously [61], and was used in a 0-D model of the S-1 spheromak to account for part of the power loss not due to particle refueling or radiation. The S-1 team reported fluctuating fields with $\langle \frac{\tilde{B}}{B} \rangle \approx .02 - .1$ [61], and CTX spheromak results show $\langle \frac{\tilde{B}}{B} \rangle \approx .05 - .1$ [67]. However, as Levinton et al. [61] noted, enhanced thermal conduction due to stochastic B requires that the observed $\tilde{B}$ be due to field breaking and reconnection; it is possible that instead the $\tilde{B}$ seen resulted from moving plasma dragging field while the spheromak relaxed into lower-energy states. On MS, much smaller levels of fluctuating magnetic field were observed (Section 3.4). There is still no satisfactory explanation for the anomalously large field decay rates observed in hotter CTX [67] and S-1 [61] discharges.

The MS spheromak is much denser (factor 10) and cooler (factor 4) than the spheromaks mentioned above. In fact, a large drift parameter characteristically indicates significant enhanced transport in the low-density limit. Since $\frac{v_d}{v_{th_e}} \propto \frac{1}{n\sqrt{T_i}}$, devices in which n drops extremely low typically see a global plasma disruption [68,69]. For MS, on the other hand, the drift parameter is of order 1 despite the high n because the temperature is so low. The high density is the most likely reason for the low temperature limit, as will be shown. Cold, dense plasmas have been shown to be radiation-dominated in power loss experimentally [51], theoretically [70], and computationally [48]. The MS magnetic field data show very little $\tilde{B}$ ripple once the spheromak has formed. Rather, the field decays smoothly with abrupt bends where a global Taylor relaxation occurs [8]. This is characteristic of radiation dominated decay [70]. Thus, for simulating radiation dominated decays on MS, satisfactory forms for the electron thermal conduction are enhanced classical, with [56]

$$Q_{th_e} = 3.52 \times 10^{-18} \frac{n_e^2 T_e^{1/2}}{a_T R_s B^2} \ln \Lambda_{ei} \qquad \frac{\text{erg}}{\text{cm}^3\text{s}} \tag{4.16}$$

or a Bohm-type, with $\kappa_{th_e} = nD_{Bohm}$,

$$Q_{th_e} = 6.00 \times 10^{-25} \frac{n_e T_e^2}{a_T R_s B} \qquad \frac{\text{erg}}{\text{cm}^3\text{s}} . \tag{4.17}$$

In practice, both forms were tried, but the power loss due to thermal conduction was found to be small, compared to that due to refueling and radiation. Typically, the 100-times enchanced classical thermal conduction was used. In the typical MS parameter range, the Bohm-type conduction is a factor 2–3 times classical. To determine even the scaling of Q_{th_e}, one requires a detailed knowledge of all power balance terms in the spheromak, or a condition where thermal conduction is a dominant loss process. Since $\langle \frac{\tilde{B}}{B} \rangle$ is very small on MS, stochastic-field enhanced thermal conduction is not significant. Thus, as will be shown below, the dominant losses are radiation and particle refueling loss.

4.2.2.3 Particle Replacement $Q_{pr_{e,i}}$

The power density reheating loss due to a refueling source S was shown previously to be $\frac{3}{2}nTS$. In the 0-D code, one needs to know the rate of production of new, cold electrons and ions, and the energy required to heat them to the average temperatures $T_{e,i}$. For the electrons one has approximately

$$Q_{pr_e} = (Z_{eff} S_o + n_e n_o \langle \sigma v \rangle_{eii})(\frac{3}{2} T_e + E_{ih}) \tag{4.18}$$

where $Z_{eff} S_o$ represents the number of newly created electrons from influxing (at rate S_o) ionizing impurities, and E_{ih} is the average energy required to produce a hydrogen ion. Typically $E_{ih} \approx 25$ eV as explained in Section 4.1.2.2 [14].

For the ions, one assumes that they originate as neutral atoms in a low temperature (T_o) blanket outside the spheromak. Thus,

$$Q_{pr_i} = \frac{3}{2}(S_{imp} + n_e n_o \langle \sigma v \rangle_{eii})(T_i - T_o) \quad . \tag{4.19}$$

4.2.2.4 Electron-Ion Transfer Q_{ei}

Classically one has electron heating via ohmic power, with ions heating due to classical electron-ion collisions. This forces $T_i \leq T_e$. The extent that T_e and T_i decouple depends on non-classical heating and on the ion energy loss rate relative to the electron-ion transfer input rate. At lower ($T \leq 20$ eV) temperatures, the ion losses are small enough that $T_i \approx T_e$. The classical transfer power density from electrons to a particular ion species {Z,q} is of the form [56]

$$Q_{e/z} = \frac{3m_e}{m_z}\frac{n_e}{\tau_{e/z}}(T_e - T_i)$$

where $\tau_{e/z}$ is the electron-ion collision time. Thus one may write

$$Q_{ei} = 7.47 \times 10^{-21} \frac{n_e}{T_e^{3/2}} \left[\sum_{Z,q} n_q^Z (q^Z)^2 (\frac{m_p}{m_z}) \ln \Lambda_{ei} \right] (T_e - T_i) \qquad \frac{\text{erg}}{\text{cm}^3\text{s}}. \tag{4.20}$$

On MS, strong Doppler broadening of impurity spectral lines may indicate ion temperatures $T_i > T_e$ during the spheromak formation phase, but these lines decrease rapidly in both spectral width and intensity once the spheromak is formed (see Chapter 1).

4.2.2.5 Charge Exchange Loss Q_{cx}

Charge exchange processes create a complex behavior at the edge plasma [71]. One idealizes the plasma edge region as three zones: i) an inner hot plasma, ii) a transition zone of influxing cold neutrals, charge exchange hot neutrals, and multiple generation intermediate temperature neutrals, iii) an outer blanket beyond the separatrix. This outer blanket contains cold neutrals, escaping hot charge exchanged neutrals, and charge exchanged ions being lost along open field lines. Refer to Figure 4.2.

By estimating some mean free paths and process rates, and making some assumptions, one can greatly simplify this picture. First, assuming typical parameters $n_H \approx 5 \times 10^{14}$ cm^{-3}, $T_i \approx 15$ eV, the mean free path for an incoming cold neutral ($T \approx 1$ eV) to charge exchange is $\lambda_{mfp} = \frac{v_{th}}{n_H \langle \sigma v \rangle_{cx}} \approx 1$ mm. Actually, electron impact ionization can also occur at these temperatures since the rate coefficients are of similar order.

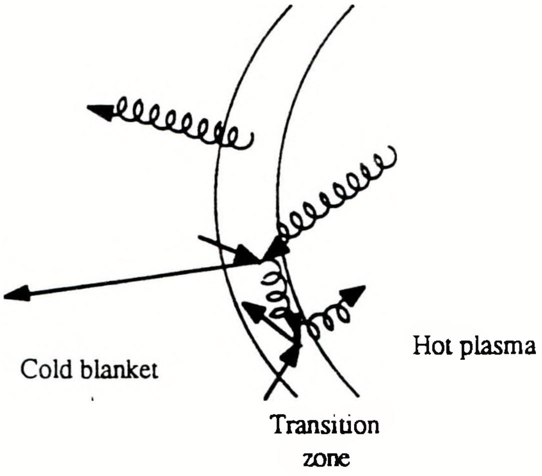

Figure 4.2: Some of the plasma edge charge exchange processes.

$\langle\sigma v\rangle_{cx} \approx 2.2 \times 10^{-8}$ cm^3/s and $\langle\sigma v\rangle_{eii} \approx 0.7 \times 10^{-8}$ cm^3/s, so that the reaction rate is $[n_H\langle\sigma v\rangle_{cx} + n_e\langle\sigma v\rangle_{eii}]^{-1}$ and $\lambda_{mfp} \approx 0.6$ mm. Thus, the charge exchange interactions take place in a zone of characteristic thickness $l_{cx} \approx .6$ mm. Next, one notes that the time required to heat the newly-created cold ions is [55]

$$\tau_{heat} = 7.18 \times 10^6 \frac{T_i^{3/2}}{n_H \ln \Lambda_i} \qquad \text{sec}$$

which gives $\tau_{heat} \approx .05 - .1$ μs. This value is about the typical time between ionization events calculated above, and one now makes the simplifying assumption that all incoming cold hydrogen neutrals that charge exchange are heated up to become thermalized plasma ions before they charge exchange again.

When the incoming cold neutrals charge exchange with a hot plasma ion, the newly created hot neutral may travel beyond the separatrix before its next charge exchange event, or it may go back into the plasma. Since the mean free path for hot hydrogen atoms is $r_{mfp} \approx 3$ mm, one has the much simplified picture of the charge exchange edge region shown in Figure 4.3. The rate of hot hydrogen ions lost due to charge exchange in the edge region is

$$\frac{n_H}{\tau_{cx}} = g n_H n_o \langle\sigma v\rangle_{cx}$$

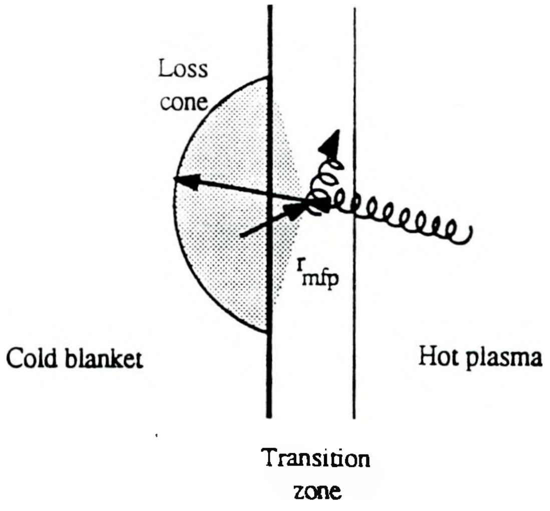

Figure 4.3: Simplified picture of the plasma edge charge exchange processes.

where $g \approx .4$ is the fractional solid angle of the loss cone, determined from the charge exchange zone thickness l_{cx} and the mfp of hot neutrals r_{mfp}. The loss of plasma energy due to escaping charge exchanged hot neutrals (not including charge exchange recombination - see Section 4.2.2.7) is

$$Q_{cx} = Q_{pr}^{cx} + Q_{work}^{cx} = g\frac{5}{2}n_H n_o \langle \sigma v \rangle_{cx}(T_i - T_o) \quad . \tag{4.21}$$

4.2.2.6 Work Done Pushing Out Particles $Q_{work_{e,i}}$

As noted above, there is a power density loss due to the work done by the plasma in pushing out plasma particles. This power density is of the form $\frac{nT}{\tau_p}$, where τ_p is the loss time defined by relation (4.9). Allowing for differing confinement times for impurities (τ_{imp}) and hydrogen (τ_p), one has for electrons

$$Q_{loss_e} = T_e\left(\frac{n_h}{\tau_p} + \frac{\sum_{Z,q} q^Z n_q^Z}{\tau_{imp}}\right) \quad . \tag{4.22}$$

and for ions

$$Q_{loss_i} = T_i\left(\frac{n_h}{\tau_p} + \frac{\sum_{Z,q} n_q^Z}{\tau_{imp}}\right) \quad . \tag{4.23}$$

4.2.2.7 Radiated Loss Q_{rad}

Numerous processes in the plasma lead to the emission of radiation and loss of energy. The plasma is treated as optically thin to this radiation [55,57]. The non-equilibrium coronal radiation (CR) model is used for the impurity ions charge state population, since the MS spheromak lifetime and particle confinement time can be less than that required for coronal equilibrium (see Section 4.1.2.2). This model treats the ions of a given charge as being in their ground state; when they are collisionally excited they are assumed to immediately radiate back down to the ground state. Accounting for electron transitions of the types free-free (Bremsstrahlung), free-bound (radiative and dielectronic, since three-body recombination is unimportant in this regime [72]), bound-bound (line emission), and charge exchange, one may write

$$Q_{rad} = P_b + \sum_{Z,q}(P_{rr} + P_{dr} + P_l + P_{cx}) \quad . \tag{4.24}$$

The forms of the various terms are detailed below.

The Bremsstrahlung emission is given by a form due to Post et al. [59].

$$P_b = 1.53 \times 10^{-25} n_e^2 Z_{eff} T_e^{1/2} \quad \frac{\text{erg}}{\text{cm}^3\text{s}}. \tag{4.25}$$

Note that this form is already summed over the impurity charge states and species.

Radiative recombination radiation is the energy radiated by an electron when it is captured by an ion into the ground state or into an excited state with subsequently decay to the ground state. The emitted power density is [55]

$$P_{rr}(q, Z) = 1.69 \times 10^{-25} \frac{n_e}{T_e^{1/2}} q^2 n_q^Z \chi_{q-1}^Z \quad \frac{\text{erg}}{\text{cm}^3\text{s}} \tag{4.26}$$

where χ_{q-1}^Z is the ionization potential of the recombined ion.

Dielectronic recombination radiation occurs when a free electron's kinetic energy is low enough that it excites a nearby ion in passing, but it then does not have enough energy to escape the ion's attraction; if the ion de-excites, the formerly free electron is captured.

The power density emitted by this processes may be estimated by [59,20]

$$P_{dr}(q,Z) = n_e n_q^Z \langle\sigma v\rangle_{dr}(\chi_{q-1}^Z + E_{excite}(q,Z)) \tag{4.27}$$

where E_{excite} is the excitation energy to the lowest excited state, and the rate coefficient $\langle\sigma v\rangle_{dr}$ used is given by Aldrovandi and Pequignot [73].

The line radiation is the most difficult to estimate accurately. In reality the ground state ions are collisionally excited and then radiatively decay down through a complex set of excited levels back to the ground state, with possible re-excitation during decay. The CR model treats the collisionally excited ions as simply decaying radiatively straight back to the ground state. Then one may write [20]

$$P_l(q,Z) = n_e n_q^Z \sum_{j=1}^{N} \langle\sigma v\rangle_{eie}{}^j \triangle E^j \tag{4.28}$$

where $\langle\sigma v\rangle_{eie}{}^j$ is the excitation rate coefficient to the jth level and $\triangle E^j$ is the excitation energy of this level with respect to the ground state. N is the number of transitions considered. In the lower temperature regime of MS spheromaks (T < 50 eV), C and O impurity radiation is expected to dominate. Tabulated rate coefficients [74] of the strongest resonant transitions of C and O were examined, and the largest contributions to Equation (4.28) were used: typically $2 \leq N \leq 4$. The relatively recent compilation of rate coefficients by Phaneuf et al. [74] are considered even more reliable than those in the highly used ADPACK radiation subroutines of Hulse [75]. The error introduced by limiting the number of lines considered is not much more than the overall quoted uncertainty of 20-50% of Phaneuf et al.'s rates, and certainly within the spirit of a 0-D calculation. The radiated power calculated by the code for a case where coronal equilibrium was also applicable compared well with the values given by the model of Post et al. (see Section 4.3).

The charge exchange recombination radiation is produced when the charge exchanged electron, left in an excited state, radiatively decays down to the ground state. Note that this process can only be counted as a net loss of plasma energy when the newly created hot neutral remains confined by a second charge exchange event (i.e. the hot neutral does not fall in the loss cone of Figure 4.3). As with line emission, this process in general involves consideration of the complexity of transitions. An approximation first introduced by Hulse et al. [76] sets the radiated energy to be the full ionization potential of the recombined ion.

$$P_{cx}(q,Z) = (1-g)n_o n_q^Z \langle\sigma v\rangle_{cx} \chi_{q-1}^Z \quad . \tag{4.29}$$

The charge exchange rate coefficients $\langle\sigma v\rangle_{cx}$ for the impurities considered (C,O) are taken from Phaneuf et al. [74].

4.2.3 Impurity Particle Balance

As mentioned in Section 4.1.2.2, a non-equilibrium coronal radiative (CR) model for the impurity ions is used. Ionization processes used are electron impact ionization and charge exchange, while recombining processes are radiative and dielectronic recombination. Two parameters are introduced: the characteristic particle confinement time τ_{imp} and a neutral impurity refueling rate S_{imp}. Thus one may write

$$\begin{aligned} \frac{dn_q^Z}{dt} &= n_{q-1}^Z n_e \langle\sigma v\rangle_{eii} - n_q^Z n_e \langle\sigma v\rangle_{eii} + n_{q+1}^Z n_e \langle\sigma v\rangle_r - n_q^Z \langle\sigma v\rangle_r \\ &\quad + n_{q+1}^Z n_o \langle\sigma v\rangle_{cx} - n_q^Z n_o \langle\sigma v\rangle_{cx} - \frac{n_q^Z}{\tau_{imp}} + S_{imp}\delta_{q0} \quad . \end{aligned} \tag{4.30}$$

where

$$\langle\sigma v\rangle_r \equiv \begin{cases} \langle\sigma v\rangle_{rr} + \langle\sigma v\rangle_{dr} & , q < Z \\ \langle\sigma v\rangle_{rr} & , q = Z \end{cases} \quad .$$

The initial population distributions are set to correspond approximately to those of a 1 eV plasma (the temperature used for the code start-up); the code physics quickly (in a few μs of simulation) adjusts the distribution to that required by the plasma conditions, and overall simulations results are insensitive to any reasonable variations in startup distribution. Rate coefficients for electron impact ionization are taken from Phaneuf et al. [74], while all other processes' coefficients' references have been previously stated.

4.2.4 Current Density Evolution

The ohmic heating, confinement, and some transport coefficients depend on the magnetic field strength B or current density j. For a spheromak, j is related to B from $\nabla \times \mathbf{B} = \lambda \mathbf{B}$, giving $\mathbf{j} = \lambda \mathbf{B}$. In practical units this gives $j(\frac{MA}{m^2}) = 35.7\frac{B(kG)}{R_s(cm)}$ for a spherical spheromak. While small profile deviations $\mathbf{j} \times \mathbf{B} \neq 0$ have been observed [77,78], the above relation is an excellent approximation for a 0-D model. Thus one only requires an evolution equation for j (or B). On MS, the large I_z discharge provides the formation j. Once the spheromak forms and the I_z current diminishes, the global current density (and field) will decay resistively. Faraday's Law gives

$$\frac{dW_B}{dt} \equiv \partial_t \int \frac{B^2}{8\pi} dV = -\int \mathbf{j} \cdot \mathbf{E}\, dV - \frac{c}{4\pi} \int \mathbf{E} \times \mathbf{B} \cdot d\mathbf{s} \quad .$$

Volume averaging over a region bounded by a conductor makes the surface term zero, and use of $\mathbf{j} = \lambda \mathbf{B}$ and $\mathbf{E} = \eta \mathbf{j} + \frac{\mathbf{v}}{c} \times \mathbf{B}$ gives (using volume averaged quantities implicitly)

$$\frac{dj}{dt} = -\frac{j}{\tau_B} \tag{4.31}$$

where $\tau_B = (4\pi\eta^* \lambda^2)^{-1}$, and η^* was defined in Section 4.2.2.1. If a Spitzer-type effective resistivity is used, it has been shown to be strongly weighted by the cooler edge temperature [18].

The model equations used for j are divided into the formation phase and decay phase. For $t \leq \tau_j^{1/4}$ one assumes the current density j is driven by the capacitor bank I_z circuit as a 1/4 sine wave. For $t \geq \tau_j^{1/4}$, j is allowed to decay resistively with a resistivity determined by the plasma conditions. The overall maximum j is determined by matching j to the value expected from MS magnetic data. For a maximum on-axis midplane B_z field $B_{z=0}^{max}$, the ideal spheromak field profile gives a maximum volume average j of $j_{max} = 0.37\lambda B_{z=0}^{max}$. Thus,

$$\frac{dj}{dt} = \begin{cases} \frac{\pi j_{max}}{2\tau_j^{1/4}} \cos(\frac{\pi t}{2\tau_j^{1/4}}) & , t < \tau_j^{1/4} \\ -\frac{j}{\tau_B} & , t > \tau_j^{1/4} \end{cases} \quad . \tag{4.32}$$

4.3 Numerical Implementation

The set of Equations (4.10)-(4.32) for n_H, n_o, $T_{e,i}$, $\{n_q^Z\}$, j are a coupled non-linear first order system of ODE's. There is a wide range of timescales in the physics processes simulated, and the code time integration step size is limited by the fastest physically significant timescale. A variable timestep, fourth order, Runge-Kutta algorithm adapted from Press et al. [79] is used to advance the system $\{T_e, T_i, j\}$, with separate implicit methods [80,81] for advancing the hydrogen and impurity populations. Refer to the Appendix for code details and a listing.

Initial conditions are based on a cold ($T_o \approx 1$ eV) plasma whose overall hydrogen content is adjusted to give densities agreeing with MS interferometer data. The user specifies the amount of impurity as a percentage of the total hydrogen density, and chooses parameters such as the confinements times, refueling rates, and anomalous resistivity factor. Sensitivity checks to various physics terms were done by varying multiplier 'knobs' on rates to see the effect on the results. Generally, run results were insensitive to factor 2 changes in any particular rate coefficient, but a factor 5 change did produce a noticeable effect.

The O-D code was tested for validity by comparing its predictions with those of previous models in conditions where known physics processes dominate. Olson's previous results [82] treated ohmic heating input and coronal equilibrium radiated power loss as dominating the power balance. For a 1 m radius, 5 T field spheromak with 1.5% oxygen at a density of 6×10^{14} cm^{-3}, his model predicts a limiting temperature of about 20 eV. The 0-D code developed here was run using these conditions, turning off all loss terms except radiated power loss; this gave a limiting temperature of about 23 eV, in reasonable agreement with Olson's model. Note that in this test case one does not expect coronal non-equilibrium effects to be significant because all the transport terms were turned off, and the limiting temperature was obtained on a longer timescale (about 0.4 ms) than typical MS evolution times.

Another means to test the 0-D model is to compare its calculated radiated power losses with those of a more detailed, established model. Post et al. [59] have constructed a coronal equilibrium radiated power model, giving cooling rates L (in $\mathrm{erg\,cm^{-3}\,s^{-1}}$) as a function of temperature for a wide range of impurities. For a typical case of 10 eV average temperature, 6×10^{14} cm^{-3} density, and $f = 1.5\%$ oxygen impurity, the 0-D code indicates about 210 MW/m^3 radiated power (see Figure 5.4). The Post et al. model gives a cooling rate of $L = 4 \times 10^{-19}\ \mathrm{erg\,cm^{-3}\,s^{-1}}$ for oxygen at 10 eV, yielding a radiated power density $P_{rad} = n_{imp}n_eL = fn^2L = 216$ MW/m^3. It is valid to compare equilibrium and non-equilibrum coronal models in this case because, as shown by Carolan and Piotrowicz [20], the coronal equilibrium timescale is much shorter at 10 eV ($\sim 50\ \mu$s at 6×10^{14} cm^{-3} electron density) than it is at the oxygen radiation barrier ($\sim$2 ms at 6×10^{14} cm^{-3}, 25 eV). It is precisely at the radiation barrier conditions that careful consideration of a coronal non-equilibrium model is important. The most difficult, most important, and potentially most inaccurate, calculation of the 0-D code is the radiated power loss. As shown above, the code calculation agrees well with established models.

Chapter 5

Results of Modeling MS Observations

5.1 Selection of Parameters

The first aim of using the 0-D code was to model the MS diagnostics' indications of the plasma's properties. This process involves fitting the model's adjustable parameters to give agreement with MS data. Note that throughout this chapter the term 'hydrogen' refers to the plasma majority ion species; deuterium may be easily substituted.

To fit the average density, one uses the results of the interferometer chord across the spheromak main diameter. The decaying density bursts observed under a wide range of conditions are used to estimate a hydrogen particle confinement time τ_p, as explained in Section 2.2.1.2. The late-time, plateau density n_∞ is used to obtain the average hydrogen refueling rate S_H in steady state, $S_H = \frac{n_\infty}{\tau_p}$. Note that use of this constant influx rate is really only valid for modeling non-bursting density shots. Lowest density, non-bursting MS shots of condition 4503 yield $n_\infty \sim 5 \times 10^{14}$ cm^{-3}, $\tau_p \sim 80$ μs, $S_H \sim 8 \times 10^{18}$ cm^{-3}s^{-1}. The impurity loss time τ_{imp} was set equal to τ_p, and the impurity fueling rate S_{imp} was set to the fraction of impurity times the hydrogen fueling rate S_H.

The magnetic field strength was fitted to the observed magnetic probe measurements. A spheromak-type field was assumed throughout the entire formation and decay with field strength related to current density as explained in Section 4.2.4. Peak on-axis poloidal

Chapter 5

Results of Modeling MS Observations

5.1 Selection of Parameters

The first aim of using the 0-D code was to model the MS diagnostics' indications of the plasma's properties. This process involves fitting the model's adjustable parameters to give agreement with MS data. Note that throughout this chapter the term 'hydrogen' refers to the plasma majority ion species; deuterium may be easily substituted.

To fit the average density, one uses the results of the interferometer chord across the spheromak main diameter. The decaying density bursts observed under a wide range of conditions are used to estimate a hydrogen particle confinement time τ_p, as explained in Section 2.2.1.2. The late-time, plateau density n_∞ is used to obtain the average hydrogen refueling rate S_H in steady state, $S_H = \frac{n_\infty}{\tau_p}$. Note that use of this constant influx rate is really only valid for modeling non-bursting density shots. Lowest density, non-bursting MS shots of condition 4503 yield $n_\infty \sim 5 \times 10^{14}$ cm^{-3}, $\tau_p \sim 80$ μs, $S_H \sim 8 \times 10^{18}$ cm^{-3}s^{-1}. The impurity loss time τ_{imp} was set equal to τ_p, and the impurity fueling rate S_{imp} was set to the fraction of impurity times the hydrogen fueling rate S_H.

The magnetic field strength was fitted to the observed magnetic probe measurements. A spheromak-type field was assumed throughout the entire formation and decay with field strength related to current density as explained in Section 4.2.4. Peak on-axis poloidal

Density	6×10^{14}	cm^{-3}
Peak average temperatures ($T_{e,i}$)	11	eV
Peak on-axis field B_z	4	kG
Magnetic field decay time	110	μs
Fraction oxygen impurity	1.5	%
Particle confinement time	80	μs
Particle refueling rate	8×10^{18}	$\mathrm{cm}^{-3}\mathrm{s}^{-1}$
Anomaly factor κ_{sp}	3	
Peak current density	2.7	$\mathrm{MA/m}^2$

Table 5.1: Properties of the spheromak of MS condition 4503, based on the model fit.

5.2 Results And Discussion

A fit of the model to the best MS conditions of case 4503 yielded the time histories shown in Figures 5.1–5.3. A summary of the model fitted plasma properties are listed in Table 5.1. The starting conditions were a 1 eV, 10% ionized plasma. The overall results were insensitive to the details of the initial plasma conditions, and the code was not expected to in any way accurately model the transient breakdown phase.

5.2.1 Density

Figure 5.1 compares the central chord (diameter) interferometer line-average density to the code's calculated average density. With a fixed particle loss rate of ~ 100 μs, as determined from the formed spheromak density-burst decay, the ionization of neutral hydrogen occurred in about 50 μs independent of moderate variations of other parameters.

5.2.2 Field Strength

Figure 5.2 shows the fitted current density, converted to peak B_z field by assuming the classical spheromak relation $\bar{j}\,(\mathrm{MA/m}^2) = 23.6\frac{B_z^{max}(\mathrm{kG})}{R_s(\mathrm{cm})}$. Also shown is the peak $B_z^{max} = B_z(r = 0, z = 0)$ magnetic data for condition 4503. Note that during the formation this field is due primarily to the externally-imposed reversal discharge current, while during spheromak decay this field is mostly due to plasma currents. Varying the anomalous decay factor κ_{sp} by more than ±0.5 from $\kappa_{sp} = 3.0$ gave substantial disagreement of the

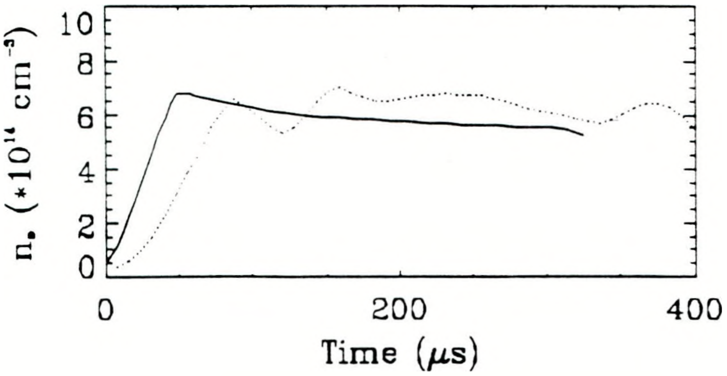

Figure 5.1: Comparison of line-averaged density (dotted) and model volume average density fit (solid) for MS condition 4503.

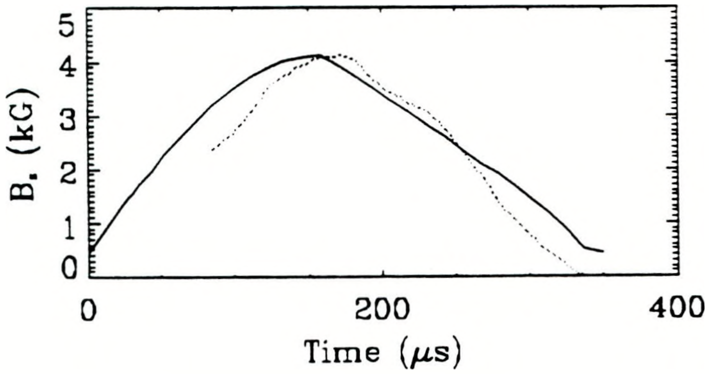

Figure 5.2: Comparison of MS peak B_z field (dotted) and model-derived peak B_z field fit (solid) for MS condition 4503.

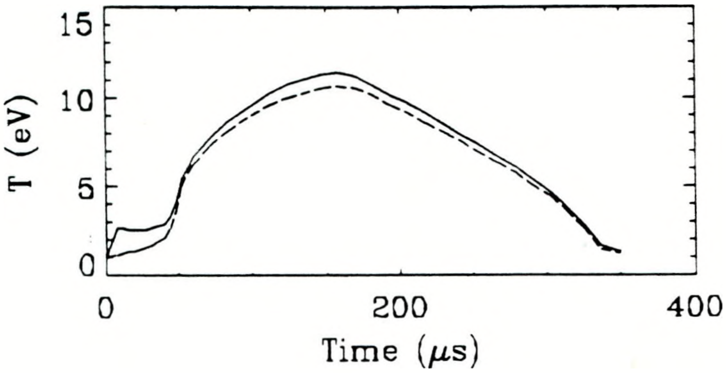

Figure 5.3: Electron (solid) and ion (dashed) temperatures for fit to MS condition 4503.

computed decay rate with the observed MS rate.

5.2.3 Temperatures

Figure 5.3 shows the electron and ion average temperatures. Note the initial delay of temperature increase during ionization: ohmic input power is consumed by the ionization process rather than going into heating. Once ionized, the plasma temperatures climb in 100 μs to about 10-12 eV at maximum plasma current. The system then decays self-consistently, with the temperature-dependent ohmic input power slightly less than the sum of all the loss powers (radiation, charge exchange, thermal conduction, particle refueling), giving a slow decrease of temperature with time. It should be noted that many of the rate coefficients for various atomic processes were only tabulated down to temperatures of 3–5 eV; extrapolation was used to obtain the necessary coefficients at as low as 1 eV temperatures.

The maximum temperature attained depended most strongly on the amount of impurity present, while the field decay rate depended on both the percentage of impurity and the resistivity anomaly factor κ_{sp}. The extent that these two parameters' effects decoupled permitted one to quickly scan the parameter space when fitting the model to MS data. Adjusting the percentage of impurity gave a fractional content of $1.5 \pm .5\%$ oxygen. Deviation of $\pm 0.5\%$ from this value not only varied the field decay rate significantly (which could have been compensated for by adjusting κ_{sp}), but more importantly it changed the electron temperature enough to eliminate or add an oxygen impurity charge state, giving rise to disagreement with MS spectroscopic observations.

5.2.4 Power Balance

The power balance breakdown at the time of peak temperature is shown in Figure 5.4. Note that this assumes that all of the field decay power heats the electrons. The 100 times enhanced electron thermal conduction loss is still insignificant compared to the other losses for relatively cold, highly refueled MS plasmas. Adding up the finite confinement effects of

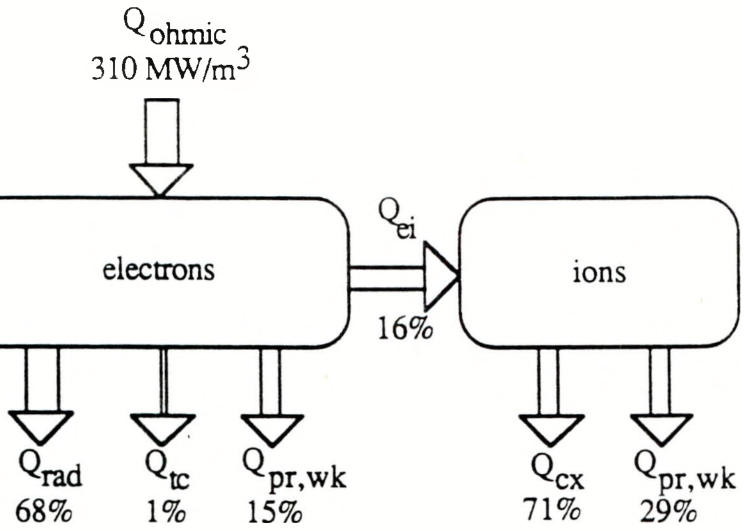

Figure 5.4: Power balance breakdown for model fit to MS case 4503.

charge exchange, electron and ion particle replacement, and electron and ion work done, one finds that 31% of the power loss of modeled condition 4503 is due to finite confinement effects, while 68% is due to radiation.

5.3 Scaling Studies

The modeled MS plasmas appear to be dense, highly radiative, and short-lived. There are three experimentally adjustable methods to increase the spheromak's temperature. First, one may reduce the overall plasma density, at fixed absolute amount of impurity and field strength, so that the average thermal energy per particle $\frac{3}{2}kT$ increases. Second, one may also reduce the percentage of impurity, at fixed density and field strength, to reduce the radiated power loss. Third, one may increase the plasma current density to increase the ohmic heating power ηj^2.

In practice, the plasma density is reduced by reducing the amount of fill gas puffed into the chamber. However, too little gas will not permit breakdown and plasma initiation; in addition, the observations of short particle confinement time and a density higher than the fully ionized fill gas by a factor of 2–5 imply that the formed spheromak density is only weakly controlled by the gas load. The percentage of impurity may be reduced by careful selection of materials that are exposed to the plasma and formation currents, and extensive material conditioning techniques, such as discharge cleaning, baking, and titanium gettering [52,69]. The plasma current density is raised by increasing the formation capacitor banks' energies (reversal, I_z, and bias).

Beginning with the model of present MS conditions, each of these three parameters was varied independent of the others to assess the relative predicted improvement in spheromak temperature. Generally, an increase in temperature gives a much longer plasma lifetime, since the resistivity η varies with temperature $\eta \propto T^{-1.5}$. The results of these scalings are shown in Figures 5.5–5.7. In each case, the parameter value fit to present MS conditions is indicated.

5.3.1 Varying Impurity Fraction

Figure 5.5 shows that even if the percentage of oxygen is reduced by an order of magnitude, the average temperature remains below 20 eV due to short particle confinement time energy losses. These losses are distributed almost evenly among electron refueling, ion refueling, and charge exchange. All of these finite confinement effects scale with the plasma density, so that much lower power loss would be obtained by having both a low plasma density and low impurity fraction.

5.3.2 Varying Field Strength

Figure 5.6 shows the scaling of temperature with volume averaged magnetic field strength. This indicates that a doubling of the present fields (four times the ohmic heating power at a given temperature) would push the volume average temperatures to only about 20 eV. The power balance losses at this high-field condition are about 67% (of the 540 MW/m^3 input power) radiation and 31% finite confinement effects. The difficulty with carrying out this kind of scaling experimentally is that the density observed is strongly coupled to the I_z current as discussed in Chapter 3; raising the plasma currents also gen-

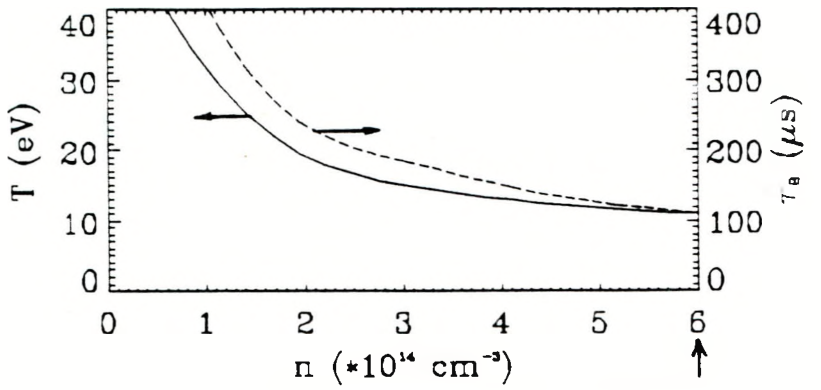

Figure 5.5: Code predictions for scaling amount of oxygen impurity. Vertical arrow indicates model fit for condition 4503.

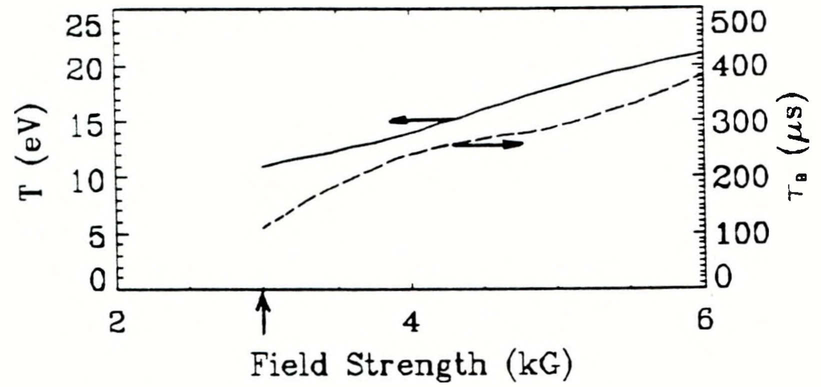

Figure 5.6: Code predictions for scaling magnetic field strength. Vertical arrow indicates model fit for condition 4503.

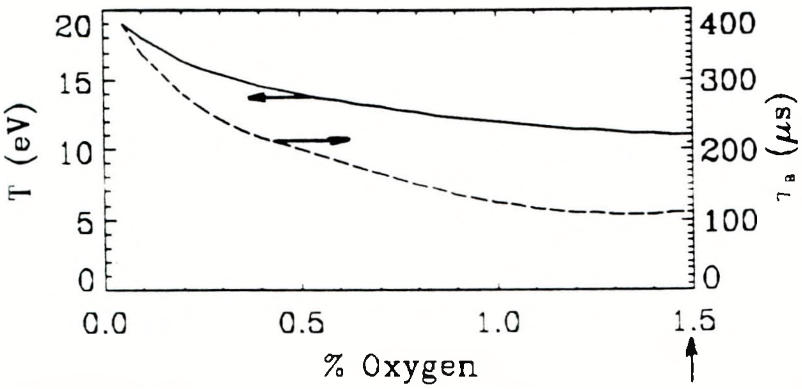

Figure 5.7: Code predictions for scaling hydrogen density (refueling rate is also scaled with density). Vertical arrow indicates model fit for condition 4503.

erally raises the density. This indicates that the present MS density and impurity fraction are high enough to make the oxygen radiation barrier at T_e ~25 eV insurmountable within the MS capacitor bank limitations.

5.3.3 Varying Density

Figure 5.7 shows the temperature scaling with density, keeping the absolute amount of impurity (not the percentage) fixed at the present level of modeled condition 4503. The neutral hydrogen influx rate was required to scale with the density since the particle confinement time was short enough that the formed spheromak density depended much more strongly on the influx rate than on the initial density. Substantial improvement in the average temperature is indicated only when the density is reduced below $\sim 1.5 \times 10^{14}$ cm^{-3} (corresponding to a 6% oxygen impurity content). The power balance in this case remains qualitatively similar to that of present model-fitted MS plasmas, except that the fraction of power lost through finite confinement effects reduces to ~ 25% at a density of 1×10^{14} cm^{-3}, while radiation accounts for most of the remaining 75%. It should be noted that all previous spheromaks reporting volume-average temperatures at or above the oxygen radiation barrier temperature $T_e \sim$ 20-25 eV have operated with densities below 1×10^{14} cm^{-3} [69,67,13].

5.3.4 Combined Effects

The above scalings showed temperature variation with any one of the three main parameters of density, impurity fraction, or field. A more realizable experimental approach would be to aim for more modest improvements of two or more of these parameters simultaneously. One may take the model fit to present MS plasmas (condition 4503) and see what is the effect of reducing the density by one-half and the absolute amount of oxygen impurity by one-third, while raising the volume average field from 3 kG to 5 kG. Table 5.2 lists the resulting plasma parameters from the model, while Figure 5.8 shows the power balance breakdown.

Density	3×10^{14}	cm^{-3}
Peak average temperatures (T_e, T_i)	38.23	eV
Peak average field	5	kG
Magnetic field decay time	≈ 1	ms
Fraction oxygen impurity	1	%
Particle confinement time	80	μs
Particle refueling rate	4×10^{18}	$\mathrm{cm}^{-3}\mathrm{s}^{-1}$
Anomaly factor κ_{sp}	3	
Peak current density	4.5	$\mathrm{MA/m}^2$

Table 5.2: Projected properties of the spheromak of MS condition 4503 with the improved parameters listed in the text.

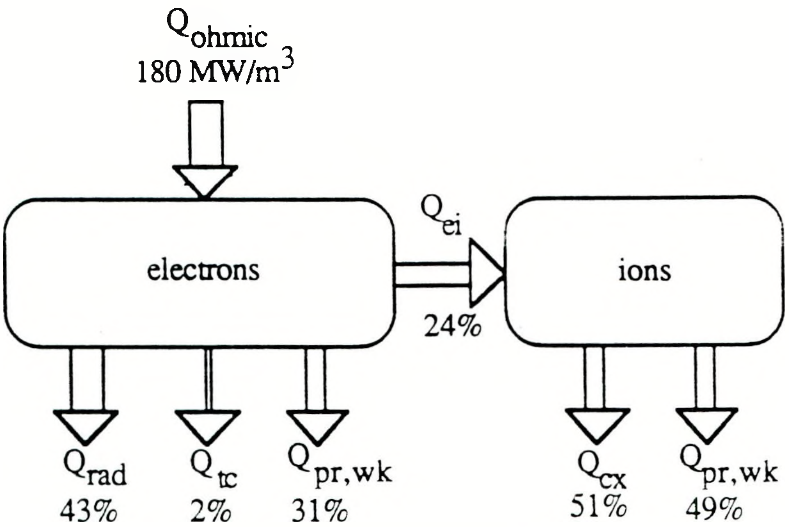

Figure 5.8: Projected power balance breakdown of the spheromak of MS condition 4503 with the improved parameters listed in the text.

Note that the electron temperature has exceeded that of the oxygen radiation barrier ($\sim$ 25 eV) and the ion temperature is decoupled from that of the electrons. The effect of an electron temperature significantly above the radiation barrier is shown by the reduced role of radiation in the power balance, and by the increased decay time ($\sim$1ms) of the plasma field and temperature. When the plasma has burned through most of the highly radiative impurity charge states, a small decrease in temperature does not cause substantial repopulation of these radiative states; thus the plasma cooling increase with decreasing temperature is not enough to overwhelm the ohmic heating power increase with decreasing temperature, as is the case below the radiation barrier. In this kind of plasma, where the impurity radiation barrier has been surpassed, O VI line emission should be readily seen from outer regions of the plasma. The central plasma region would contain O VII.

5.4 Anomalous Ion Heating Modeling

5.4.1 MS Observations

The above modeling assumed that all of the input power from the anomalously high field decay rate went into ohmic heating of the electrons. This imposed the requirement that $T_i \leq T_e$. However, Doppler broadening measurements on MS oxygen and carbon impurity lines indicate a wide range of ion temperatures, with $T_i \geq T_e$ generally.

Figure 1.6 shows intensities and Doppler broadening derived temperatures for C III, C IV, and O IV for MS condition 4503. Several interesting observations may be made. First, multiply-ionized states appear within 50 μs of plasma initiation, indicating that impurity ions in the view of the spectrometer are being ionized faster than the 0-D model predicts. Second, the lines intensities and temperatures peak with the I_z discharge current, indicating that rapid ionization and heating is strongly driven by the I_z. Third, the indicated ion temperatures vary dramatically with the impurity ion: $T_{CIII} \leq 20$ eV, $T_{CIV} \leq 55$ eV, and $T_{OIV} \leq 150$ eV. Some type of anomalous ion heating is present, but its variation with ion mass, charge, and location in the plasma is not readily apparent.

Anomalous ion temperatures have also been reported on the CTX [18] and [illegible]-1 [38] spheromaks, as well as in Reversed Field Pinches [83]. Generally, the ion species appearing at the highest electron temperatures show the largest Doppler broadened line widths. Instrument width was kept small compared to the observed widths, and both instrument effects and Stark effects were subtracted in quadrature from the observed line widths.

5.4.2 Ion Energy Transfer Mechanisms

One may estimate the energy equilibration time scales if electron, hydrogen, and the impurity ions have different temperatures. In the simplest 0-D model, the impurity ions would all be assigned a volume averaged temperature T_{imp}; this would be an average over the various species' ion temperatures as derived from Doppler-broadened line widths. These impurity ions collisionally exchange energy with the electrons (temperature T_e) and hydrogen ions (temperature T_h). The general form of the energy equilibration rate of a charged particle species α with another species β is [55]

$$\frac{3}{2} n_\alpha \frac{dT_\alpha}{dt} = \frac{3}{2} n_\alpha \sum_\beta \nu^\epsilon_{\alpha\beta} (T_\beta - T_\alpha)$$

where

$$\nu^\epsilon_{\alpha\beta} = 1.8 \times 10^{-19} \frac{(m_\alpha m\beta) Z_\alpha^2 Z_\beta^2 n_\beta \lambda_{\alpha\beta}}{(m_\alpha T_\beta + m_\beta T_\alpha)^{3/2}} \qquad \text{sec}^{-1}$$

and $m_{\alpha,\beta}$ are the species' masses in grams, $Z_{\alpha,\beta}$ are the charges in units of the electron charge, n_β is the density of the β species in cm^{-3}, $T_{\alpha,\beta}$ are the temperatures in eV, and $\lambda_{\alpha\beta}$ is the appropriate Coulomb logarithm [55] (typically λ is in the range 8-11).

The inverse of the equilibration rate, $(\nu^\epsilon_{\alpha\beta})^{-1}$, is an estimate of the time scale for the temperature of species α to equilibrate with the fixed temperature of species β, in the absence of any other significant input powers or losses. Table 5.3 shows these times for conditions of $\approx$ 1% oxygen impurity with average ion charge 3, an electron density of $6 \times 10^{14} cm^{-3}$, and temperatures $T_e \approx 12$ eV, $T_i \approx 15$ eV, $T_{imp} \approx 50$ eV. The values of Table 5.3 show that, neglecting all other energy balance terms, initially hot impurity

	e^-	Hydrogen	Impurity
e^-	0.003	2.4	420
Hydrogen	2.4	0.6	18
Impurity	4.2	0.18	6.6

Table 5.3: Energy equilibration times in μs for electrons, hydrogen ions, and oxygen impurity ions assuming collisional energy transfer. Species α is read down at left, species β is across.

ions will collisionally cool down to the electron and hydrogen temperatures within about 10 μs. In reality, there are numerous other energy balance terms present that affect these temperatures. The above equilibration values indicate that unless there is a large power input preferentially heating the impurity ions, their observed high temperature should rapidly fall to that of the electrons and hydrogen ions. The hot impurities do slowly heat the hydrogen ions, as indicated in Table 5.3, and any heating mechanism that strongly couples to the heavy impurity ions will, to a lesser degree, also heat the hydrogen ions.

If one assumes that electrons are ohmically heated by a classical Spitzer resistivity, times a Z_{eff} to account for the impurity fraction, then the input heating power observed from the rate of decay of MS magnetic field Q_{input} may be divided into electron input power $Q^e_{ohmic} = Z_{eff}\eta_{sp}j^2$ and anomalous ion input power

$$Q_{anom} \equiv Q_{input} - Q^e_{ohmic} = (\kappa_{sp} - 1)Q^e_{ohmic} \qquad (5.1)$$

At present there is no satisfactory explanation of the physical mechanism for transferring magnetic energy to the ions. Some conjecture has been made [18] that the ongoing relaxation of magnetic field to get into, and maintain, the minimum energy state causes the plasma to be moved about with the changing flux surfaces. If all plasma components in some local region are given the same turbulent velocities during relaxation, then the temperatures of the various components would be proportioned to their masses if they each separately thermalize. Thus ions, particularly impurity ions, could acquire a much higher temperature than electrons. This process would be complicated by spatial variation of plasma temperature and relaxation activity, as well as by the fact that different species of impurity ions equilibrate with each other almost as rapidly as with themselves, and also equilibrate with the majority hydrogen ions much quicker than with the electrons.

The earlier results with the 0-D model, and other's models [14,61], indicate that the magnetic decay input power is about a factor of 3 times the classical electron heating power. The model here would imply that about 2/3 of the total input power goes into ions. This ion input power is then divided into hydrogen ion input power and impurity ion input power, $Q_{anom} = Q^{h}_{anom} + Q^{imp}_{anom}$. For impurity ion species α with a mass-to-proton-mass ratio μ_α and fractional amount f_α the impurity ion input power is estimated as $Q^{imp}_{anom} = (\sum \mu_\alpha f_\alpha) Q_{anom}$, with the remainder going to the hydrogen ions $Q^{h}_{anom} = (1 - \sum \mu_\alpha f_\alpha) Q_{anom}$. Note that even though the fraction of impurity f may be small ($<5\%$), the mass ratio μ for oxygen is 16 and the input power Q^{imp}_{anom} heats a much smaller number of particles than does Q^{h}_{anom}. This strong effect of anomalous power input on the impurity ion temperature plus the strong collisional energy transfer between impurity and hydrogen ions makes the impurity power balance difficult to model numerically, even in a 0-D code.

5.4.3 Model for Ion Heating

The code was modified to attempt to model anomalous ion heating by including a separate impurity temperature equation in the system (4.10)–(4.32),

$$\frac{3}{2} n_{imp} \frac{dT_{imp}}{dt} = Q^{imp}_{anom} - Q_{imp/h} - Q_{imp/e} - Q^{imp}_{tc} - Q^{imp}_{pr} - Q^{imp}_{wk} - Q^{imp}_{cx}$$

Equations (4.14) for the electrons and hydrogen were modified in two ways. First, collisional energy transfer between impurities and electrons ($Q_{imp/e}$), and impurities and hydrogen ions ($Q_{imp/h}$) was included. Second, the magnetic decay energy was divided into the electron heating part and the anomalous ion heating part according to Equation (5.1). In the parameter regime of MS the thermal conduction (Q^{imp}_{tc}) and fueling losses ($Q^{imp}_{pr}, Q^{imp}_{wk}$) were very small. Using the same value of $\kappa_{sp} = 3.0$ as with the original

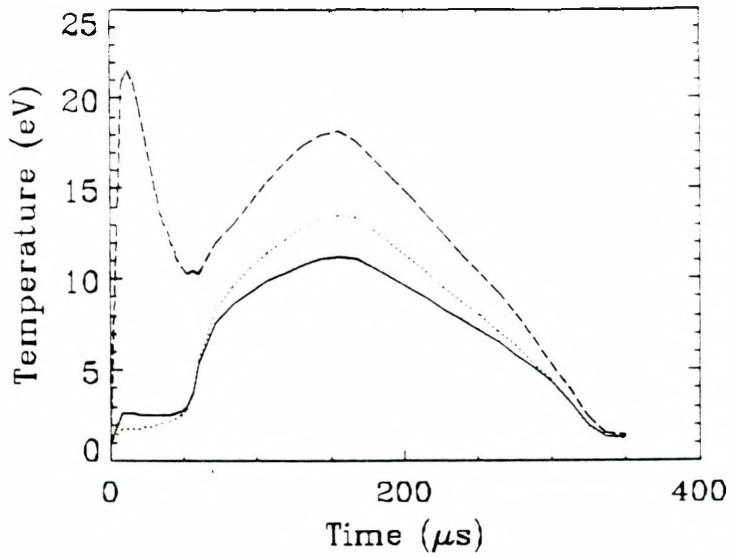

Figure 5.9: Electron (solid), ion (dotted), and impurity ion (dashed) temperatures for fit to MS condition 4503.

model, to obtain a similar overall magnetic field decay rate, this modified model was run for the case of Table 5.1 (MS condition 4503).

Results for the temperatures are shown in Figure 5.9, and are qualitatively very similar to those of the original model. The power balance is virtually the same as that shown in Figure 5.4. The main difference is the effect of the high temperature oxygen impurity. Initially the impurity temperature becomes quite large because of the small amount of hydrogen ions present to exchange energy with the impurities. While hydrogen ionizes the impurity temperature falls, until $t \approx 55$ μs when the fully-ionized hydrogen begins heating. The increasing hydrogen temperature lowers the impurity-hydrogen ion collisional exchange rate, and the impurity ions' temperature again rises under the effect of the steadily increasing heating Q^{imp}_{anom}. All three temperatures rise until the plasma current begins falling at the start of the decay phase, $t \approx 160$ μs. The hydrogen ion temperature is pulled modestly above that of the electrons by the impurity energy transfer.

Evidence for an elevated majority ion species temperature is difficult to obtain spectroscopically, because hydrogen is stripped of its electron at temperatures of about 2 eV [27]. One may instead use helium for the fill gas, since this ion is not expected to be stripped for electron temperatures below about 8 eV, and thus is likely to be emitting its line radiation from somewhere within the spheromak rather than on the cold outer edge. Doppler broadening of He II (4686Å) indicated a majority species ion temperature of 15–17 eV. Since this He II emission is probably not coming from the locally 15–20 eV central magnetic axis region, the volume average T_h is somewhat higher than the 7–8 eV volume average inferred from the He II data. The code indicates a maximum volume average T_h of ≈13 eV, and a T_e that yields impurity ionization states consistent with those seen on MS after spheromak formation.

With the limited parameter range of MS operation, it is impossible to use scaling fits to determine whether the original model or the anomalous ion heating version better fit observation. One may, however, ask if anomalous ion heating has any significant effect on the scaling or power balance predictions of Figures 5.5–5.7. The hypothetical improved case of Table 5.2 was rerun with the anomalous ion heating present. The hydrogen ion and electron temperature histories looked very similar to those produced by the original model, but with the roles of T_e and T_h reversed so that T_h reached 44 eV and T_e reached 30 eV. The impurity temperature T_{imp} reached 72 eV. The power balance (Figure 5.10) changed compared to that of the original model, Figure 5.8, mainly in that the charge exchange and fueling power losses of the ions almost doubled due to the high ion temperatures.

5.5 Conclusions

The 0-D code model provides a means to assess the impact of impurities and a short confinement time on the overall heating and decay of MS plasmas. The model fit to MS data indicates that impurity radiation is presently the most significant loss mechanism. The short particle confinement time and large particle influx rate required to match the interferometer density observations imply that with moderate improvements in density, impurity content, and plasma current the particle confinement effects will become equal to or greater than the radiated power. The anomalous ion temperatures observed spec-

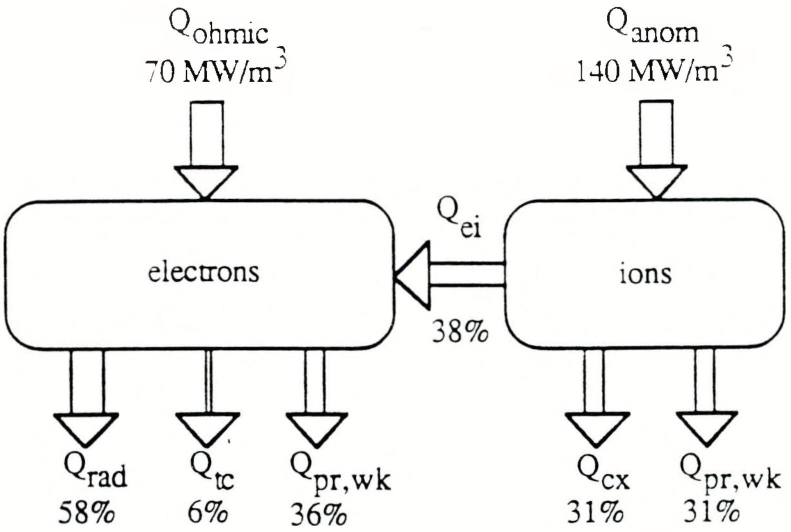

Figure 5.10: Power balance breakdown for model fit to hypothetical improved MS condition. with anomalous ion heating.

troscopically on MS have been included in the model in a self-consistent fashion. but the details of how the field decay power input to the ions is distributed to the impurities and majority hydrogen is not yet known. The model yields volume average impurity temperatures about 1.6 times the average electron temperatures. while observations indicate that this ratio is at least 5.

Chapter 6

Conclusions

The aim of this study was to understand the role of density in spheromak evolution. For MS spheromak plasmas, the temperature and lifetime are well below the design parameters while the density is higher than expected. In general, it is important to assess the impact of fueling, particle confinement time, and impurity content on the spheromak temperature and the configuration decay time.

The interferometer and Langmuir probe diagnostics results show that MS spheromaks form with densities a factor of 2–5 above that expected from the fully ionized fill gas. The rapid density decay after formation indicates particle confinement times less than 100 μs. The short particle confinement time and high density mean that in addition to enhanced radiative power loss, particle refueling losses can become significant. Estimates for the volume average diffusion coefficient were consistent with predictions of turbulent collisional drift waves, at values of about $10D_{\perp}^{Bohm}$. The magnitude of the densities observed depended most strongly on the materials inside the vessel, the wall conditions, and the magnitude of the I_z formation current. The density scaled with the gas puff only when gas loads well above the minimum 3 mT required for consistent breakdown were used.

Spheromak power and particle balance were successfully modeled over the limited range of MS plasmas. The model fit indicates the spheromaks produced are dominated (2/3 of the total power loss) by radiation due to low Z impurities. Spitzer resistivity enhanced by a factor 3 was required to match the observed field decay; the physical processes underlying this anomalous resistivity remain unexplained, but may be associated in part with convection of magnetic energy from within the separatrix, and with temperature profile effects. High ion temperatures observed on spheromaks have been included in the model, by postulating that the ions are heated by the input power fraction not used for classical electron heating. The distribution of ion heating power between the impurity and the majority species ions is not well understood at present, but charge exchange becomes a significant ion power loss channel at high densities and high ion temperatures. In general, the model is unique in its inclusion of direct ion heating and a wide range of physical processes affecting the spheromak evolution.

The observations under present conditions and the model's projections permit some recommendations for ways to improve MS spheromak properties. The scaling runs indicate that combined improvements of higher input currents (peak field), lower impurity fraction, and lower density are required for 50 eV, 2 ms regime spheromaks. The density and spectroscopy observations show that primary sources of enhanced density are the I_z electrode insulators and the vessel walls, while the reversal coil coverings contribute to a lesser degree. Since higher I_z current (and hence higher spheromak heating) also increases the density, a better route to hotter spheromaks in MS is to lower the fueling, by achieving breakdown at lower gas fills (with an effective preionizing scheme) in conjunction with conditioning the vessel walls. The use of wall gettering [69] on the plasma-exposed surfaces could make the short particle confinement time an advantage, since the highly absorptive coated wall surfaces would effectively pump the plasma's blanket refueling gas and rapidly reduce the spheromak density [68]. Both low gas fill breakdown and gettering would have to be used simultaneously to avoid saturating the getter coating.

Appendix: 0-D Computer Code

The following pages are a listing of the various parts of the 0-D computer code. The code is written in Vax Pascal, and is segmented into several files. The rate coefficient data for various atomic processes are contained in separate data files; these are not included here for sake of brevity, but may be obtained from the author in printed or computer format. References for the rate coefficients are described in the main text and are also included as comments in the source code.

The code is generally written for clarity rather than speed, since a typical interactive run takes only about 20 seconds of real time on a VaxStation 3100. Note that when modeling anomalous ion heating, the small timesteps required greatly increased the run time.

```
{ Program to do 0-dim transport model for spheromak. Program history:  }
{                                                                       }
{ Originally written in Pascal for an Atari 1040ST personal computer    }
{ (5/1/89), ported over to a microVax for use with VaxPascal compiler.  }
{ This initial version (10/10/89) is identified as 0.90.                }
{                                                                       }
{ Version 1.00 (10/17/89) includes adjustable compression effects.      }
{                                                                       }
{ Version 1.50 (11/1/89) changes include:                               }
{   i) replacing B field evolution with j current density               }
{  ii) adjustable 'knobs' for sensitivity testing of rates, radiations,}
{      power losses.                                                    }
{ iii) correction of tau_ohmic=2pi() instead of 4pi().                  }
{  iv) use of implicit method to advance impurities.                    }

PROGRAM o_d_transport(input,output,readfile,writefile);

CONST maximpurities = 2       ;         {keep small as possible - memory!}
      zmaxplus1     = 9       ;         {max Z of impurities used, plus 1}
      nonimpvars    = 5       ;         {# saved vars advanced explicitly}
      maxsavevars   = 36      ;         {# saved quantities}
      maxsave       = 100     ;         {max # saved t steps}
      firststep     = 5.0e-7  ;         {initial t step guess, sec}
      minstep       = 5.0e-9  ;         {minimum t step, sec}
      smallchange   = 0.01    ;         {fractional change for t step}
      t_scale       = 1.0e-6  ;         {microsec to sec}
      j_scale       = 3.0e9   ;         {A/cm^2 to statA/cm^2}
      b_scale       = 1.0e-3  ;         {kGauss to Gauss}
      tempconvert   = 1.6e-12;          {eV to ergs,since all temps in eV}
      densconvert   = 1.0e14  ;         {densities in units of 10^14 cm-3}
      lnmaxreal     = 71.0    ;         {approx max allowed x of exp(x)}
      extrapolatefactor = 0.1;          {nondimensional, used for extrap.}
      h_ionpotent   = 13.6    ;         {in eV}
      pathname      = '[.results]';     {subdirectory with data files}
      inputfileroot = 'SETTINGS';       {file name root for input data}
      fw = 12;    spc = 4;    prc = 6;  {formats: fullwidth, space, prec.}
      strsize       = 15      ;         {string length - keep small}
      eii_maxcoeffs = 9       ;         {for e ionization data}
      cxr_maxcoeffs = 9       ;         {for charge exchange data}
      dr_maxcoeffs  = 4       ;         {for dielectronic recomb data}
      eie_maxcoeffs = 10      ;         {for e excitation data}
      eie_maxtrans  = 2       ;         {for e excitation data}

TYPE  stringer      = VARYING [strsize] OF char;      {VAX/VMS Pascal}
      power         = (q_ohmic, q_thermal_e, q_thermal_i, q_rad, q_ei,
                       q_replace_e, q_replace_i, q_work_e, q_work_i, q_cx,
                       q_aux_e, q_aux_i);
      powerrange    = q_ohmic..q_aux_i;
```

```
      powertype    = ARRAY[powerrange] OF real;
      radiation    = (brem_rad,cxr_rad,dr_rad,rr_rad,line_rad);
      radrange     = brem_rad..line_rad;
      radtype      = ARRAY[radrange] OF real;
      parameter    = (tau_p,tau_imp,radius,templength,h_rate,imp_rate,
                      kappa_sp,kappalow,chiswitch,energy_ih,coldtemp,
                      compress_on,compress_off,peakcompress,tau4_j,
                      peakfield,min_j);
      paramrange   = tau_p..min_j;
      paramtype    = ARRAY[paramrange] OF real;
      impurityarray= ARRAY[1..zmaxplus1] OF real;
      arrayvar     = RECORD
                       values    : impurityarray;
                       ionpotent: impurityarray;  {ionization potentials}
                       k_ionpotent: real;           {knob for potentials}
                       e_excite : impurityarray;  {1st excited state en.}
                       k_e_excite: real;           {knob for excitations}
                       Z         : integer;
                       mass      : real;        {in units of proton mass}
                       fraction : real
                     END;
      impuritytype = ARRAY[1..maximpurities] OF arrayvar;
      datatype     = RECORD
                       e_temp : real;
                       i_temp : real;
                       currentdens : real;
                       h_density : real;
                       h_n_density : real;
                       impurities : impuritytype
                     END;
      evolvetype   =  ARRAY[1..nonimpvars] OF real;
      resulttype   =  ARRAY[1..maxsavevars,1..maxsave] OF real;
      eii_coefftype = ARRAY[1..zmaxplus1,1..eii_maxcoeffs] OF real;
      cxr_coefftype = ARRAY[2..zmaxplus1,1..cxr_maxcoeffs] OF real;
      dr_coefftype  = ARRAY[2..zmaxplus1,1..dr_maxcoeffs] OF real;
      eie_coefftype =
        ARRAY[1..zmaxplus1,1..eie_maxtrans,1..eie_maxcoeffs] OF real;
      coeff      = (eii,cxr,dr,eie,rr);
      coeffrange = eii..rr;
      kcoefftype = ARRAY[coeffrange] OF real;

VAR   variables             : datatype;
      prm                   : paramtype;
      results               : resulttype;
      time                  : ARRAY[1..maxsave] OF real;
      pwr,k_pwr             : powertype;
      k_rad                 : radtype;
      e_density,maglength,kappa,chi_curr              : real;
```

```
      begintime,endtime,dt_save,changesavetime         : real;
      numimpurities,numok,numbad,numsaves              : integer;
      c_eii,o_eii           : eii_coefftype;      {for e ionization data}
      h_cxr,c_cxr,o_cxr     : cxr_coefftype;      {for charge exchange}
      c_dr,o_dr             : dr_coefftype;     {for dielectronic recomb}
      c_eie,o_eie           : eie_coefftype;      {for e excitation}
      k_coeffs              : kcoefftype;         {knobs for all rates}
      masterpath            : stringer;    {keeps track of file path}
      dataversion           : stringer;    {labels result files 0-999}
      quitearly             : boolean;
      readfile,writefile    : text;

{ procedure to get parameters and initial conditions. User must provide
  a file 'SETTINGSXXX.DAT' with proper format for program to read, where
  XXX is the run number. }
PROCEDURE getrunparameters(VAR quitearly:boolean);
CONST headerlines = 8;       {# comment lines at top of data file}
VAR i,q     : integer;
    item    : parameter;
    rate    : coeff;
    energy  : power;
    rad     : radiation;
    n_fraction : real;
    inputfilename : stringer;

  BEGIN
    masterpath := pathname;                {used in writing data to files}
    write('Enter version # of run (000-999):');
    readln(dataversion);
    inputfilename := inputfileroot+dataversion;
    open(readfile,pathname+inputfilename+'.DAT',OLD);
    reset(readfile);
    FOR i:=1 TO headerlines DO
      readln(readfile);
    FOR item:=tau_p TO min_j DO readln(readfile,prm[item]);
    readln(readfile);                               {skip line of comments}
    readln(readfile,begintime);
    prm[tau4_j] := prm[tau4_j]+begintime;           {offset to begintime}
    prm[compress_on]  := prm[compress_on]+begintime;
    prm[compress_off] := prm[compress_off]+begintime;
    readln(readfile,endtime);                      {actually time interval}
    endtime := begintime+endtime;
    readln(readfile,dt_save);
    readln(readfile,changesavetime);
    WITH variables DO
      BEGIN
        readln(readfile,e_temp);                   {in eV}
        readln(readfile,i_temp);
```

```
     currentdens := prm[min_j];                 {to start with}
     readln(readfile,h_density);                {in densconvert units}
     readln(readfile,n_fraction);
     h_n_density := n_fraction*h_density;
     readln(readfile,numimpurities);
     FOR i:=1 TO numimpurities DO
       WITH impurities[i] DO
         BEGIN
           readln(readfile);                   {skip line of comments}
           readln(readfile,Z,mass,fraction);
           readln(readfile);                   {skip line of comments}
           FOR q:=0 TO Z DO
             BEGIN
               read(readfile,values[q+1]);           {normalized to 1}
               values[q+1] := fraction*(h_density+h_n_density) *
                              values[q+1]
             END;  readln(readfile);
           readln(readfile);            {skip line}
           FOR q:=0 TO Z-1 DO read(readfile,ionpotent[q+1]);
           readln(readfile);
           readln(readfile);            {skip line}
           FOR q:=0 TO Z-1 DO read(readfile,e_excite[q+1]);
           readln(readfile)
         END   {for i=1 to numimpurities}
    END;   {with variables do}
  readln(readfile);                                        {skip line}
  FOR energy:=q_ohmic TO q_aux_i DO read(readfile,k_pwr[energy]);
  readln(readfile);
  readln(readfile);                                        {skip line}
  FOR rate:=eii TO rr DO
    read(readfile,k_coeffs[rate]);  readln(readfile);
  readln(readfile);                                        {skip line}
  FOR rad:=brem_rad TO line_rad DO read(readfile,k_rad[rad]);
  readln(readfile);
  close(readfile)
END;
```

```
{ Set of routines called by program o_d_transport. These routines are
  method-specific. The global CONSTants, TYPEs, and VARiables are
  defined in file PROLOGUE.PAS }

{ Function to return value of Chebychev polynomial Tn(x), used as
  fitting polynomials for rate coefficient data. }
FUNCTION chebychev(n:integer; x:real):real;
VAR i : integer;
    last,this,next : real;
BEGIN
  last := x;
  this := 2*sqr(x)-1;
  IF n=1 THEN chebychev:=last
  ELSE IF n=2 THEN chebychev:=this
  ELSE IF n>2 THEN
    BEGIN                 {use recursion: T(n+1,x)=2x*T(n,x)-T(n-1,x)}
      FOR i:=3 TO n DO
        BEGIN
          next := 2*x*this-last;
          last := this;
          this := next
        END;
      chebychev := this
    END
  ELSE
    BEGIN
      writeln(' Fatal error in chebychev - order<0...hit <return>');
      readln;
      chebychev := 1.0    {default error value}
    END
END;   {chebychev}

{Two functions to get compression factor and derivative of compression
 factor. User is responsible for ensuring that t1<=t<=t2!}
FUNCTION compression(t1,t2,t,c0:real):real;
VAR tbar,dt : real;
BEGIN
  tbar := (t1+t2)/2;
  dt := t2-t1;
  compression := c0+8*(1-c0)*sqr((t-tbar)/dt)*(1-2*sqr((t-tbar)/dt))
END;

FUNCTION d_compression(t1,t2,t,c0:real):real;
VAR tbar,dt : real;
BEGIN
  tbar := (t1+t2)/2;
  dt := t2-t1;
  d_compression := 16*(1-c0)*(t-tbar)/sqr(dt)*(1-4*sqr((t-tbar)/dt))
```

```
END;

{ Function to return value of rate coefficient for the process of
  charge-exchange recombination (in cm^3/sec). Reference:
    R.A. Phaneuf, R.K. Janev, M.S. Pindzola, "Collisions of Carbon and
    Oxygen Ions with Electrons, H, H2, and He", Atomic Data for Fusion
    Series, Vol. V, Oak Ridge Nat. Lab., 1987.
    (Hereafter referred to as 'PJP'.)
  Note that the globals cxr_maxcoeffs,cxr_coefftype,h_cxr,c_cxr,
  o_cxr were defined and assigned in main program. }
FUNCTION alpha_cxr(Z,q:integer; T_i:real):real;  {note that q=ion charge}
CONST emin = 8;  emax = 9;                      {indices in cxr_coefftype}
VAR  element : cxr_coefftype;
     i       : integer;
     temp,x,sum,t1,t2,alpha1,alpha2 : real;
BEGIN
  IF (q<1) OR (q>Z) THEN
    temp := 0.0
  ELSE IF Z=1 THEN
    BEGIN
      x := ln(1.25*(T_i+prm[coldtemp]))/ln(10.0);      {log base 10}
      temp := 1.61e-10*sqrt(T_i+prm[coldtemp])*sqr(7.6-1.06*x)
    END
  ELSE
    BEGIN
      CASE Z OF
        6          : element := c_cxr;
        8          : element := o_cxr
        END;
      IF (T_i>=element[q+1,emin]) AND (T_i<=element[q+1,emax]) THEN
        BEGIN            {do normal polynomial evaluation}
          x := ln( sqr(T_i)/(element[q+1,emin]*element[q+1,emax]) )/
               ln( element[q+1,emax]/element[q+1,emin] );
          sum := 0.5*element[q+1,1];
          FOR i:=1 TO cxr_maxcoeffs-3 DO
            sum := sum+element[q+1,i+1]*chebychev(i,x);
          temp := sum
        END
      ELSE         {do linear extrapolation of logarithms of two points}
        BEGIN
          IF T_i<element[q+1,emin] THEN
            BEGIN
              t1 := element[q+1,emin];
              t2 := t1*(1+extrapolatefactor)
            END
          ELSE
            BEGIN
              t2 := element[q+1,emax];
```

```
              t1 := t2*(1-extrapolatefactor)
            END;
          alpha1 := alpha_cxr(Z,q,t1);          {recursive calls}
          alpha2 := alpha_cxr(Z,q,t2);
          IF (alpha1<0.0) OR (alpha2<0.0) THEN temp:=0.0
          ELSE
            BEGIN
              sum := (ln(t2/T_i)*ln(alpha1)-ln(t1/T_i)*ln(alpha2)) /
                     ln(t2/t1);
              IF sum<-lnmaxreal THEN temp:=0.0    {check for underflow!}
              ELSE temp:= exp(sum)
            END
        END    {linear extrapolation}
    END;
  alpha_cxr := temp*k_coeffs[cxr]
END;   {alpha_cxr}

{ Function to return value of rate coefficient for the process of
  electron impact ionization (in cm^3/sec). References:
    1)  R. Elton, in "Methods of Experimental Physics", Vol 9 -
         Plasma Physics. Eds H.R. Griem & R.H. Lovberg, Ch. 4.
    2)  PJP     (see also W. Lotz, Astrophys. J. Suppl. <14>,207 (1967).)
  Note that the globals eii_maxcoeffs,eii_coefftype,c_eii,o_eii
  were defined and assigned in main program. }
FUNCTION alpha_eii(Z,q:integer; T_e:real):real;      {q=ion charge}
CONST emin = 8; emax = 9;
VAR  element          : eii_coefftype;
     i                : integer;
     temp,x,sum,t1,t2,alpha1,alpha2 : real;
BEGIN
  IF q>(Z-1) THEN
    temp := 0.0
  ELSE IF Z=1 THEN                  {use Elton's formula for hydrogen}
    BEGIN
      x := (h_ionpotent/T_e);
      temp := 2.5e-6*exp(-x-1.5*ln(T_e)) / (sqr(x)*(1+1.0/x))
    END
  ELSE
    BEGIN                    {use tables of coeffs for impurities}
      CASE Z OF
        6  :  element := c_eii;
        8  :  element := o_eii
      END;
      IF (T_e>=element[q+1,emin]) AND (T_e<=element[q+1,emax]) THEN
        BEGIN                         {do normal polynomial evaluation}
          x := ln( sqr(T_e)/(element[q+1,emin]*element[q+1,emax]) )/
               ln( element[q+1,emax]/element[q+1,emin] );
          sum := 0.5*element[q+1,1];
```

```
         FOR i:=1 TO eii_maxcoeffs-3 DO
           sum := sum+element[q+1,i+1]*chebychev(i,x);
         temp := sum
       END
     ELSE        {do linear extrapolation of logarithms of two points}
       BEGIN
         IF T_e<element[q+1,emin] THEN
           BEGIN
             t1 := element[q+1,emin];
             t2 := t1*(1+extrapolatefactor)
           END
         ELSE
         BEGIN
           t2 := element[q+1,emax];
           t1 := t2*(1-extrapolatefactor)
         END;
{         writeln(' Mild warning in alpha_eii - e temp beyond range'); }
         alpha1 := alpha_eii(Z,q,t1);          {recursive calls}
         alpha2 := alpha_eii(Z,q,t2);
         IF (alpha1<=0.0) OR (alpha2<=0.0) THEN temp:=0.0
         ELSE
           BEGIN
             sum := (ln(t2/T_e)*ln(alpha1)-ln(t1/T_e)*ln(alpha2)) /
                    ln(t2/t1);
             IF sum<-lnmaxreal THEN temp:=0.0    {check for underflow!}
             ELSE temp:=exp(sum)
           END
       END    {linear extrapolation}
    END;   {if q>(Z-1)...else...}
  alpha_eii := temp*k_coeffs[eii]
END;   {alpha_eii}

{ Function to return value of rate coefficient for the process of
  radiative recombination (in cm^3/sec). Reference: D.E. Post, et. al.,
  Atomic Data and Nuclear Data Tables <20>,397 (1977). }
FUNCTION alpha_rr(Zee,q:integer; T_e:real):real;          {q=ion charge}
VAR i : integer;
    temp,x : real;
BEGIN
  IF (q<1) OR (q>Zee) THEN
    temp := 0.0
  ELSE
    BEGIN
      IF Zee=1 THEN x:=h_ionpotent/T_e
      ELSE  {find impurity's ionization potential}
        FOR i:=1 TO numimpurities DO
          IF variables.impurities[i].Z=Zee THEN
            x := variables.impurities[i].ionpotent[q];
```

```
      temp := 5.20e-14*q*exp(1.5*ln(x))*( ln((1+x)/x)-0.4/sqr(1+x) )
    END;
  alpha_rr := temp*k_coeffs[rr]
END;   {alpha_rr}

{ Function to return value of rate coefficient for the process of
  dielectronic recombination (in cm^3/sec). Reference:
    S.M.V. Aldrovandi and D. Pequignot,
    Astron & Astrophys <25>, 137 (1973).
  Note that the globals dr_maxcoeffs,dr_coefftype,c_dr,o_dr
  were defined and assigned in main program.      }
FUNCTION alpha_dr(Z,q:integer; T_e:real):real;        {q=ion charge}
CONST tconvert = 11600.0;       {A&P's values in K - must convert to eV}
VAR element       : dr_coefftype;
    temp,dummy1,dummy2 : real;
BEGIN
  temp := 0.0;
  CASE Z OF
    6   :   element := c_dr;
    8   :   element := o_dr;
    OTHERWISE
      BEGIN
        writeln(' Error in alpha_dr - wrong element...hit <return>');
        readln
      END
  END;
  IF (q>0) AND (q<Z) THEN
    BEGIN
      dummy1 := -element[q+1,3]/(tconvert*T_e)-1.5*ln(tconvert*T_e);
      dummy2 := -element[q+1,4]/(tconvert*T_e);
      IF dummy1<-lnmaxreal THEN temp:=0.0        {check for underflow}
      ELSE
        BEGIN
          IF dummy2<-lnmaxreal THEN dummy2:=0.0      {ditto}
          ELSE dummy2:=exp(dummy2);
          temp:=exp(dummy1)*element[q+1,1]*(1+element[q+1,2]*dummy2)
        END
  END;
  alpha_dr := temp*k_coeffs[dr]
END;   {alpha_dr}

{ Function to return value of line radiation for the process of
  electron impact excitation (in eV*density/time). Reference: PJP }
FUNCTION lineradiation(Zee,q:integer; T_e:real):real;     {q=ion charge}
CONST emin = 8;  emax = 9;                      {indices in eie_coefftype}
VAR  element : eie_coefftype;
     i,j      : integer;
     temp,x,impuritydens,radsum,ratesum : real;
```

```
    t1,t2,alpha1,alpha2,sum        : real;
BEGIN
  IF (q<1) OR (q>=Zee) THEN                   {ignoring neutrals for now}
    temp := 0.0
  ELSE
    BEGIN
      CASE Zee OF
        6         :  element := c_eie;
        8         :  element := o_eie;
        END;
      {get appropriate density}
      FOR i:=1 TO numimpurities DO
        IF variables.impurities[i].Z=Zee THEN
          impuritydens := variables.impurities[i].values[q+1];
      {ratesum will contain excitation rate coefficient, radsum will add
       up energies lost by each transition of requested ion}
      radsum := 0.0;
      FOR j:=1 TO eie_maxtrans DO      {sum over transitions considered}
        BEGIN
          ratesum := 0.0;
          t1 := element[q+1,j,emin]; {note that t1=t2=0.0 if less than..}
          t2 := element[q+1,j,emax]; {..maxtrans transitions are present}
          IF (T_e>=t1) AND (T_e<=t2) THEN
            BEGIN            {do normal polynomial evaluation}
              x := ln(sqr(T_e)/(t1*t2)) / ln(t2/t1);
              ratesum := 0.5*element[q+1,j,1];
              FOR i:=1 TO eie_maxcoeffs-4 DO
                ratesum := ratesum+element[q+1,j,i+1]*chebychev(i,x)
            END
          ELSE IF (t1<>0.0) AND (t2<>0.0) THEN
            {do linear extrapolation of logarithms of two points}
            BEGIN
              IF T_e<t1 THEN t2:=t1*(1+extrapolatefactor)
              ELSE t1:=t2*(1-extrapolatefactor);
              {get first point}
              x := ln(sqr(t1)/(element[q+1,j,emin]*element[q+1,j,emax]))
                   / ln( element[q+1,j,emax]/element[q+1,j,emin] );
              alpha1 := 0.5*element[q+1,j,1];
              FOR i:=1 TO eie_maxcoeffs-4 DO
                alpha1 := alpha1+element[q+1,j,i+1]*chebychev(i,x);
              {get second point}
              x := ln(sqr(t2)/(element[q+1,j,emin]*element[q+1,j,emax]))
                   /ln( element[q+1,j,emax]/element[q+1,j,emin] );
              alpha2 := 0.5*element[q+1,j,1];
              FOR i:=1 TO eie_maxcoeffs-4 DO
                alpha2 := alpha2+element[q+1,j,i+1]*chebychev(i,x);
              {now do extrapolation}
              IF (alpha1<0.0) OR (alpha2<0.0) THEN ratesum:=0.0
```

```
              ELSE
                BEGIN
                  sum := (ln(t2/T_e)*ln(alpha1)-ln(t1/T_e)*ln(alpha2)) /
                          ln(t2/t1);
                  IF sum<-lnmaxreal THEN ratesum:=0.0  {check underflow}
                  ELSE ratesum := exp(sum)
                END
            END;    {linear extrapolation}
          {finally, add contribution to line radiation}
          radsum := radsum+e_density*impuritydens*densconvert *
                    ratesum*element[q+1,j,eie_maxcoeffs]
        END;   {for j:=1 to maxtrans...}
      temp := radsum
    END;   {else...}
  lineradiation := temp*k_coeffs[eie]
END;   {lineradiation}

{ procedure to calculate right-hand-side of integrating equation set }
PROCEDURE derivs(t : real; y : evolvetype; VAR dydt : evolvetype);

CONST pi        = 3.14159;
      jnot      = 4.493;    {first zero of spherical Bessel fcn order 0}
      c         = 3.0e10;       {speed of light, cm/sec}

VAR T_e, T_i, J, h_dens, h_n_dens, impiondensity, z_eff, tau_j, f_z,
    tauohmic, ee_log, ei_log, ii_log, t_c_on, t_c_off, c_peak    : real;
    h_ionrate, k_spheromak, rate, sum0, sum1, sum2, peak_j,
    resistivity, lastionizcoef, thisionizcoef, thisrecombcoef,
    nextrecombcoef                                               : real;
    i, q  : integer;

{ Function to calculate total radiated power of plasma, in
  eV*density/time }
FUNCTION getradiationpwr:real;
VAR i,q  : integer;
    p_brem,p_cxr,p_dr,p_rr,p_line : real;
BEGIN
  p_dr:=0.0;  p_line:=0.0;
{H part}
  p_rr := 1.69e-25*densconvert*e_density*h_dens*h_ionpotent/sqrt(T_e);
  p_cxr := 0.0;
{H part}
{ p_cxr := h_dens*h_n_dens*densconvert*alpha_cxr(1,1,T_i)*h_ionpotent; }
  FOR i:=1 TO numimpurities DO
    WITH variables.impurities[i] DO
      BEGIN
        FOR q:=1 TO Z DO
          BEGIN
```

```
{            p_cxr  := p_cxr + h_n_dens*values[q]*densconvert*        }
{                              alpha_cxr(Z,q,T_i)*ionpotent[q];       }
            p_dr   := p_dr + e_density*values[q]*densconvert*
                        alpha_dr(Z,q,T_e)*(ionpotent[q]+e_excite[q+1]);
            p_rr   := p_rr + 1.69e-25*densconvert*e_density*sqr(q)*
                        values[q]*ionpotent[q]/sqrt(T_e);
            p_line := p_line+lineradiation(Z,q,T_e)  {see fcn 4 details}
          END;
      END;
  p_brem := 1.53e-25*densconvert*sqr(e_density)*z_eff*sqrt(T_e) /
            tempconvert;
  getradiationpwr := p_brem*k_rad[brem_rad] + p_cxr*k_rad[cxr_rad] +
                     p_dr*k_rad[dr_rad] + p_rr*k_rad[rr_rad] +
                     p_line*k_rad[line_rad]
END;  {getradiationpwr}

{ ***** Main part of derivs ***** }
BEGIN
  T_e      := y[1];                  {just makes code easier to read}
  T_i      := y[2];
  J        := y[3];
  h_dens   := y[4];
  h_n_dens := y[5];
  t_c_on   := prm[compress_on];
  t_c_off  := prm[compress_off];
  c_peak   := prm[peakcompress];
  {calculate total impurity density, electron density, and Z effective}
  {note that e_density is a global variable}
  WITH variables DO
    BEGIN
      sum0 := 0.0;   sum1 := 0.0;   sum2 := 0.0;
      FOR i:=1 TO numimpurities DO
        WITH impurities[i] DO
          FOR q:=1 TO Z DO
            BEGIN
              sum0 := sum0+values[q+1];     {sum impurity ion densities}
              sum1 := sum1+values[q+1]*q;    {sum for charge neutrality}
              sum2 := sum2+values[q+1]*sqr(q)      {sum for Z effective}
            END;
      impiondensity := sum0;
      e_density := h_dens+sum1;
      z_eff := (h_dens+sum2)/e_density
    END;   {with variables do...}

  {calculate change of current density J, h density, h-neutral density}
  {get characteristic length scale of magnetic gradients, a global}
  k_spheromak := jnot/prm[radius];            {for spherical sheromak}
  maglength := 1/k_spheromak;
```

```
{adjust scale length for compression, if necessary}
IF (t>t_c_on) AND (t<t_c_off) THEN
  maglength := maglength/compression(t_c_on,t_c_off,t,c_peak);
{electron-electron coulomb log - see Braginskii}
ee_log := 24.0- ln(sqrt(e_density*densconvert)/T_e);
{resistivity scaling factor}
f_z := 0.582+0.418*exp(-0.7*ln(z_eff));
{ohmic dissipation time - use half Spitzer since j parallel to B, and
 Spitzer is a perpendicular resistivity. kappa is a global}
resistivity := 5.75e-15*kappa*z_eff*ee_log*f_z / exp(1.5*ln(T_e));
tauohmic := 2*pi*sqr(maglength/c)/resistivity;     {note factor 2*pi!}
{field dissipation time}
tau_j := 2*tauohmic;
peak_j := c/(4*pi*j_scale)*(prm[peakfield]/b_scale)*k_spheromak -
          prm[min_j];
WITH variables DO
  BEGIN
    {multiple equations use this rate}
    h_ionrate := e_density*h_n_dens*densconvert*alpha_eii(1,0,T_e);
    {rate of change of current density - rises with Iz, then decays}
    IF t<prm[tau4_j] THEN
      dydt[3] := peak_j/(2/pi*prm[tau4_j])*cos(t/(2/pi*prm[tau4_j]))
    ELSE
      dydt[3] := -j/tau_j;
    {rate of change of hydrogen ions}
    dydt[4] := h_ionrate - h_dens/prm[tau_p] -
               e_density*h_dens*densconvert*alpha_rr(1,1,T_e);
    {adjust h ion density for compression, if necessary}
    IF (t>t_c_on) AND (t<t_c_off) THEN
      dydt[4] := dydt[4]+3*h_dens *
                   d_compression(t_c_on,t_c_off,t,c_peak) /
                   compression(t_c_on,t_c_off,t,c_peak);
    {rate of change of neutral hydrogen}
    dydt[5] := prm[h_rate] - h_ionrate
  END;

 {now calculate change of electron, ion temperatures}
 {note that the q_'s are global variables}
 WITH variables DO
   BEGIN
     {first get heating contributions, all in eV*density/time}
     pwr[q_ohmic] := resistivity*sqr(J*j_scale)*k_pwr[q_ohmic] /
                     (densconvert*tempconvert);
     pwr[q_replace_i] := 1.5*(h_ionrate+prm[imp_rate]) *
                             (T_i-prm[coldtemp])*k_pwr[q_replace_i];
     pwr[q_replace_e] := 1.5*(h_ionrate+z_eff*prm[imp_rate]) *
                             (T_e+prm[energy_ih])*k_pwr[q_replace_e];
     IF T_i>prm[coldtemp] THEN
```

```
  pwr[q_cx] := 1.5*h_dens*h_n_dens*densconvert*alpha_cxr(1,1,T_i)*
               (T_i-prm[coldtemp])*k_pwr[q_cx]
ELSE
  pwr[q_cx] := 0.0;
{need some ion species summations for e-ion heat transfer (sum0)
 and ion thermal conduction (sum1)}
{first count hydrogen ion contribution}
ei_log := 23.0-0.5*ln(e_density*densconvert)+1.5*ln(T_e);
sum0 := ei_log;
ii_log := 23.0-ln(z_eff*sqrt(e_density*densconvert))+1.5*ln(T_i);
sum1 := ii_log*sqr(h_dens);
{now count impurity ions' contributions}
FOR i:=1 TO numimpurities DO
  WITH variables.impurities[i] DO
    FOR q:=1 TO Z DO
      BEGIN
        sum0 := sum0+(ei_log-ln(q))*q/mass;
        sum1 := sum1+(ii_log-0.5*ln(q))*sqr(values[q+1]*q) *
                sqrt(mass)
      END;
{finally..}
pwr[q_ei] := 7.47e-21*densconvert*sqr(e_density)*sum0*(T_e-T_i) /
        ( tempconvert*exp(1.5*ln(T_e)) )*k_pwr[q_ei];
{thermal conduction term - using classical for now}
pwr[q_thermal_e] := 8.81e9*sqr(e_density)*sqrt(T_e)*ei_log /
                    sqr(prm[templength]*J*j_scale*4*pi*maglength/c)
                    *k_pwr[q_thermal_e];
pwr[q_thermal_i] := 1.57e-15*sqrt(T_i)*sum1*densconvert /
           (tempconvert*sqr((J*j_scale*4*pi*maglength/c) *
           prm[templength]))
                    *k_pwr[q_thermal_i];
IF (t>t_c_on) AND (t<t_c_off) THEN
  BEGIN
    pwr[q_thermal_e] := pwr[q_thermal_e] *
                        sqr(compression(t_c_on,t_c_off,t,c_peak));
    pwr[q_thermal_i] := pwr[q_thermal_i] *
                        sqr(compression(t_c_on,t_c_off,t,c_peak))
  END;
pwr[q_rad] := getradiationpwr*k_pwr[q_rad];    {refer to function}
pwr[q_work_e] := T_e * (h_dens/prm[tau_p] +
                   impiondensity/prm[tau_imp])*k_pwr[q_work_e];
pwr[q_work_i] := T_i * h_dens/prm[tau_p]*k_pwr[q_work_i];
pwr[q_aux_e] := 0.0;                {no auxiliary heating for now}
pwr[q_aux_i] := 0.0;
{electron power balance}
dydt[1] := (pwr[q_ohmic]-pwr[q_rad]-pwr[q_ei]-pwr[q_thermal_e] -
     pwr[q_replace_e]-pwr[q_work_e]+pwr[q_aux_e])/(1.5*e_density);
{ion power balance}
```

```
      dydt[2] := (pwr[q_ei]-pwr[q_thermal_i]-pwr[q_replace_i]-pwr[q_cx]-
           pwr[q_work_i]+pwr[q_aux_i])/(1.5*(h_dens+impiondensity));
      {adjust temps for compression, if necessary}
      IF (t>t_c_on) AND (t<t_c_off) THEN
        BEGIN
          dydt[1] := dydt[1]+2*T_e *
                     d_compression(t_c_on,t_c_off,t,c_peak) /
                     compression(t_c_on,t_c_off,t,c_peak);
          dydt[2] := dydt[2]+2*T_i *
                     d_compression(t_c_on,t_c_off,t,c_peak) /
                     compression(t_c_on,t_c_off,t,c_peak)
        END
    END    {with variables do...}
END;   {routine derivs}

{ routine to time-step impurities (global) using implicit method. Solve
  tridiagonal system Au=w using method and notation of:
     D. Potter, "Computational Physics", (Wiley, New York, 1973),
     pp. 88-89.
  See also article by R. Hulse, Nucl. Fusion <3>,259 (1983). }
PROCEDURE advanceimpurities(VAR explicitvars:evolvetype; dt:real);
CONST theta = 0.75;  {explicit for theta=0, implicit for theta=1 }
                     {want theta>0.5 for stability!}
VAR  i,q : integer;
     thisionizcoef,nextrecombcoef,lastionizcoef,thisrecombcoef,
     lossrate,T_e,T_i,J,h_dens,h_n_dens    : real;
     w,alpha,beta,gamma                    : impurityarray;

{ tridiagonal, diagonal dominant matrix solver for linear system  Au=w.
  Caller provides matrix A in form of three vectors: alpha - upper
  diagonal, beta - diagonal, and gamma - lower diagonal. e.g. for A of
  form
    A = (a b 0 0) , have   alpha = (b e h S)   ,where S,T are unused.
        (c d e 0)          beta  = (a d g j)
        (0 f g h)          gamma = (T c f i)
        (0 0 i j)
  Also provides vector w, and size of system (if 'size'<dimension of A,
  uses first 'size' rows and cols of A). Resulting type is a global. }
FUNCTION tridiag(VAR alpha,beta,gamma,w:impurityarray;
                 size:integer) : impurityarray;
VAR i      : integer;
    temp   : real;
    x,y,u  : impurityarray;
BEGIN
  x[size-1] := -gamma[size]/beta[size];
  y[size-1] := w[size]/beta[size];
  FOR i:=size-1 DOWNTO 2 DO
    BEGIN
```

```
{      IF abs(beta[i])>(abs(alpha[i])+abs(gamma[i])) THEN
        writeln('SERIOUS ERROR in tridiag - not diagonal dominant!'); }
      temp := beta[i]+alpha[i]*x[i];
      x[i-1] := -gamma[i]/temp;
      y[i-1] := (w[i]-alpha[i]*y[i])/temp
    END;
  u[1] := (w[1]-alpha[1]*y[1])/(beta[1]+alpha[1]*x[1]);
  FOR i:=1 TO size-1 DO
    u[i+1] := x[i]*u[i]+y[i];
  tridiag := u
END;  {tridiag}

BEGIN
  T_e := explicitvars[1];  T_i := explicitvars[2];
  J := explicitvars[3];                 {just makes it easier to read}
  h_dens := explicitvars[4];  h_n_dens := explicitvars[5];
  lossrate := -1/prm[tau_imp];
  FOR i:=1 TO numimpurities DO
    WITH variables.impurities[i] DO
      BEGIN
        FOR q:=0 TO Z DO            {first construct alpha,beta,gamma}
          IF q<Z THEN
            BEGIN
              thisionizcoef  := densconvert*e_density*alpha_eii(Z,q,T_e);
              nextrecombcoef := (h_n_dens*alpha_cxr(Z,q+1,T_i) +
                                 e_density*alpha_rr(Z,q+1,T_e) +
                              e_density*alpha_dr(Z,q+1,T_e))*densconvert;
              IF q=0 THEN
                BEGIN
                  beta[1]  := 1-dt*theta*(lossrate-thisionizcoef);
                  alpha[1] := -dt*theta*nextrecombcoef;
                  w[1]     := dt*prm[imp_rate] + values[q+1] + dt*
                              (1-theta)*((lossrate-thisionizcoef) *
                              values[q+1] + nextrecombcoef*values[q+2])
                END
              ELSE
                BEGIN
                  gamma[q+1] := -dt*theta*lastionizcoef;
                  beta[q+1]  := 1-dt*theta *
                                (lossrate-thisionizcoef-thisrecombcoef);
                  alpha[q+1] := -dt*theta*nextrecombcoef;
                  w[q+1]     := values[q+1] + dt*(1-theta) *
                    (lastionizcoef*values[q]+nextrecombcoef*values[q+2]+
                    (lossrate-thisionizcoef-thisrecombcoef)*values[q+1])
                END;
              {for next stage of ionization}
              lastionizcoef  := thisionizcoef;
              thisrecombcoef := nextrecombcoef
```

```
            END   {if q<Z}
          ELSE {case q=Z}
            BEGIN
                  gamma[q+1] := -dt*theta*lastionizcoef;
                  beta[q+1]  := 1 - dt*theta*(lossrate-thisrecombcoef);
                  w[q+1]     := values[q+1] +
                                 dt*(1-theta)*(lastionizcoef*values[q] +
                                 (lossrate-thisrecombcoef)*values[q+1])
            END;   {for q:=0 to Z...}
        w := tridiag(alpha,beta,gamma,w,Z+1);          {now solve system}
        FOR q:=1 TO Z+1 DO
          values[q] := w[q]                  {and store values}
      END   {for i:=1 to numimpurities...}
END;  {advanceimpurities}
```

```
{ Set of routines called by program o_d_transport. These routines are
  algorithmic-specific. The global CONSTants, TYPEs, and VARiables
  are defined in file TRANSPRT.PAS }

{ procedure to do a single runge-kutta step. Taken from routine 'rk4',
  chapter 15 (see also appendix) of:

    NUMERICAL RECIPES - The Art of Scientific Computing,
    by  W.H. Press, B.P. Flannery, S.A. Teukolsky, and
    W.T. Vetterling,  Cambridge University Press, 1986.

  All routines taken from this source ("NR") are so noted. }
{ given n variables y and their derivs dydx at x, apply 4th order
  Runge-Kutta to advance the soltn over h, and return the answer as yout.
  User must supply the right-hand-side derivative routine 'derivs'. }
PROCEDURE r_k_4(VAR y,dydx,ymins : evolvetype; n : integer; x,h : real;
                VAR yout : evolvetype);
VAR i              :integer;
    temp,xh,hh,h6 : real;
    dym,dyt,yt    : evolvetype;

BEGIN
  hh := h*0.5;  h6 := h/6.0;  xh := x+hh;
  FOR i:=1 TO n DO                                  {first step}
    BEGIN
      yt[i] := y[i]+hh*dydx[i];
      IF yt[i]<ymins[i] THEN yt[i]:=ymins[i]      {do not allow y<ymins!}
    END;
  derivs(xh,yt,dyt);                          {second step}
  FOR i:=1 TO n DO
    BEGIN
      yt[i] := y[i]+hh*dyt[i];
      IF yt[i]<ymins[i] THEN yt[i]:=ymins[i]
    END;
  derivs(xh,yt,dym);                      {third step}
  FOR i:=1 TO n DO
    BEGIN
      yt[i] := y[i]+h*dym[i];
      IF yt[i]<ymins[i] THEN yt[i]:=ymins[i];
      dym[i] := dyt[i]+dym[i]
    END;
  derivs(x+h,yt,dyt);                 {fourth step}
  FOR i:=1 TO n DO              {accumulate increments with proper weights}
    BEGIN
      yout[i] := y[i]+h6*(dydx[i]+dyt[i]+2.0*dym[i]);
      IF yout[i]<ymins[i] THEN yout[i]:=ymins[i]
    END
END;   {r_k_4}
```

```
{ procedure to do an adjustable time step; taken from NR, routine 'rkqc'}
{ 5th order Runge-Kutta step with monitoring of local truncation error to
  ensure accuracy and adjust stepsize.
  Inputs:
    y,dydx,x             : dependent variable vector, deriv, at x.
    htry,eps             : trial stepsize, required accuracy.
    yscal                : scaling of error vector.
  Outputs:
    y,x                  : new y,x.
    hdid,hnext           : stepsize used, next estimated stepsize.
  Note that a right-hand-side derivative routine 'derivs' must also
  be defined. }
PROCEDURE rungekutta_qc(VAR y,dydx :evolvetype; n :integer; VAR x :real;
                        htry,eps : real; VAR yscal,ymins : evolvetype;
                        VAR hdid,hnext : real);
CONST pgrow  = -0.20;
      pshrnk = -0.25;
      fcor   = 0.06666666;       { 1/15 }
      one    = 1.0;
      safety = 0.9;              {recommended by NR}
      errcon = 6.0e-4;           { (4/safety)^(1/pgrow) }

VAR   i                        : integer;
      xsav,hh,h,temp,errmax    : real;
      dysav,ysav,ytemp         : evolvetype;
      success                  : boolean;

BEGIN
  success := false;
  xsav := x;                    {first, save initial values}
  FOR i:=1 TO n DO
    BEGIN
      ysav[i] := y[i];
      dysav[i] := dydx[i]
    END;
  h := htry;                    {set stepsize to initial trial value}
  WHILE (NOT success) AND (NOT quitearly) DO
    BEGIN
      hh := 0.5*h;                                  {take two half steps}
      r_k_4(ysav,dysav,ymins,n,xsav,hh,ytemp);
      x := xsav+hh;
      derivs(x,ytemp,dydx);
      r_k_4(ytemp,dydx,ymins,n,x,hh,y);
      x := xsav+h;
      IF x=xsav THEN
        BEGIN
          writeln(' Pause in rungekutta_qc... stepsize too small!');
```

```
          writeln(' Program will abort early...');
          quitearly := true
        END;
      r_k_4(ysav,dysav,ymins,n,xsav,h,ytemp);   {take the large step}
      errmax := 0.0;                            {now evaluate accuracy}
      FOR i:=1 TO n DO
        BEGIN
          ytemp[i] := y[i]-ytemp[i];    {ytemp now has error estimate}
          temp := abs(ytemp[i]/yscal[i]);
          IF errmax<temp THEN errmax:=temp
        END;
      errmax := errmax/eps;        {scale relative to required tolerance}
      IF errmax>one THEN         {trunc error too large, reduce stepsize}
        BEGIN
          h := safety*h*exp(pshrnk*ln(errmax));
          success := false           {will try again}
        END
      ELSE
        BEGIN                  {step succeeded, compute size of next step}
          success := true;
          hdid := h;
          IF errmax>errcon THEN hnext := safety*h*exp(pgrow*ln(errmax))
          ELSE hnext := 4.0*h
        END
    END;   {while not success...}
  IF success THEN
    FOR i:=1 TO n DO                {mop up 5th order trunc error}
      BEGIN
        y[i] := y[i]+ytemp[i]*fcor;
        IF y[i]<0.0 THEN y[i]:=0.0
      END
END;   {rungekutta_qc}

{ procedure to do integration of set of equations; adapted from routine
  'odeint' in NR. }
{ Runge-Kutta driver with adaptive stepsize control. Integrates the
  numvar starting values contained in data from t_start to t_end with
  accuracy epsilon, storing intermediate results in the globals
  time,result (the globals dt_save and maxsave refer to initial storage
  intervals and max # stored values, while the global changesavetime is
  the time after which the storage intervals are changed by the local
  variable newsavefactor). dt_start is a guessed first stepsize, dt_min
  is minimum allowed stepsize (can be 0.0). On output nok and nbad are
  the number of good and bad (but retried and fixed) steps taken, and
  data contains values at the end of the integration interval. Note that
  user must define a right-hand-side derivative routine derivs. The q_'s,
  chi, e_density are globals, calculated in derivs, that are displayed
  and/or saved for the user. }
```

```
PROCEDURE ode_integrate(VAR data : datatype; nvar : integer;
                        t_start : real; VAR t_end : real;
                        epsilon dt_start,dt_min : real;
                        VAR nok,nbad : integer);
CONST maxstp = 10000;
      zero   = 0.0;      two = 2.0;
      tiny   = 1.0e-25;
      newsavefactor = 3;       {factor for increasing storage intervals}
      gradualchange = 0.2;    {factor for gradually changing resistivity
           between its limits; smaller factor means more gradual change}
      fraction = 0.05;           {used to halt gradual changeover}

VAR   nstp,i,j,index,countchanges,fullcount,countsteps : integer;
      tsav,t,dt_next,dt_did,dt   : real;
      chi_prev                   : real;
      yscal,ymins,y,dydt,temp    : evolvetype;
      done,switched              : boolean;
      key                        : char;

  PROCEDURE save_results(t : real; numsaves : integer);
    CONST w = 8; p = 2; s = ' ';           {print formats}
    VAR i,j,index : integer;
    BEGIN
      time[numsaves] := t;
      writeln(' **** Data saved at time:',t:w:0,' microsec ****');
      writeln(' T_e,i (eV):',y[1]:w:p,'  ',y[2]:w:p);
      writeln(' J (A/cm^2): ',y[3]:w:p);
      writeln(' n,n_h (10^14 cm^-3):',y[4]:w:p,'  ',y[5]:w:p);
      FOR i:= 1 TO nonimpvars DO
        results[i,numsaves] := y[i];
      results[nonimpvars+ 1,numsaves] := e_density;
      results[nonimpvars+ 2,numsaves] := kappa;
      results[nonimpvars+ 3,numsaves] := chi_curr;
      index := nonimpvars+4;
      FOR i:=1 TO numimpurities DO
        WITH data.impurities[i] DO
          BEGIN
            FOR j:=0 TO Z DO
              results[index+j,numsaves] := values[j+1];
            index := index+Z+1
          END;
      results[index    ,numsaves] := pwr[q_ohmic];
      results[index+ 1,numsaves] := pwr[q_rad];
      results[index+ 2,numsaves] := pwr[q_thermal_e];
      results[index+ 3,numsaves] := pwr[q_replace_e];
      results[index+ 4,numsaves] := pwr[q_work_e];
      results[index+ 5,numsaves] := pwr[q_ei];
      results[index+ 6,numsaves] := pwr[q_thermal_i];
```

```
      results[index+ 7,numsaves] := pwr[q_replace_i];
      results[index+ 8,numsaves] := pwr[q_work_i];
      results[index+ 9,numsaves] := pwr[q_cx]
    END;

BEGIN
  t := t_start;  tsav := t_start;
  IF t_end>=t_start THEN dt := abs(dt_start) ELSE dt := -abs(dt_start);
  nok := 0;  nbad := 0;  numsaves := 0;
  done := false;  nstp := 0; switched := false;
  FOR i:=1 TO nvar DO
    CASE i OF     {set up array of minimum allowed values for variables}
      1,2 :       ymins[i] := prm[coldtemp];          {min temperatures}
      3   :       ymins[i] := prm[min_j];          {min current density}
      OTHERWISE   ymins[i] := tiny                     {min populations}
    END;
  WITH data DO
    BEGIN
      y[1] := e_temp;
      y[2] := i_temp;
      y[3] := currentdens;
      y[4] := h_density;
      y[5] := h_n_density
    END;
  kappa := prm[kappa_sp];   {just for starting, used by derivs routine}

{ NOTE: deactivated variable kappa sections - 2/7/90 }
{ for changing over kappa gradually, use k_(n)=(1-x)*k_(n-1) + x*klow,
  where
  k_(j) = kappa at jth iteration
  klow  = lower bound on kappa
  x     = factor for gradually changing k_(0) to klow; 0<x<=1 - smaller x
          means more gradual changeover.
  To avoid numerical problems, when kappa is within 'fraction' of
  kappalow, will terminate iterations and simply set kappa to kappalow -
  this is role of 'countchanges' and 'fullcount'. (1/24/90)}
{  countchanges := 0;
  fullcount := 1+trunc( ln(1+kappa/(fraction*prm[kappalow])) /
                        ln(1/(1-gradualchange)) ); }

  {****** Main loop ******}
  REPEAT
    nstp := nstp+1;
    derivs(t,y,dydt);

  {evaluate current chi and, depending on previous value, evaluate kappa}
    chi_curr := 1.33e-11*y[3]*j_scale/(y[4]*sqrt(y[2]));
 {   IF nstp=1 THEN chi_prev := chi_curr;
```

```
    IF (chi_prev>=prm[chiswitch]) AND (chi_curr>=prm[chiswitch]) THEN
      BEGIN
        kappa  = prm[kappa_sp];
        chi_prev := chi_curr
      END
    ELSE IF (chi_prev>=prm[chiswitch]) AND (chi_curr<prm[chiswitch]) THEN
      BEGIN
        kappa := (1-gradualchange)*kappa+gradualchange*prm[kappalow];
        chi_prev := 10*prm[chiswitch];     {anything >prm[chiswitch]}
{       countchanges := countchanges+1;
        IF countchanges>=fullcount THEN     {finished changeover}
{         BEGIN
            chi_prev := chi_curr;
            countchanges := 0
          END
      END
    ELSE IF (chi_prev<prm[chiswitch]) AND (chi_curr<prm[chiswitch]) THEN
      BEGIN
        kappa := prm[kappalow];
        chi_prev := chi_curr
      END
    ELSE      {do changeover to kappa_sp}
{     BEGIN
        kappa := (1-gradualchange)*kappa+gradualchange*prm[kappa_sp];
        chi_prev := 0.9*prm[chiswitch];     {anything <prm[chiswitch]}
{       countchanges := countchanges+1;
        IF countchanges>=fullcount THEN     {finished changeover}
{         BEGIN
            chi_prev := chi_curr;
            countchanges := 0
          END
      END;
}
    {do scaling used to monitor accuracy}
    FOR i:=1 TO nvar DO
      yscal[i] := abs(y[i])+abs(dydt[i]*dt)+tiny;
    {store intermediate results?}
    IF ((maxsave>0) AND (abs(t-tsav)>abs(dt_save)) AND
      (numsaves<(maxsave-1)))
      OR (numsaves=0) THEN
      BEGIN
        tsav := tsav+dt_save;       {tsav is modification of NR code.. }
        IF (tsav>changesavetime) AND NOT switched THEN
          BEGIN
            dt_save := newsavefactor*dt_save;
            switched := true
          END;
        numsaves := numsaves+1;     {to save data at regular intervals}
```

```
        {save wanted variables into globals}
        save_results(t/t_scale,numsaves)
      END;
    IF ((t+dt-t_end)*(t+dt-t_start))>zero THEN dt:=t_end-t;
                              {if step will overshoot, reduce stepsize}
    temp := y;                {store current values temporarily}
    rungekutta_qc(y,dydt,nvar,t,dt,epsilon,yscal,ymins,dt_did,dt_next);
    advanceimpurities(temp,dt_did);      {advance impurities implicitly}
    countsteps := countsteps+1;
    IF dt_did=dt THEN nok:=nok+1 ELSE nbad:=nbad+1;
    IF ((t-t_end)*(t_end-t_start))>=zero THEN            {are we done?}
      done := true
    ELSE
      BEGIN
        IF (abs(dt_next)<dt_min) THEN
          writeln(' Pause in ode_integrate, stepsize very small.');
        dt := dt_next
      END
  UNTIL (nstp>=maxstp) OR done OR quitearly;
  {**** End main loop ****}
  IF maxsave<>0 THEN
    BEGIN
      writeln(' time: ',t:fw);
      numsaves := numsaves+1;                      {save final step}
      {now save wanted variables into globals}
      save_results(t/t_scale,numsaves)
    END;
  IF (NOT done) AND (NOT quitearly) THEN
    writeln(' Pause in routine ode_integrate, too many steps!')
END;

{ procedure to write selected saved variables, as functions of time,
  to separate data files for later plotting. Note that globals used are:
    dataversion, variables, endtime. }
PROCEDURE dofilewrite;
CONST maxplots = 6;      {max # plots on one graph - depends on plotter}
      spc = ' '; wd = 9; wd2 = 7; plc = 2;    {for print formats}
VAR i,j,k,index,last,Zee,maxZee   : integer;
    dataname   : stringer;

BEGIN
  last := numsaves;                    {write temperature data}
  dataname := 'TEMPS';
  open(writefile,masterpath+dataname+dataversion+'.DAT',NEW);
  rewrite(writefile);
  FOR i:=1 TO last DO
    BEGIN
      write(writefile,time[i]:wd:plc,spc,results[1,i]:wd:plc,
```

```
          spc,results[2,i]:wd:plc);
    writeln(writefile)
  END;
close(writefile);

dataname := 'JDENS';               {write j data}
open(writefile,masterpath+dataname+dataversion+'.DAT',NEW);
rewrite(writefile);
FOR i:=1 TO last DO
  BEGIN
    write(writefile,time[i]:wd:plc,spc,results[3,i]:wd:plc);
    writeln(writefile)
  END;
close(writefile);

dataname := 'EXTRA';               {write kappa, chi data}
open(writefile,masterpath+dataname+dataversion+'.DAT',NEW);
rewrite(writefile);
FOR i:=1 TO last DO
  BEGIN
    write(writefile,time[i]:wd:plc,spc,results[7,i]:wd:plc,
          spc,results[8,i]:wd:plc);
    writeln(writefile)
  END;
close(writefile);

dataname := 'DNSTY';               {write density data}
open(writefile,masterpath+dataname+dataversion+'.DAT',NEW);
rewrite(writefile);
FOR i:=1 TO last DO
  BEGIN
    write(writefile,time[i]:wd:plc,spc,results[4,i]:wd,spc,
          results[5,i]:wd,spc,results[6,i]:wd);
    writeln(writefile)
  END;
close(writefile);

index := nonimpvars+4;             {write impurity population data}
FOR i:=1 TO numimpurities DO
  BEGIN
    dataname := 'IMP'+chr(ord('0')+i)+'_';
    Zee := variables.impurities[i].Z;
    IF Zee<maxplots THEN maxZee:=Zee
      ELSE maxZee:=maxplots-1;
    open(writefile,masterpath+dataname+dataversion+'.DAT',NEW);
    rewrite(writefile);
    FOR j:=1 TO last DO
      BEGIN
```

```
          write(writefile,time[j]:wd,spc);
          FOR k:=0 TO maxZee DO
            write(writefile,results[index+k,j]:wd,spc);
          writeln(writefile)
        END;
      index := index+Zee+1;
      close(writefile)
    END;

  dataname := 'EPWR_';                {write e pwr balance data}
  open(writefile,masterpath+dataname+dataversion+'.DAT',NEW);
  rewrite(writefile);
  FOR i:=1 TO last DO
    BEGIN
      write(writefile,time[i]:wd:plc);
      {write electron power data to file}
      FOR j:=index TO index+5 DO
        write(writefile,spc,results[j,i]:wd);
      writeln(writefile)
    END;
  close(writefile);

  dataname := 'IPWR_';                {write ion pwr balance data}
  open(writefile,masterpath+dataname+dataversion+'.DAT',NEW);
  rewrite(writefile);
  FOR i:=1 TO last DO
    BEGIN
      write(writefile,time[i]:wd:plc);
      {write ion power data to file}
      FOR j:=index+5 TO index+9 DO
        write(writefile,spc,results[j,i]:wd);
      writeln(writefile)
    END;
  close(writefile)
END;
```

```
{ Pascal 0-dim transport model, ported from Personal Pascal version for
  an Atari 1040ST. Version 1.10}

{ Include data setup routines and constants,types,and global vars }
{ I TRANSPORT.PAS }

{ Include data loading routines:      load_1_ratedata,load_2_ratedata }
{ I RATEDAT1.PAS }
{ I RATEDAT2.PAS }

{ Include method-specific routines:   derivs (alpha_cxr,alpha_rr,
                                     alpha_eii,alpha_dr,getradiationpwr) }
{ I MODEL.PAS }

{ Include time stepper and state solver routines:   r_k_4,rungekutta_qc,
                                         ode_integrator,dofilewrite }
{ I INTGRTR.PAS }


{ *** Main **** }
BEGIN
  writeln('          ************** 0 D Tranport Code  ************** ');
  writeln('          **                                            ** ');
  writeln('          **         VAX/VMS Pascal Version 1.50        ** ');
  writeln('          **              By Alex B. Filuk              ** ');
  writeln('          **              January 11, 1990              ** ');
  writeln('          **                                            ** ');
  writeln('          ************************************************ ');
  writeln;
  quitearly := false;
  getrunparameters(quitearly);  {load run parameters}
  load_1_ratedata;            {load tabular data for various rate coeffs}
  load_2_ratedata;
  IF NOT quitearly THEN
    BEGIN
      ode_integrate(variables,nonimpvars,begintime,endtime,
                    smallchange,firststep,minstep,numok,numbad);
      IF quitearly THEN writeln(' Aborting run...see result files')
      ELSE writeln(' All done...see result files');
      writeln(' Run duration (msec CPU): ',Clock:prc);
      writeln(' Number ok steps: ',numok:fw,' Number bad steps: ',
              numbad:fw);
      writeln(' Writing results to files; stand by....');
      dofilewrite;
      writeln(' That''s all folks...')
    END
  ELSE writeln(' Aborting early...')
END.   {enfin!}
```

Bibliography

[1] M. Yamada, *Fus. Tech.* **9** (1986) 38.

[2] G. Schmidt, *Physics of High Temperature Plasmas*, 2nd ed. (Academic, New York, 1979), Ch. 3.

[3] L. Woltjer, *Proc. Nat. Acad. Sci.* **44** (1958) 489.

[4] S. Chandrasekhar and L.Woltjer, *Proc. Nat. Acad. Sci.* **44** (1958) 489.

[5] G.C. Goldenbaum, J.H. Irby, Y.P. Chong, and G.W. Hart, *Phys. Rev. Lett.* 44 (1980) 393.

[6] T.R. Jarboe, I. Henins, H.W. Hoida, R.K. Linford, J. Marshall, D.A. Platts and A.R. Sherwood, *Phys. Rev. Lett.* **45** (1980) 1264.

[7] M. Yamada, H.P. Furth, W. Hsu, A. Janos, S.C. Jardin, M. Okabayashi, J. Sinnis, T.H. Stix and K. Yamazaki, *Phys. Rev. Lett.* **46** (1981) 188.

[8] J.B. Taylor, *Phys. Rev. Lett.* **33** (1974) 1139.

[9] M. Rosenbluth and M.N. Bussac, *Nucl. Fus.* **19** (1979) 489.

[10] R.M. Mayo, C.K. Choi, F.M. Levinton, A.C. Jones, and M. Yamada, *Phys. Fluids B* **2** (1990) 115.

[11] T.R. Jarboe, I. Henins, A.R. Sherwood, C.W. Barnes, and H.W. Hoida, *Phys. Rev. Lett.* **51** (1983) 39.

[12] T.R. Jarboe, C.W. Barnes, I. Henins, H.W. Hoida, S.O. Knox, R.K. Linford, and A.R. Sherwood, *Phys. Fluids* **27** (1984) 13.

[13] M. Yamada, in *Proc. 10th Int. Conf. Plasma Physics and Controlled Nuclear Fusion Research, 1984*, Vol. 2 (IAEA, Vienna, 1985) 535.

[14] C.W. Barnes, T.R. Jarboe, H.W. Hoida, B.L. Wright, R.A. Hulse, and D.E. Post, *Nucl. Fus.* **25** (1985) 1657.

[15] P.N. Guzdar, J.M. Finn, K.W. Whang, and A. Bondeson, *Phys. Fluids* **28** (1985) 3154.

[16] F.K. Hwang, A.W. DeSilva, G.C. Goldenbaum, C. Chin-Fatt, *Bull. Am. Phys. Soc* **35** (1990) 2056.

[17] J.-L. Gauvreau, G.C. Goldenbaum, C. Chin-Fatt, A.W. DeSilva, and R.A. Hess, *Bull. Am. Phys. Soc.* **35** (1990) 2056.

[18] J.C. Fernandez, T.R. Jarboe, S.O. Knox, I. Henins, and G.J. Marklin, *Nucl. Fus.* **30** (1990) 67.

[19] H.R. Griem, *Plasma Spectroscopy* (McGraw-Hill, New York, 1964).

[20] P.G. Carolan and V.A. Piotrowicz, *Plasma Phys.* **25** (1983) 1065.

[21] S. Jardin and U. Christensen, *Nucl. Fus.* **21** (1981) 1665.

[22] C. Chin-Fatt, A.W. DeSilva, G.C. Goldenbaum, R.A. Hess, C. Cote, A.B. Filuk, J.-L. Gauvreau, F.K. Hwang, and L. Kanaganayagasingam, *Bull. Am. Phys. Soc.* **34** (1989) 2052.

[23] J. Völkl and G. Alefeld, in *Hydrogen in Metals*, Vol. 1, eds. G. Alefeld and J. Völkl, Topics in Applied Physics Series, Vol. 28 (Spring-Verlag, New York, 1978).

[24] R.A. Alpher and D.R. White, in *Plasma Diagnostic Techniques*, eds. R.H. Huddlestone and S.L. Leonard, Ch. 10, (Academic, New York, 1965).

[25] H.J. Kunze, in*Plasma Diagnostics*, ed. W. Lochte-Holtgreven (North Holland, Amsterdam, 1968).

[26] C.J. Buchenauer and A.R. Jacobson, *Rev. Sci. Instr.* **48** (1977) 769.

[27] T.J. Dolan, *Fusion Research* Vol. I (Pergamon, New York, 1982).

[28] D.D. Meyerhofer, Ph.D. thesis, Princeton University, 1987.

[29] F.F. Chen, in *Plasma Diagnostic Techniques*, eds R.H. Huddlestone and S.L. Leonard, Ch. 4 (Academic, New York, 1965).

[30] D. Bohm, in *The Characteristics of Electrical Discharges in Magnetic Fields*, eds. A. Guthrie and R.K. Wakerling (McGraw-Hill, New York, 1949).

[31] I. Langmuir, in *Collected Works of Irving Langmuir*, ed. G. Suits, Vol. 4 (Macmillan, New York 1961).

[32] A.M. Cormack, *J. Appl. Phys.* **34** (1963) 2722, and **35** (1964) 2908.

[33] R.S. Anderssen, *J. Inst. Maths Applic.* **17** (1976) 329.

[34] Y. Nagayama, *J. Appl. Phys.* **62** (1987) 2702.

[35] G. Lewin, *Fundamentals of Vacuum Science and Technology*(McGraw-Hill, New York, 1965), p. 72.

[36] F.F. Chen, *Introduction to Plasma Physics* (Plenum, New York, 1974), p. 166.

[37] S. Ichimaru, *Basic Principles of Plasma Physics - A Statistical Approach* (Benjamin/Cummings, Massachusetts, 1973), Section 11.5.

[38] R.M. Mayo, F.M. Levinton, D.D. Meyerhofer, T.K. Chu, S.F. Paul, and M. Yamada, *Nucl. Fus.* **29** (1989) 1493; also R.M. Mayo, Ph.D. thesis, Purdue University, 1989.

[39] A.J. Wootton, B.A. Carreras, H. Matsumoto, K. McGuire, W.A. Peebles, Ch.P. Ritz, P.W. Terry, and S.J. Zweben, *Phys. Fluids B* **2** (1990) 2879.

[40] P.C. Liewer, *Nucl. Fus.* **25** (1985) 543.

[41] A. Hassam, private conversation.

[42] N.T. Gladd and N.A. Krall, *Phys. Fluids* **29** (1986) 1640.

[43] M. Wakatani and A. Hasegawa, *Phys. Fluids* **27** (1984) 611; A. Hasegawa and M. Wakatani, *Phys. Rev. Lett.* **50** (1983) 682.

[44] R. E. Waltz, *Phys. Fluids* **28** (1985) 577.

[45] P.W. Terry and P.H. Diamond, *Phys. Fluids* **28** (1985) 1419.

[46] L. Garcia, P.H. Diamond, B.A. Carreras, and J.D. Callen, *Phys. Fluids* **28** (1985) 2147.

[47] J.F. Drake and A.B. Hassam, *Phys. Fluids* **24** (1984) 1262.

[48] R.E. Olson and G.H. Miley, *Nucl. Technol./Fus.* **4** (1983) 1459.

[49] D.E. Shumaker, J.K. Boyd, S.P. Auerbach, and B. McNamara, *J. Comp. Phys* **45** (1982) 266

[50] F.M. Levinton and D.D. Meyerhofer, *Rev. Sci. Instr.* **58** (1987) 1393.

[51] W.C. Turner, G.C. Goldenbaum, E.H.A. Granneman, J.H. Hammer, C.W. Hartman, D.C. Prono, and J. Taska, *Phys. Fluids* **26** (1983) 1965.

[52] C.W. Barnes, T.R. Jarboe, I. Henins, A.R. Sherwood, S.O. Knox, R. Gribble, H.W. Hoida, P.L. Klingner, C.G. Lilliequist, R.K. Linford, D.A. Platts, R.L. Spencer, M. Tuszewski, *Nucl. Fus.* **24** (1984) 267.

[53] L. Johnson and E. Hinnov, *J. Quant. Spectrosc. Radiat. Transfer* **13** (1973) 333.

[54] D.D. Meyerhofer, R.A. Hulse, E.G. Zweibel, *Nucl. Fus.* **26** (1986) 235.

[55] D.L. Book, *NRL Plasma Formulary* (Naval Research Laboratory, Washington, D.C., 1987), NRL Publication 0084-4040.

[56] S.I. Braginskii, in *Reviews of Plasma Physics*, Vol 1 (Consultants Bureau, New York, 1965).

[57] G.R. Hopkins and J.M. Rawls, *Nucl. Tech.* **36** (1977) 171, and *Nucl. Tech* **43** (1979) 382.

[58] R. Elton, in *Methods of Experimental Physics*, Vol. 9, eds. H.R. Griem and R.H. Lovberg (Academic, New York, 1971), Ch. 4.

[59] D.E. Post, R.V. Jensen, C.B. Tarter, W.H. Grasberger, and W.A. Lokke, *At. Data Nucl. Data Tables* **20** (1977) 387.

[60] R. Mewe, *Astron. & Astrophys.* **20** (1972) 215.

[61] F.M. Levinton, D.D. Meyerhofer, R.M. Mayo, A.C. Janos, Y. Ono, Y. Ueda, M. Yamada, *Nucl. Fus.* **30** (1990) 871.

[62] L. Spitzer, Jr., *Physics of Fully Ionized Gases* (Interscience, New York, 1962).

[63] R.D. Milroy and J.U. Brackbill, *Phys. Fluids* **29** (1986) 1184.

[64] R. Chodura, *Nucl. Fus.* **15** (1975) 55.

[65] T.J. Dolan, *Fusion Research*, Vol II (Pergamon, New York, 1982).

[66] P.A. Sahlin, W. Pierce, H. Biglari, H.H. Fleischmann, S.C. Jardin, *Phys. Fluids B* **2** (1990) 554.

[67] J.C. Fernandez, C.W. Barnes, T.R.Jarboe, I. Henins, H.W. Hoida, P.L. Klingner, S.O. Knoz, G.J. Marklin, and B.L. Wright, *Nucl. Fus.* **28** (1988) 1555.

[68] F.J. Wysocki, J.C. Fernandez, I. Henins, T.R. Jarboe, and G.J. Marklin, *Phys. Rev. Lett.* **65** (1990) 40.

[69] T. Uyama, *Nucl. Fus.* **27** (1987) 799.

[70] S.P. Auerbach, *Phys. Fluids* **25** (1982) 1108.

[71] T.J. Dolan, *Fusion Research*, Vol III (Pergamon, New York, 1982).

[72] R.D. Cowan, *The Theory of Atomic Structure and Spectra* (University of California Press, Los Angeles, 1981) p. 546.

[73] S.M.V. Aldrovandi and D. Pequignot, *Astron. & Astrophy.* **25** (1973) 137.

[74] R.A. Phaneuf, R.K. Janev, and M.S. Pindzola, *Collisions of Carbon and Oxygen Ions with Electrons, H, H2, and He*, Atomic Data for Fusion Series, Vol. V (Oak Ridge National Laboratory, 1987), publication ORNL 6090.

[75] R.A. Hulse, private conversation.

[76] R.A. Hulse, D.E. Post, and D.R. Mikkelson, *J. Phys. B* **13** (1980) 3895.

[77] G.W. Hart, C. Chin-Fatt, A.W. DeSilva, G.C. Goldenbaum, R. Hess, and R.S. Shaw, *Phys. Rev. Lett.* **51** (1983) 1558.

[78] G.W. Hart, A. Janos, D.D. Meyerhofer, and M. Yamada, *Phys. Fluids* **29** (1986) 1994.

[79] W.H. Press, B.P. Flannery, S.A. Teukolsky, and W.T. Vetterling, *Numerical Recipes – The Art of Scientific Computing* (Cambridge, New York, 1986).

[80] R.A. Hulse, *Nucl Technol./Fus.* **3** (1983) 259.

[81] D. Potter, *Computational Physics* (Wiley & Sons, New York, 1973).

[82] R.E. Olson, Ph.D. thesis, University of Illinois at Urbana-Champaign, 1983.

[83] S.O. Knox, C.W. Barnes, G. Marklin, T.R. Jarboe, I. Henins, H.W. Hoida, and B.L. Wright, *Phys. Rev. Lett.* **56** (1986) 842.